Summer 2017

Liquid pulsed plasma thruster plasma plume investigation and MR-SAT cold gas propulsion system performance analysis

Jeremiah Daniel Hanna

Department:

LIQUID PULSED PLASMA THRUSTER PLASMA PLUME INVESTIGATION AND MR-SAT COLD GAS PROPULSION SYSTEM PERFORMANCE ANALYSIS

by

JEREMIAH DANIEL HANNA

A THESIS

Presented to the Faculty of the Graduate School of the

MISSOURI UNIVERSITY OF SCIENCE AND TECHNOLOGY

In Partial Fulfillment of the Requirements for the Degree

MASTER OF SCIENCE

IN

AEROSPACE ENGINEERING

2017

Approved by

Dr Joshua Rovey, Advisor
Dr Henry Pernicka, Co-Advisor
Dr David Riggins

ABSTRACT

The plasma plume produced by a liquid pulsed plasma thruster is investigated using a Langmuir triple probe and a nude Faraday probe. The Langmuir triple probe failed to produce results which are suspected caused by the presence of ionic liquid in the plume resulting in shorting of the probe. The nude Faraday probe is able to record the ion current density which revealed a high level of inconsistency in the plasma plume. Ion current density recorded by the nude Faraday probe had a relative standard deviation of upwards of 100% of the mean value. Controlling the amount of propellant used during each pulse was extremely difficult. Investigating the plasma plume with more complex probes was not done due to the inconsistency measured by the nude Faraday probe and the expulsion of ionic liquid from the thruster which is highly corrosive to metals.

Examining the historical thrust test data performed by the Missouri Satellite Research Team, a revised model with new assumptions was created and resulted in an improvement in accuracy to within 4.5%. The cold gas propulsion system developed over the years had undergone testing which resulted in measured thrust half of what was predicted. Developing a thrust prediction scheme that incorporates the effects of the solenoid control valve decreases the error to between 1-3% depending on temperature considerations. This thrust prediction scheme can be applied to the current design for the NanoSat 8 competition and results in an accurate prediction of thrust.

ACKNOWLEDGMENTS

I would like to deeply thank Dr Joshua Rovey for advising during my time as a graduate student at the Missouri University of Science and Technology. He pushed me to explore concepts and ideas that I would not have on my own. I would also like to thank my co-advisor, Dr Henry Pernicka, for allowing me to explore and access the design and concepts of the Missouri Satellite Research Team. I would also like to mention all the members of the Aerospace Plasma Laboratory who have been enormously helpful and friendly. I would especially like to thank Matthew Glascock for assisting me with setting up the plasma plume analysis experiments and teaching me how to run the large vacuum chamber.

I have been extremely fortunate to have the encouragement, love, and understanding of my wife Jennifer Neighbors. She has been incredibly helpful in keeping me on track to finish my academics endeavors. I also must thank my parents, Michael and Lori Hanna, and my siblings Sarah Hanna, Douglas Hanna, and Joshua Hanna for their support.

TABLE OF CONTENTS

LIST OF ILLUSTRATIONS

LIST OF TABLES

NOMENCLATURE

Abbreviation	
AP Lab	Aerospace Plasma Laboratory
DSSP	Digital Solid State Propulsion
FEEP	field emission electric propulsion
GEM-10T	Green Electric Monopropellant
GFSSP	Generalized Fluid System Simulation Program
HAN	hydroxylammonium nitrate
HiPEP	High Performance Electric Monopropellant
LOX	liquid oxygen
LPPT	liquid pulsed plasma thruster
LTP	Langmuir triple probe
MEDiC	Multiple Energy Discharge Controller
MMH	monomethylhydrazine
M-SAT	Missouri Satellite Research Team
MS&T	Missouri University of Science and Technology
MPCF	multiple point choked flow
MPD	magneto-plasma-dynamic
MZI	Mach-Zehnder interferometry
NASA	National Aeronautical and Space Administration
NFP	nude Faraday probe
NVT	nozzle on a valve thruster
OMS	orbital maneuvering system
PPT	pulsed plasma thruster
SCFM	standard cubic feet per minute
SCMS	standard cubic meters per second
SPT	straight pipe thruster
VLAD	Valved Liquid Actuation Device

Liquid Pulsed Plasma Thruster Plume Analysis

A_n	area of probe n = 1, 2, 3, C
(t)	measure probe current with respect to time,
$J_i(t)$	ion current density with respect to time
$J_{i,}$	maximum ion current density
m_{expel}	mass of propellant expelled
m_i	initial mass of propellant
m_{gas}	mass of gaseous propellant expelled
m_{final}	final mass of propellant
m_{leak}	mass of leaked propellant
m_{liquid}	mass of liquid propellant expelled
m_{plasma}	mass of plasma expelled
m_{used}	mass of propellant used during experiment
n_e	electron density
T_e	electron temperature
U_i	ion velocity
V_{dn}	voltage difference between probes 1 and n = 2, 3

Cold Gas Thruster Performance Analysis

A	area
AR	area ratio between the throat and exit
a	speed of sound
C_d	coefficient of discharge
C_p	specific heat at constant pressure
C_v	flow coefficient
c^*	characteristic velocity
d	diameter
F	thrust
f_t	temperature correction factor
G_g	specific gravity

g	gravitational constant
I	moment of inertia
I_{bit}	impulse bit
I_{sp}	specific impulse
K	gas valve flow constant
k_s	spring constant
L	Lohm rating
L_{cm}	length to the center of mass
L_t	length to the thruster
M	Mach number
m	mass
$\dot{m}$	mass flow rate
N	numerical constant
ΔP	pressure differential
P	pressure
PR	pressure ratio
Q	volumetric flow rate
R	gas constant
T	temperature
u	velocity
x_{ss}	steady state displacement
α	nozzle half angle
γ	ratio of specific heat
ζ_F	force correction factor
ζ_v	specific impulse correction factor
ζ_d	mass flow rate correction factor
λ	momentum correction factor
θ	angular position
ω_n	natural frequency

1. INTRODUCTION

On October 4, 1957 history was made when the Soviet Union launched Sputnik I and became the first nation to successfully put a satellite into orbit around Earth [1]. This metallic sphere, roughly the size of a beach ball, caught the world off guard at started the space race between the United States of America and Soviet Union. Then in November 3, 1957 the Soviet Union successfully launched Sputnik II which was a satellite large enough to carry a dog into orbit.

It was not until January 31, 1958 that the United States would successfully launch Explorer I into orbit around Earth [2]. Explorer I, shown in Figure 1.1., was the United States response to Sputnik I and was the first satellite to carry scientific instruments. The data provided by the cosmic ray detector onboard Explorer1 would be used to discover the radiation belts around Earth. Explorer 1 re-entered Earth's atmosphere on March 31, 1970.

On November 10, 1958 Pioneer 1, shown in Figure 1.2., became the first spacecraft successfully launched by the newly formed National Aeronautics and Space Administration (NASA) [3]. Pioneer 1 mission was to investigate ionizing radiation,

Figure 1.1. Explorer 1, the first satellite successfully launched by the United States [2].

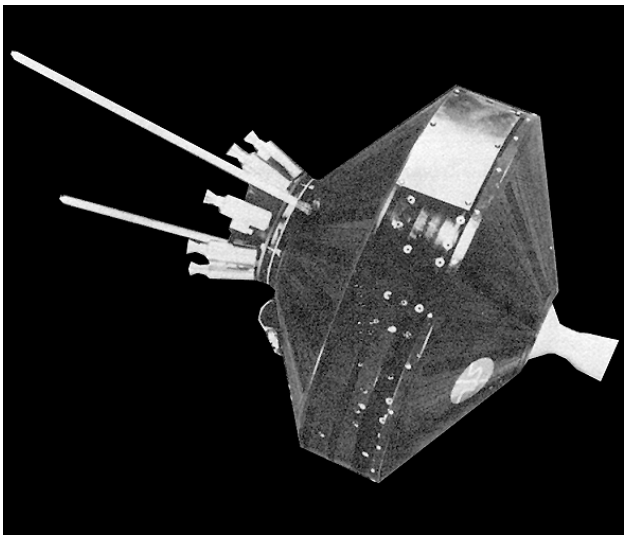

Figure 1.2. Pioneer 1, the first spacecraft launched by NASA [3].

cosmic rays, magnetic fields, and micrometeorites around Earth and the Moon. This spacecraft was the first to have an onboard propulsion system for orbital maneuvering. Pioneer 1 carried an 11 kg solid propellant rocket motor for injection into a lunar transfer orbit and eight smaller low thrust solid propellant rocket motor to perform a velocity correction to achieve orbit around the Moon. The mission never achieved orbit around the Moon due to a launch vehicle malfunction that left Pioneer 1 on a sub-orbital trajectory.

1.1. TYPES OF SPACECRAFT PROPULSION SYSTEMS

Spacecraft use several different types of propulsion systems during their lifespan. To get into orbit a launch vehicle uses a primary propulsion system typically consisting of liquid propellant rocket engines and solid rocket motor boosters. Once in orbit a spacecraft employs a secondary propulsion system to achieve its final orbit, maintain that orbit, and control its attitude. To achieve a large change in velocity modern spacecraft typically use an electric propulsion system.

There are multiple choices for propulsion system available to mission planners. Each of these propulsion systems has its own advantages and disadvantages. For a mission requiring a large change in velocity a spacecraft should use a propulsion system

with a high specific impulse to minimize the propellant necessary. To get a spacecraft into orbit a propulsion with a high thrust-to-weight ratio is necessary to get the launch vehicle off the ground. Several propulsion systems and their typical specific impulse and thrust to weight ratio are shown in Table 1.1. [4].

Table 1.1. Performance parameters of different propulsion systems [4].

Engine Type	Specific Impulse [sec]	Thrust-to-Weight Ratio
Bi-propellant (solid or liquid)	200 – 468	0.1 – 100
Mono-propellant	194 – 223	0.1 – 1.0
Resistojet	150 – 300	10^{-4} – 0.1
Arcjet	280 – 1,200	10^{-4} – 0.1
Pulsed Plasma	700 – 2,500	10^{-6} – 10^{-4}
Hall Effect Thruster	1,000 – 1,700	10^{-4}
Ion Engine	1,200 – 5,000	10^{-6} – 10^{-4}

1.1.1. Primary Propulsion Systems. Primary propulsion systems are used to insert a spacecraft into its initial orbit. They are generally characterized by a high thrust-to-weight ratio. The need to accelerate the launch vehicle to the high velocity required to achieve an initial orbit limits choices of primary propulsion systems to liquid, solid, and hybrid propellant systems. Liquid propellant rocket engines are typically the primary propulsion system of the majority of launch vehicles. Solid propellant rocket motors are typically used as boosters to assist during the first stage of a launch. There is growing interest in developing hybrid systems for use in launch vehicles.

1.1.1.1 Liquid propellant rocket engines. Liquid propellant rocket engines comprise the primary propulsion system of the majority of launch vehicles. These systems operate through the combustion of a liquid fuel and oxidizer to produce a high temperature and pressure gas which is then thermodynamically expanded through a nozzle producing thrust. Liquid propellant rocket engines have several advantages that make them ideal for launch vehicles. The disadvantages of these systems typically come from the complexity of their design. The F1 developed by Rocketdyne for the Saturn V are the most powerful liquid propellant rocket engine to ever successfully be used in a launch vehicle.

Liquid propellant rocket engines have the highest level of complexity in their design and operation of any primary propulsion system [4]. The primary components of these primary propulsion systems consist of propellant storage tanks, propellant feed systems, and a thrust chamber. A schematic of a liquid propellant rocket engine is shown in Figure 1.3. The propellant storage tanks that contain the fuel and oxidizer can be very large and may require design considerations for pressurization and the storage of cryogenic propellants. The propellant feed system encompasses all the propellant lines and typically one or more turbo pumps that supply the fuel and oxidizer to a thrust chamber. The thrust chamber of a liquid propellant rocket engine consists of fuel and oxidizer injectors, the combustion chamber and a nozzle. In large thrust chambers that operate for extended periods of time a complex cooling system that takes advantage of the cryogenic fuels are used to cool the structure.

The advantages of liquid propellant rocket engines come from their relative high performance when compared to other primary propulsion systems along with a large degree of control over their operation [4]. Depending on propellant selection, liquid propellant rocket engines have the highest specific impulse of any primary propulsion system. These systems have a high thrust-to-weight ratio making them ideal for lifting heavy launch vehicles off the launch pad. Liquid propellant rocket engines have the ability to start, stop, and then restart along with being able to be throttled which allows for complex launch trajectories to be achieved. Some of these systems are gimbaled allowing for thrust vectoring adding another degree of control over the launch vehicle.

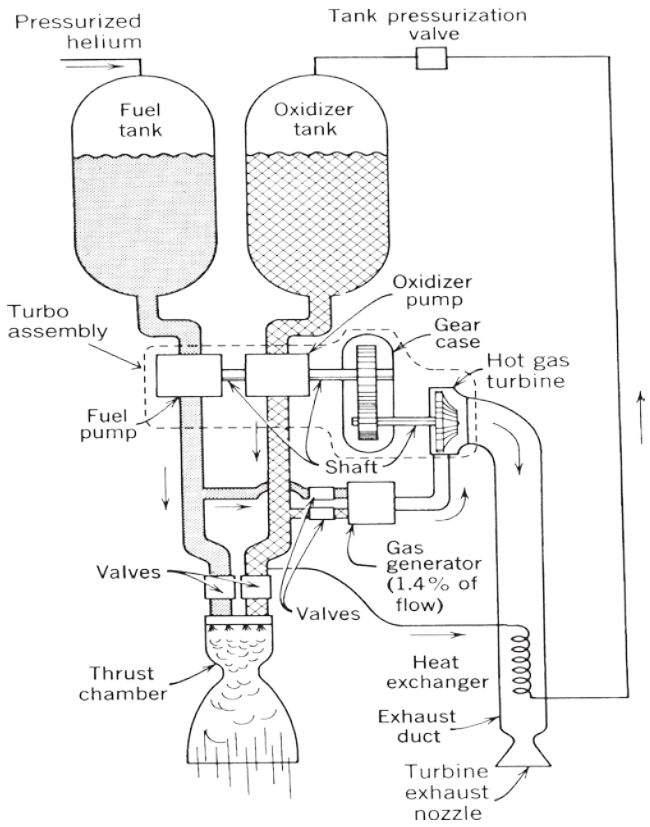

Figure 1.3. Schematic of a liquid propellant rocket engine that utilizes a turbopump feed system [4].

The disadvantages of liquid propellant rocket engines come from the complexity of their design and operation [4]. The challenges begin with the propellant tanks that may have to store cryogenic propellants which require insulation, temperature constraints on structural material, and long term storage issues. The propellant feed system requires components that operate at high pressure and the mass flow rates of propellants require powerful turbo pumps. The high temperature and pressure of the thrust chamber requires complex structural architecture and thermal management systems. The overall complexity of the of liquid propellant rocket engine designs leads to a large number of failure modes that must be mitigated. The complex engineering requirements of these systems makes them expensive to develop.

Liquid propellant rocket engines have several different propellant combinations available depending on performance requirements of the system [4]. The most common oxidizer historically used by the National Air and Space Administration (NASA) launch vehicles is liquid oxygen (LOX) which is a cryogenic liquid that provides excellent combustion performance. Other oxidizer choices include hydrogen peroxide, nitric acid, and nitrogen tetroxide. A typical fuel of NASA launch vehicles is liquid hydrogen which is a cryogenic liquid that when combined with LOX provides the highest performance of any fuel/oxidizer combination. Other liquid propellant rocket engine propellants include hydrocarbon fuels like kerosene, gasoline, and turbojet fuel, hydrazine, unsymmetrical dimethyl-hydrazine, and monomethyl-hydrazine.

The Saturn V is, to date, the most powerful launch vehicle ever successfully flown and was used during the NASA Apollo mission to land a man on the moon [5]. The first stage of the Saturn V consisted of five F1 liquid propellant rocket engines developed by Rocketdyne. The F1 used a LOX and kerosene fuel/oxidizer combination to produce 7,740 kN each at a specific impulse of 304 sec. Despite its troubled development no F1 ever failed during a launch.

1.1.1.2 Solid propellant rocket motors. Solid propellant rocket motors are typically used as boosters attached to the first stage of a launch vehicle. The design and operation of these primary propulsion systems is more simplistic than liquid propellant rocket engines typically with few, if any, moving parts. The advantages of these systems come from the simplicity of their design and operation. Typically the disadvantages of solid rocket motors are due to the lack of control mechanisms during their operation. There are several different propellant combinations for these systems which are premixed together in what is referred to as the grain. A well-known solid propellant rocket motor is the SRB made by Thiokol that assisted the Space Shuttles during their ascent into orbit.

Solid propellant rocket motors have a relatively simple design and operation when compared to other primary propulsion systems [4]. The fuel and oxidizer are pre-mixed during the manufacturing process of the grain where the performance of the solid propellant rocket motor is determined by grain composition and internal geometry. The casing in which the grains are inserted acts as the combustion chamber and typically is the primary structure of a solid rocket motor. An ignition system is employed to start the

combustion process on the internal surface of the grain. The high pressure and temperature gas is then expelled through a nozzle producing thrust. Some solid propellant rocket motor's nozzles are gimbaled allowing for thrust vectoring. A perspective of a solid propellant rocket motor is shown in Figure 1.4.

The advantages of solid propellant rocket motors come from the simplicity of their design and operation [4]. Typically there are no moving parts in these systems reducing the number of failure modes. Solid propellant rocket motors have a high thrust-to-weight ratio making them well suited for their typical role as a booster of launch vehicles during their first stage. The grain geometry and composition can be tailored to produce varying levels of performance over the duration of the burn of a solid propellant rocket engine. Due to the simplicity of these primary propulsion systems they are cheaper to design and manufacture.

The disadvantages of solid propellant rocket motors come from the lack of control over their operation during a launch [4]. Once a solid propellant rocket motor is ignited there is no control mechanism to stop the combustion process of the grain. These primary

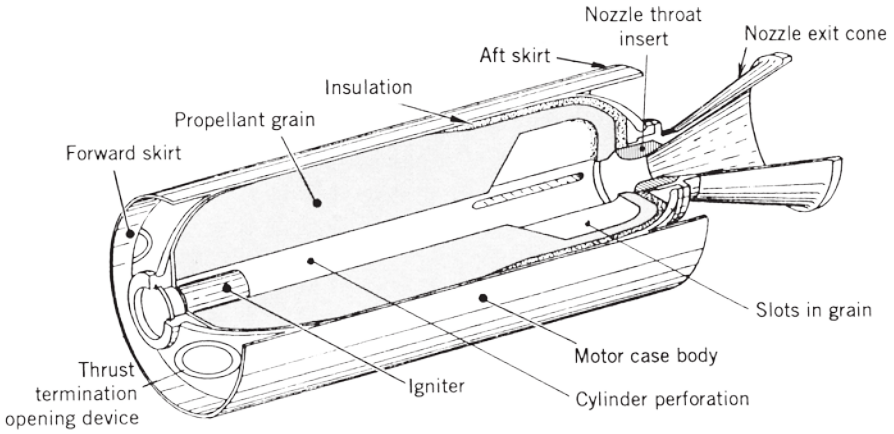

Figure 1.4. Perspective of a solid propellant rocket motor that highlights their relative simplistic design [4].

propulsion systems lack an ability to vary their performance on command. Cracks that form in the grain will vary the performance of the solid propellant rocket motor.

Several different fuel/oxidizer combinations are available for the grain of solid propellant rocket motors [4]. Most grains consist of oxidizers, fuels, binders, plasticizers, and curing agents. A typical oxidizer is ammonium perchlorate because of its compatibility, performance, and availability. A common fuel is spherical powdered aluminum but there is interest in boron and beryllium based fuels due to their increased performance. The binders, plasticizer, and curing agents are used to combine the fuel and oxidizer in a solid state.

A well-known solid propellant rocket motor is the SRB made by Thiokol that was used as the boosters on Space Shuttle launches [6]. The SRB was a massive solid propellant rocket motor measuring 126.21 ft high with a diameter of 12.71 ft. The SRB produced 11,519 kN of thrust at a specific impulse 237 sec with a total burn time of 124 sec. The SRB was brought to attention of the general public when a failure in an O-ring led to the destruction of Space Shuttle Challenger.

1.1.1.3 Hybrid propellant rocket engine. A hybrid propellant rocket engine consists of storing either the fuel and oxidizer as a solid and the other as a liquid. There is interest in hybrid propellant rocket engines due to several advantages they have over other primary propulsion systems. Despite the advantages of hybrid propellant rocket engines there are several disadvantages that must be overcome before these systems become more widespread in launch vehicles. There are multiple different propellant options available for hybrid propellant rocket engines to utilize. A well-known hybrid propellant rocket engine was successfully used as SpaceShip One primary propulsion system.

There are three types of hybrid propellant rocket engines [4]. What are defined as the typical or classical configurations use a liquid oxidizer and a solid fuel. The reverse or inverse configuration has a solid oxidizer and a liquid fuel. The mixed hybrid configuration involves uses a premixed fuel/oxidizer grain that is supplemented by a liquid oxidizer. These different configurations allow for different mission profiles to be achieved. A schematic of a simply classical configuration hybrid propellant rocket engine is shown in Figure 1.5.

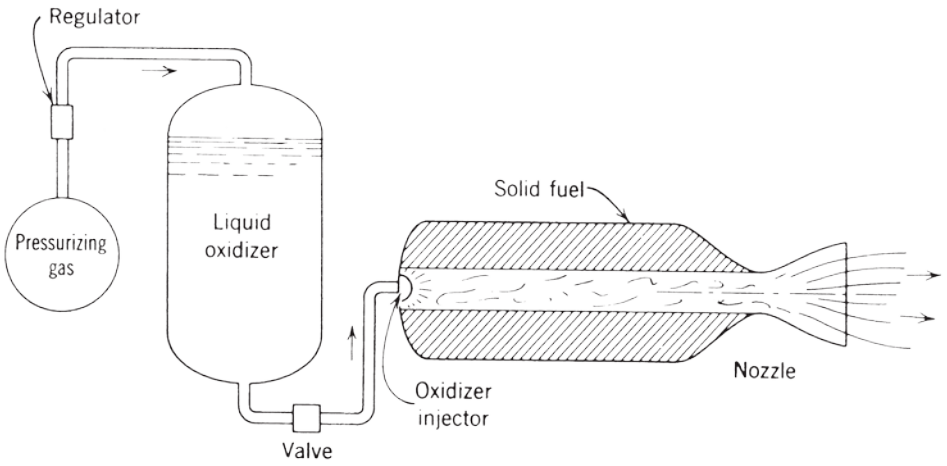

Figure 1.5. A schematic of a simplified hybrid propellant rocket motor [4].

Hybrid propellant rocket engines have a number of advantages compared to other primary propulsion systems [4]. Hybrid propellant rocket engines are safer than solid propellant rocket motors during manufacture and transportation since the fuel and oxidizer is typically not premixed. These primary propulsion systems have the ability to start, stop, and then restart on command allowing for multiple burns during a given launch profile. There are large reduction in complexity in design and operation of hybrid propellant rocket engines relative to liquid propellant rocket engines. These primary propulsion systems typically have a higher specific impulse than solid propellant rocket motors. Hybrid propellant rocket engines have throttling capabilities similar to liquid propellant rocket engines.

There are a number of disadvantages for hybrid propellant rocket engines compared to other primary propulsion systems [4]. The fuel/oxidizer mixture ratio typically varies over the extent of a burn and during throttling resulting in varying specific impulse and thrust. Hybrid propellant rocket engine fuel grains require complex internal geometry that typically has unavoidable fuel residual remaining at the end of the burn. The complex internal geometry makes accurately predicting the regression rate of the fuel grain difficult.

There are several different fuel and oxidizer combination available for hybrid propellant rocket engines [4]. A common fuel/oxidizer combination for large hybrid propellant rocket engines is LOX and oxygen-hydroxyl-terminated polybutadiene (HTPB). Other common high energy fuels are typically light metal hybrids with a polymeric binder. Other oxidizers that have been proposed for hybrid propellant rocket engines are hydroxyl ammonium nitrate (HAN), nitrous oxide, and hydrogen peroxide.

A hybrid propellant rocket engine successfully propelled SpaceShip One on a sub-orbital flight [7]. SpaceShip One was developed by Scaled Composites and won the Ansari X prize in 2004 after being the first private company to successfully perform two sub-orbital flights. The primary propulsion system for SpaceShip One is a nitrous oxide/HTPB hyprid propellant rocket engine developed by SpaceDev [8]. The hybrid propellant rocket engine on SpaceShip One produced 73.5 kN of thrust at a specific impulse of 250 sec for 90 sec propelling the spacecraft of 112 km above the Earth.

1.1.2. Secondary Propulsion Systems. Once a spacecraft has achieved an initial orbit with its launch vehicle a secondary propulsion system is used to achieve the final orbit, maintain that final orbit, and control its attitude. The secondary propulsion system is typically not as prominent a feature on a spacecraft as the primary propulsion system on a launch vehicle but is just as important. The currently available types of secondary propulsion systems include cold gas thrusters, mono and bi propellant rocket engines, solid propellant rocket motors, and electric propulsion systems.

1.1.2.1 Cold gas propulsion systems. Cold gas propulsion systems are typically comprised of a pressurized inert gas. The kinetic energy of the exhaust gas comes solely from the stored energy of the pressurized reservoir. The advantages of these secondary propulsion systems is due to the designs of the system are typically simpler than other thermodynamic propulsion systems. The disadvantages come from the low performance and large volumes of cold gas propulsion systems. An experimental cold gas propulsion system will be used as the attitude control system on the upcoming INSPIRE CubeSat.

Cold gas propulsion systems produce thrust by expelling pressurized gas through a nozzle [9]. The kinetic energy associated with the exhaust gases comes from the potential energy stored in the pressurized reservoir. In true cold gas propulsion system there is no heat transfer or combustion resulting in a low temperature exhaust gas. Cold

gas propulsion systems typically produce a small amount of thrust at a low specific impulse.

The design of cold gas thruster system is similar to other secondary propulsion systems that produce thrust thermodynamically [9]. Typically a propellant tank will feed a plenum chamber that is designed to maintain a certain pressure either by a regulator or carefully controlling the propellant flow with control valves. From the plenum chamber a series of propellant feed lines will supply cold gas thrusters positioned around the spacecraft. The cold gas thrusters themselves simply consist of a nozzle position closely to a control valve.

The advantages of cold gas thruster systems come from the simplicity of their design and operation [9]. These systems typically do not have large power requirements which makes them ideal for satellites with limited power generation capabilities or large power requirements of other subsystems. The lack of chemical combustion or heat transfer results in a secondary propulsion system that has limited thermal effects on the interior of a satellite. The lack of heat generation makes cold gas propulsion systems ideal for small satellites that typically do not have active thermal management systems. Cold gas propulsion systems are very reliable and are proven for spaceflights of over a decade [4]. These secondary propulsion systems are also safe, the propellants are typically non-toxic, the designs are simply, and they are inexpensive to produce.

The disadvantages of cold gas propulsion systems come from their lack of performance [4]. These secondary propulsion systems typically have very poor propellant mass fraction and thrust-to-weight ratio. The low specific impulse results in a small change in velocity of the spacecraft when compared to other secondary propulsion systems with the same propellant mass. The low specific impulse also requires that a cold gas propulsion system will need a large propellant tank which can cause problems on small spacecraft where internal volume is limited.

The propellants for typical cold gas propulsion systems are inert gases [4]. Nitrogen, argon, dry air, krypton, and Freon 14 have been successfully operated on spacecraft. The performance of several cold gas propulsion system propellants is shown in Table 1.2 [4]. The propellants that theoretically would provide the highest performance are typically not used because their low density would require large high pressure

propellant tanks to achieve a sizeable change in velocity for the spacecraft. Refrigerant-based propellant alleviates some of the storage issues by storing the propellant as a saturated liquid in the propellant tank.

Table 1.2. Typical cold gas propellant properties.

Propellant	Molecular Mass	Density[a] [lb/ft^3]	Specific Heat Ratio *k*	Theoretical Specific Impulse[b] [sec]
Hydrogen	2.0	1.77	1.40	284
Helium	4.0	3.54	1.67	179
Methane	16.0	14.1	1.30	114
Nitrogen	28.0	24.7	1.40	76
Air	28.9	25.5	1.40	74
Argon	39.9	35.3	1.67	57
Krypton	83.8	74.1	1.63	50

[a] At 5000 psia and 20˚C.

[b] In vacuum with nozzle area ratio of 50:1 and initial temperature of 20˚C.

The University of Texas at Austin (UT-Austin) has developed a cold gas propulsion system for controlling the attitude of a CubeSat [10]. The team UT-Austin used additive manufacturing to combine the propellant tank, plenum, propellant feed lines, and nozzles into one component. The entire propellant system fits a volume of less than 1U (10 cm X 10 cm X 10 cm) and will be the primary attitude control system of the INSPIRE spacecraft. The cold gas propulsion system uses the refrigerant propellant R236-fa. The four nozzles produce approximately 60 mN of thrust at a specific impulse of 65 sec.

1.1.2.2 Monopropellant propulsion systems. Monopropellant propulsion systems allow for moderate levels of performance from a secondary propulsion system

while still having a simply design. Monopropellant propulsion systems have difficulties maintaining the catalyst bed over the lifespan of a spacecraft. The main monopropellant used in these secondary propulsion systems is hydrazine. Monopropellant propulsion systems are found on many spacecraft as attitude control systems.

Monopropellant propulsion systems have a simpler design than a bipropellant propulsion system [4]. In monopropellant propulsion systems a stable yet easily decomposed liquid propellant is used to produce thrust. The monopropellant is supplied from a pressurized propellant tank as a liquid to a catalyst where an exothermic decomposition of the propellant takes place. The high temperature and pressure exhaust gas is then expanded thermodynamically through a nozzle producing thrust. The catalyst bed design is important in assuring a complete decomposition of the monopropellant as well preventing the loss of catalytic material. A schematic of a typical hydrazine monopropellant thruster is shown in Figure 1.6.

The advantage of a monopropellant propulsion system is that it produces moderate levels of performance while retaining a simple design [4]. Monopropellant

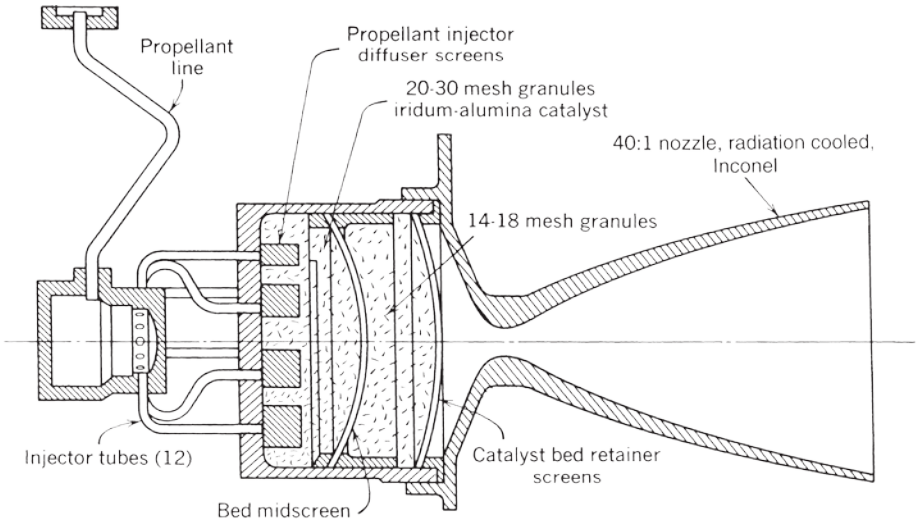

Figure 1.6. Schematic of a typical hydrazine monopropellant thruster [4].

propulsion systems typically have a higher specific impulse than cold gas propulsion systems allowing for an increase in the change of velocity of the spacecraft for the same mass of propellant. The exhaust plume produced by a typical monopropellant thruster is nontoxic, clear, and clean. Monopropellant propulsion systems are scalable allowing for their use in multiple different spacecraft.

The disadvantage of monopropellant propulsion systems is maintaining the catalyst bed over the lifespan of the spacecraft [4]. Catalytic attrition occurs when fine particles of the catalyst bed is lost due to the over pressurization and thermal expansion of the catalyst bed crushing the catalytic pellets. Catalyst poisoning is the buildup of impurities found in the monopropellant in the catalyst bed. These catalyst bed problems lead to a decline of performance of a monopropellant propulsion system.

Monopropellant propulsion systems typically use hydrazine as their propellant [4]. Hydrazine has been used as monopropellant due to its ease of decomposition and long term storage capability. The catalyst bed for hydrazine is typically iridium on a porous alumina base, but several materials decompose the hydrazine if the catalyst bed is preheated. Hydrazine exothermically decomposes to gaseous ammonia and nitrogen then the ammonia endothermically decomposes to into nitrogen and hydrogen. Hydroxylammonium nitrate (HAN) has been proposed as an alternative to hydrazine due to its lack of toxicity and similar performance [11].

The MR-100 hydrazine monopropellant propulsion system developed by Redmond has been used by multiple spacecraft since 1974 [12]. MR-100s are used as attitude control thrusters on Voyager, Magellan, GPS, and several other spacecraft. The MR-100 produces a thrust of 1.12 N at a specific impulse of 227 sec. The MR-100 can perform 750,000 pulses altering a spacecraft’s attitude.

1.1.2.3 Bipropellant propulsion systems. Bipropellant propulsion systems are similar to the design and operation of liquid propellant rocket engines used for primary propulsion systems in launch vehicles. Bipropellant propulsion systems are used when high performance is need from the secondary propulsion system. The main disadvantage of bipropellant propulsion systems is the complexity of their design. These secondary propulsion systems typically use monomethylhydrazine and nitrogen tetroxide as their

propellants. The Space Shuttle Orbiter employed a bipropellant propulsion system for orbital maneuvering.

Bipropellant propulsion systems have a similar design to their larger versions used for primary propulsion systems [4]. A bipropellant propulsion system uses a series of propellant tanks to supply fuel and oxidizer to several thrusters. The propellant tanks are pressurized and a system is employed to manage the propellants in the void of gravity. The thrusters are similar to liquid propellant primary propulsion systems where fuel and oxidizer are injected into a combustion chamber where the propellants are ignited and the high temperature and pressure exhaust gas are expelled thermodynamically through a nozzle. These secondary propulsion systems typically use a thermal management system to deal with the heat produce during combustion [9].

Bipropellant propulsion systems primary advantage is the high level of performance they are capable of producing [4]. Bipropellant propulsion system typically can produce the highest level of thrust of any secondary performance system. These secondary propulsion systems typically have higher specific impulse than monopropellant or cold gas propulsion systems.

The disadvantage of a bipropellant propulsion system for secondary propulsion is the added level of complexity in their design and the thermal management of their operation [4]. The need for separate pressurized propellant tanks along with separate propellant lines and control valves adds a higher number of failure modes and an increase in development cost [9]. These secondary propulsion systems typically have a complex thermal management system to handle the heat produce during their operation.

Propellants used for bipropellant propulsion systems on spacecraft need to be able to be stored for long periods of time [9]. When high performance is required a combination of monomethylhydrazine (MMH) and nitrogen tetroxide (N_2O_4) are used as the fuel and oxidizer. This fuel and oxidizer combination can achieve specific impulses in excess of 300 sec.

The Space Shuttle Orbiter Orbital Maneuvering System (OMS) pods used a bipropellant propulsion system for orbital maneuvering, insertion, and re-entry [13]. The OMS uses MMH and N_2O_4 as its fuel and oxidizer combination. The OMS never failed or required replacement due to their simplicity. The OMS pods each contained a

gimbaled bipropellant engine. Each engine was capable of producing 26.7 kN of thrust at a specific impulse of 316 sec.

1.1.2.4 Solid propellant propulsion systems. Solid propellant propulsion systems used for secondary propulsion are similar to solid propellant rocket motors used by launch vehicles [4]. Some interceptor vehicles used for missile defense use a solid propellant propulsion system for attitude and orbital maneuvering. In this secondary propulsion system a central propellant grain is ignited then the high temperature and pressure exhaust gas is supplied to a series of thrusters. This type of secondary propulsion system allows for maneuvers requiring high thrust but only for a short period of time.

Solid propellant propulsion systems are used for orbital maneuvering of spacecraft when a high change in velocity over a short time frame is necessary [9]. Typical solid propellant propulsion is used on spacecraft that are spin stabilized to maintain the proper thrust alignment. In some geostationary satellites a solid propellant propulsion system is used to insert the satellite into its orbit. NASA's Pioneer 1 was equipped with a solid propellant propulsion system to insert it into a lunar orbit [3].

1.1.2.5 Electric propulsion systems. An electric propulsion system generates the kinetic energy used for thrust by the electric energy stored on the spacecraft [4]. Every electric propulsion system uses a raw energy source such as solar or nuclear power to generate electricity. A conversion device is used to transform the energy to the proper voltage, current, and frequency. A propellant management system is used to control, measure, and deliver the propellant to one or multiple thrusters. In the thruster the electric energy is converted to kinetic energy to control the attitude and maneuver the spacecraft. The power required to achieve certain specific impulse are shown in Figure 1.7.

Electric propulsion systems encompass both thermal and non-thermal secondary propulsion systems [4]. Electrostatic propulsion systems accelerate charge particles using the interactions of electrostatic fields. Electrothermal propulsion systems heat a propellant using electricity then expel the gas thermodynamically through a nozzle. Electromagnetic propulsion system accelerate a plasma using electric and magnetic fields

Electric propulsion systems have been proposed since the 1950s but it hasn't been since the mid-1990s that the onboard power supplies of spacecraft have been sufficient

[4]. The typical performance parameters of several types of electric performance are shown in Table 1.3. Electric propulsion systems produce low levels of thrust operating from weeks to years generating large changes in velocity. The advantage of electric propulsion systems is the very high specific impulse.

Table 1.3. Performance parameters of different types of electric propulsion systems [4].

Type	Thrust Range (mN)	Specific Impulse (sec)	Thruster Effciency (%)	Thrust duration
Resistojet	200-300	200-350	65-90	Months
Arcjet	200-1000	400-1000	30-50	Months
Ion Thruster	0.01-500	1500-8000	60-80	Years
Pulsed Plasma Thruster	0.05-10	600-2000	10	Years
Magnetoplasma Dynamic	0.001-2000	2000-5000	30-50	Weeks
Hall Thruster	0.01-2000	1500-2000	30-50	Months

1.1.2.5.1 Electrostatic propulsion systems. Electrostatic thrusters operate using Coulomb force to produce thrust [4]. These secondary propulsion systems accelerate ions to very high exit velocities. There are a couple of sources of charged particles used by electrostatic thrusters. Ion thrusters typically use electron bombardment to produce positive ions by bombarding a gas with electrons. These positive ions are then accelerated through a series of electrically conducting grids [14]. Field emission electric propulsion (FEEP) thrusters and electrospray thruster use positive ions supplied by a liquid source. When certain liquid metals are subjected to large electric fields molecular ions are produced and accelerated.

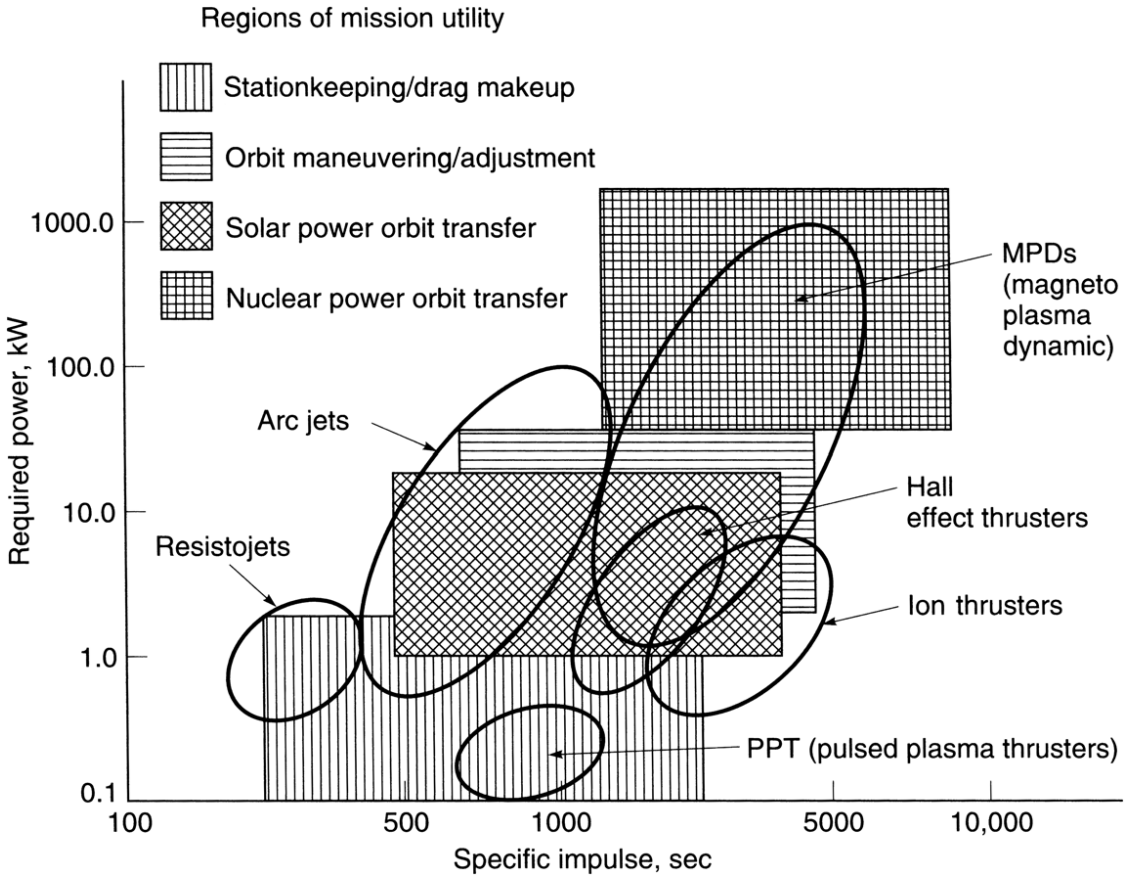

Figure 1.7. The region of mission utility with respect to power required and the specific impulse of different electric propulsion systems [4].

All electrostatic propulsion systems are comprised of same subsystems [4]. These subsystems consist of a propellant source, electric power supplies, an ionization chamber, an accelerator region, and a way to neutralize the exhaust plume to prevent a build-up of electric charge on the spacecraft. Neutralization of the charged particles is typically achieved downstream of the accelerator region by injection of electrons into the exhaust plume. The ionization chamber typically represents most of the mass, size, and efficiency of electrostatic propulsion systems.

Ion thrusters are the most common electrostatic propulsion system [4]. These electrostatic propulsion systems produce positive ions by bombarding a gas or vapor with

electrons from a cathode. Ion thrusters then accelerate ions through a series of electrical grids powered by a separate electrical power supply. A schematic of a simply ion thruster is shown in Figure 1.8. Ion thrusters have high thruster efficiencies, typically between 60% to 80%, and a high specific impulse ranging from 2,000 sec to upwards of 10,000 sec [14].

There are several different ways to ionize the propellant in an ion thruster [14]. A typical DC electron discharge generator uses an anode potential discharge chamber and hollow cathode electron source. A small amount of propellant is injected into the hollow cathode with the remainder injected into the discharge chamber. The propellant is ionized by the electrons emitted by the cathode. Typically a form of magnetic confinement is

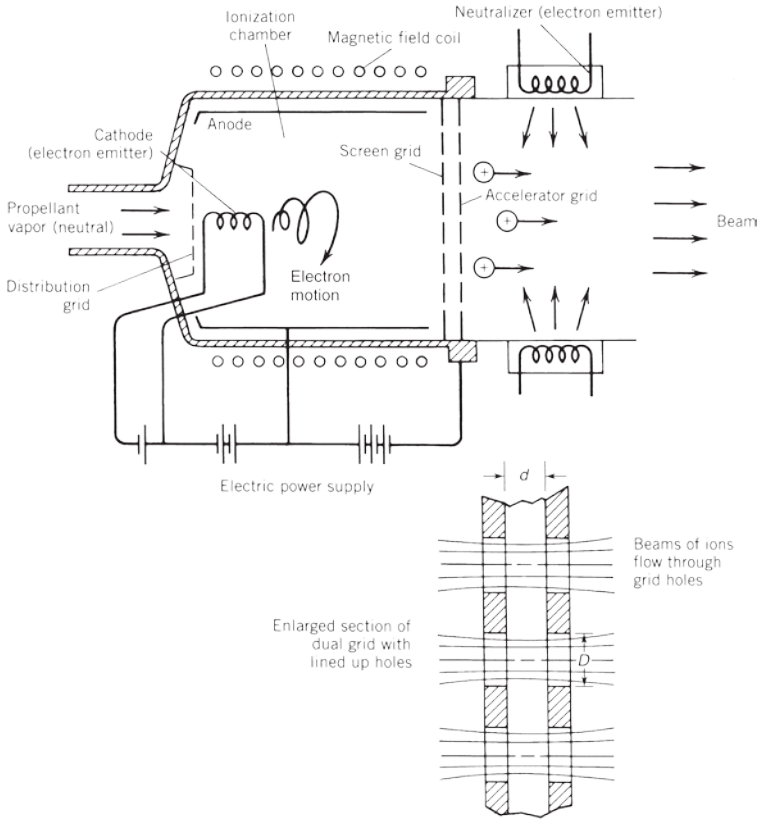

Figure 1.8. Schematic of a simply ionic thruster [4].

used to keep the electrons form interacting with the wall decreasing efficiency. Other ionization schemes include RF and microwave systems.

Xenon is the typical propellant of ion thrusters [4]. Xenon is a rare and expensive propellant that is both stable and inert gas with a high molecular weight. Xenon can be stored as liquid if kept below its critical temperature.

FEEP and electrospray thrusters produce positive ions by extracting ions from a liquid metal, like indium or cesium, or ionic liquids under a high electric field [15,16]. The performance of FEEP thrusters is dependent on the emitter and electrode geometry, material, and operating voltage [15]. Electrospray thrusters are a type of electric propulsion system that extracts positive or negative ions at high velocity from a liquid [16]. Ionic molecules and small clusters of ionic particles are emitted by electrospray thrusters. FEEP thrusters have been proposed for micro-propulsion space application and can achieve specific impulses upwards of 9000 sec. These electrostatic propulsion systems wick a liquid to the end of sharp needles where the ions are extracted ions by large electric fields [14]. FEEP and electrospray thrusters produce very low levels of thrust making them only suitable for precise attitude control of a spacecraft.

1.1.2.5.2 Electrothermal propulsion systems. Electrothermal propulsion systems generate thrust by heating propellant using electrical energy [4]. These electric propulsion systems typically have the simplest power conditioning. The two main types of electrothermal propulsion system are resistojets and arcjets. Resistojets heat propellant by heat transfer using electrical resistance to generate heat. Arcjets heat the propellant to much higher temperature than resistojets by passing an electrical discharge through the propellant.

Resistojets are the simplest of the electrothermal propulsion systems [4]. These electric propulsion systems pass a propellant through coils, fins, or other geometry optimized for heat transfer. The propellant is heated through conduction, convection, and radiation and then expelled thermodynamically through a nozzle producing thrust. Electrothermal propulsion systems must be supplied by a pressurized propellant tank designed for operation in the gravity free environment of space. There is no special power conditioning requirements for resistojets. The maximum temperature that the

propellant can achieve is dependent on the material properties of the heating element and thrust chamber.

Resistojets can use virtually any propellant due to the way in which they operate [4]. Propellants that have been used by resistojets are O_2, H_2O, CO_2, NH_3, CH_4, and N_2. Resistojets have also been used to increase the performance of hydrazine monopropellant propulsion systems. When used after the decomposition of hydrazine the exhaust gas temperature can be raised from 700°C to an even higher temperature.

The performance of resistojets is dependent of the molecular mass and exhaust temperature of the exhaust gas [4]. The performance of a typical resistojet decease as the flow rate of propellant increases. The thruster efficiency of these electrical propulsion system ranges between 65 and 85%. Resistojets have higher thrust to power required than other electric propulsion systems due to low specific impulse and high thruster efficiency. The lack of complicated power conditioning results in resistojets having a low overall system mass.

Arcjets produce thrust by pass an electric current direct through the exhaust gas increasing its temperature as it is expelled thermodynamically through a nozzle [4]. A schematic of an arcjet is shown in Figure 1.9. Arcjets overcome the material temperature

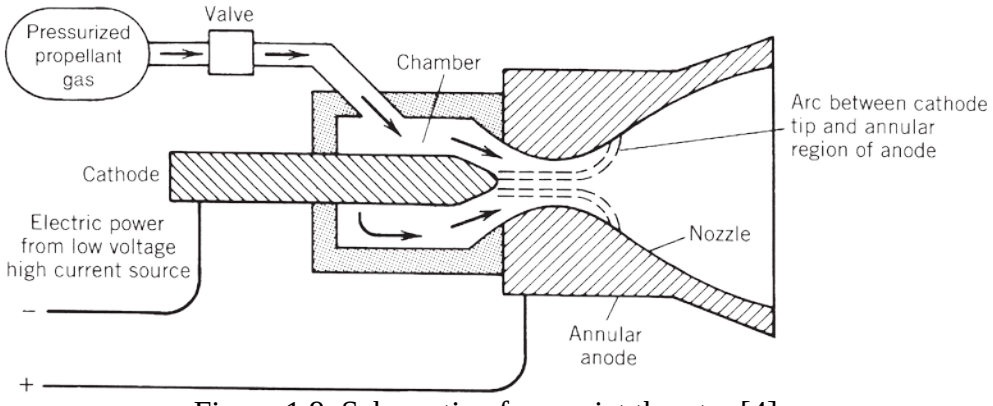

Figure 1.9. Schematic of an arcjet thruster [4].

limitation imposed on resistojets by directly heating the propellant. The simple design of arcjet thrusters consist of a central cathode and an anode incorporated into the structure of the nozzle. In an ideal arcjet the electrical arc attaches right after the throat but this configuration is difficult to achieve. In practice the electrical arc moves around frequently with voltage and mass flow rate and only typically heats the small portions of exhaust gas to very high temperatures. The small portion that has been heated to high temperature then mixes with the remainder of the exhaust gas.

Arcjets provide a higher level of performance compared to resistojets [4]. Arcjets typically produce six times the thrust-to-power ratio of resistojets. These electric propulsion systems are also scalable to produce high levels of thrust. Arcjets can also be incorporated into monopropellant hydrazine thruster improving their performance.

The local erosion of the electrode can severely limit the overall lifespan of these electric propulsion systems [4]. The local erosion of the electrode in arcjet thruster is caused by the high operating temperature of the arc attachment locations. Arcjets also require complicated power conditioning to start and maintain the high voltage electrical arc. Less than half of electrical power is transferred into kinetic energy with upwards of 20% being dissipated into space as heat.

1.1.2.5.3 Electromagnetic propulsion systems. Electromagnetic propulsion systems uses electric and magnetic field to accelerate plasma to high velocity producing thrust [4]. Plasma is a mixture of electrons, positive ions, and neutral particles. Electromagnetic propulsion systems typically produce a neutral exhaust beam. The thrust density of electromagnetic propulsion systems is typically 10 to 100 times greater than electrostatic propulsion systems.

Pulsed plasma thrusters (PPT) are the simplest electromagnetic propulsion system [4]. During a pulse a PPT accelerates plasma using Lorentz force cause by an electric and self-induced magnetic field, shown in Figure 1.10. PPT electrodes consist of an anode and cathode either in a pair of parallel rails or in a coaxial configuration. The propellant, typically Teflon, is pressed against the electrodes. An electrical discharge is sparked between the electrodes ablating a layer of the propellant. The plasma is then accelerated by an electric field created by the discharge of a capacitor bank through the plasma along with the magnetic field created by the accelerating plasma.

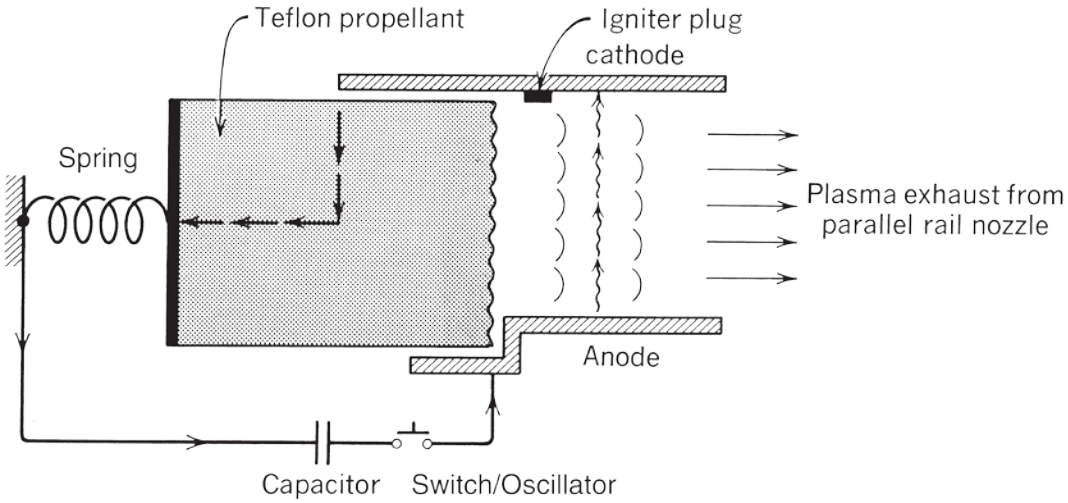

Figure 1.10. Simply diagram of a PPT's propulsion process [4].

PPTs are ideal for small spacecraft with limited power supplies [17]. The power supplies for PPT are typically below 100 W with no loss in performance. PPTs operate in a pulsed fashion generating small impulse bits usefully for attitude control of a spacecraft. The overall efficiency of a PPT is very low with few achieving over 10%. The loss in efficiency is due to several reasons. First, a PPT typically efficiently transfers the stored electrical energy in the capacitor bank into the kinetic energy of the plasma. Second, the ablative process results in a low mass utilization because of late time ablation and large solid portions of the propellant being ejected.

Magneto-plasma-dynamic (MPD) thruster is similar in design to an arcjet thruster [4]. In a MPD a high current arc ionizes a significant portion of the propellant then the Lorentz force is used to accelerate the electrically charge propellant [14]. These electromagnetic propulsion systems typically operate at very high power levels generating a high specific impulse and thrust.

Hall-effect thrusters consist of a cylindrical channel, an interior anode, a radial magnetic field, and an exterior cathode [14]. Hall-effect thrusters rely on more complex physics than electrostatic propulsion systems. These electromagnetic propulsion systems

typically have lower thruster efficiency and specific impulse than electrostatic propulsion system but offer a higher thrust-to-power ratio and require less power supplies.

1.2. THESIS FORMAT

The Introduction section is followed by three main sections that are broken down as such:

2. Liquid Pulsed Plasma Thruster Plume Analysis – Covers the investigation of the plasma generated by a liquid pulsed plasma thruster. This section includes a review of plasma plume analysis and the recent developments of liquid pulsed plasma thrusters. It also includes a description of design and operation of the Digital Solid State Propulsion's liquid pulsed plasma thruster. The section ends with a review of the experimental methodology employed in examining the plasma plume generated, the results of the experiments, and a discussion of their implications.

3. MR SAT Propulsion System Performance Review – Covers a description the propulsion system used by MR SAT. A review of the previous analysis and experimental results performed by the Missouri Satellite Research Team. A description of the Multiple Point Choked Flow analysis employed to improve the thrust prediction. An examination of the accuracy of the improved analysis of the MR SAT thrust performance.

4. Conclusion – A review of the lessons learned over the course of this research. A discussion of the plasma plume generated by a liquid pulsed plasma thruster. A review of the capability of the Multiple Point Choked Flow to accurately predict cold gas propulsion system performance.

2. LIQUID PULSED PLASMA THRUSTER PLASMA PLUME ANALYSIS

To full understand how a plasma propulsion system or thruster operates the plasma plume generated needs to be investigated to determine if the theoretical predicted plume matches with the experimentally measured one. There are several ways to investigate a plasma plume for properties such as ion current density, electron temperature, plasma species, electron density, etc. Missouri University of Science and Technology (MS&T) has investigated plume properties of a prototype of a liquid pulsed plasma thruster (LPPT) developed and supplied by Digital Solid State Propulsion (DSSP).

2.1. LITERATURE REVIEW

A review of plasma plume analysis is necessary before proceeding further. Plasma plume analysis is the measuring the properties of the plume created by a plasma generating system. The multiple different techniques for plasma plume analysis have been applied to characterizing the plasma generated by a PPT. An area of particular interest is the analysis performed by Matthew Glascock on a similar electric micro-thruster. The recent progress in the development of LPPT is needed to add context to the analysis to follow.

2.1.1. Plasma Plume Analysis. Plasma plume analysis is the characterization of the plasma emitted by a steady or unsteady source through the use of probes and other diagnostic equipment [18-27]. The main purpose of plasma plume analysis is to determine the electron temperature (T_e), electron number density (n_e), ion current density (J_i), ion velocity (u_i), and the plasma species as these parameters vary with geometry and time. There is a number of different ways to measure these parameters and their distributions including nude Faraday probes (NFP), magnetically filtered Faraday probe, Langmuir probes, high speed photography, retarding potential analyzers, residual gas analyzer, etc.

2.1.1.1 Nude Faraday probe. A NFP is a crude plasma diagnostic tool that allows for an initial look at a plasma's J_i [18]. The NFP used by the APLab consist of a center collector surrounded by a shielding ring, shown in Figure 2.1. Both the collection and shielding ring are equally negatively biased by separate power supplies. NFP are highly susceptible to vacuum chamber geometry and back pressure making comparisons between similar experiments conducted at different facilities problematic [19]. Orientation of the NFP with respect to the thruster will also skew the probe's measurements. The advantage of a NFP is that its simplicity allows for an initial examination of the J_i with respect to time by

Figure 2.1. The APLab's NFP mounted in the vacuum facility [27].

$$J_i(t) = \frac{I_p(t)}{A_C} \tag{2.1}$$

where I_p is the measured current coming from the collector with respect to time and A_c is the area of the collector plate. There are a number of ways to improve the accuracy and decrease distortions from back pressure such magnetically filtering the ion stream [26].

2.1.1.2 Langmuir triple probe. A Langmuir triple probe (LTP) is a highly sensitive device that allows for simultaneous measurements of the T_e and n_e. A LTP is three Langmuir probes in a single housing [18,20,23,25]. A Langmuir probe simply consists of a wire, typically made out of tungsten, inside of an insulator that is biased at different potentials to determine properties of a plasma plume [27]. When three are placed in the same insulator and biased differently (one floats, one negatively biased, and one positively biased), referred to as the voltage-mode, they allow for the properties of the plasma plume to be measured based on the voltage difference between probes ($V_{d,2}$ and $V_{d,3}$) and the current measured off the negatively biased probe (I_3) [25]. The LTP allows for measurements of T_e and n_e by solving

$$\frac{1}{2} = \frac{1 - exp\left(-\frac{V_{d2}}{T_e}\right)}{1 - exp\left(-\frac{V_{d3}}{T_e}\right)} \tag{2.2}$$

and

$$n_e = \frac{m_i^{0.5}\left(\frac{I_3}{A_3}\right)1.05 \times 10^9}{(T_e)^{0.5}\left(exp\left(\frac{V_{d2}}{T_e}\right) - 1\right)} \tag{2.3}$$

where m_i is the ion mass and A_3 is the area of the third probe [18].

2.1.2. PPT Plasma Plume Analysis. Plasma Plume analysis has been used multiple times to examine multiple plasma plume parameters. Typically these experiment have examined the T_e and n_e with respect to the spatial location around the PPT. These experiments include plasma plume analysis using Langmuir triple probes, quadruple Langmuir probes, high speed photography, spectroscopy, interferometry, etc.

2.1.2.1 Eckman, et al. Eckman, et al. used a Langmuir triple probe to interrogate the plasma plume generated by a PPT [20]. The scope of their investigation focused on the T_e and n_e at different spatial locations and discharge energies. The experiments were conducted on the NASA Lewis laboratory model PPT.

The Langmuir triple probe consisted of three tungsten wires with a diameter of 0.25 mm and a length of 9 mm protruding from their alumina housing [20]. The probe was operated in what is referred to as the voltage mode. A glow discharge was used to clean the Langmuir triple probe of contamination form the PPT. The probe recorded data at locations from 6 to 20 cm from the Teflon surface and at angles between 0 to 40˚ from the centerline in both parallel and perpendicular to the electrode plane.

The experiment shows that as the distance from the Teflon propellant increases past 14 cm the n_e decease substantially but the T_e remains relatively unchanged [20]. The T_e of the bulk plasma allows remained around 3 eV. The maximum electron density was found to range from 1.7 x 10^{20} to 3.5 x 10^{20} m^{-3}.

2.1.2.2 Kumagai, et al. Kumagai, et al. used high speed photography along with a contamination study to examine the plasma plume of created by a PPT [22]. The scope of the investigation focused on the shape of the plasma with respect to time and the level of contamination on a plate downstream of the PPT. The experiments were performed on the TMIT-PPT.

A high speed camera was used to capture 16 pictures over the duration of the plasma discharge [22]. The pictures for the high speed photography were captured at 4,000,000 pps at an exposure time of 20 nsec. The images highlight the complex architecture of the plasma discharge created by a PPT.

To examine the possible contamination on a spacecraft from a PPT by placing 20 aluminum foil strips on an aluminum plate placed 1,100 mm from the thrusters exit [22]. 500,000 pulses were fired form the 2.3 J PPT at the aluminum plate. The aluminum foil strips were analyzed and found that no more than 0.2 ng per pulse was deposited by the PPT.

2.1.2.3 Schönherr, et al. Schönherr, et al. used optical emission spectroscopy and Mach-Zehnder interferometry (MZI) to investigate the plasma generated by a PPT [28]. The scope of their investigation focused on the T_e, n_e, and the Knudsen number as

they vary with time, space, and discharge energy. The experiments were performed on an engineering model of an ADD SIMP-LEX PPT.

Optical emission spectroscopy is suitable for determining a PPT's plasma plume as a function of time, space, discharge voltage, and main capacitance [28]. The spectrometer used had a wavelength range of 232-828 nm. The CCD camera used a virtual exposure time of 500 nsec and several spectra were recorded at nine points over the 12 μsec pulse.

MZI has been applied to highly transient plasma but has rarely been used to investigate PPT plasma plumes due to the low n_e [28]. A two wave-length MZI using two lasers as probe lights was used during this experiment. One beam passed through the plasma whereas the other remained uninfluenced. Interference pattern is created by inflicting an optical retardation of the beams and is recorded by a high-speed camera.

The T_e was found to between 1.7 to 3.1 eV [28]. The maximum n_e was found to be 10^{17} cm^{-3}. Both of these measurements were found to be strongly dependent on discharge voltage and proximity to the electrodes while capacitance and time had less influence. A continuum flow behavior of the bulk plasma was determined based on the calculated Knudsen number in the order of 10^{-3}-10^{-2}.

2.1.2.4 Li, et al. Li, et al. developed a current-model Langmuir triple probe to measure the plasma plume generated by a PPT [29]. The scope of their investigation of the plasma plume of PPT focused on the T_e and n_e at different spatial locations and discharge energies. A single channel parallel plate PPT was designed and built that used PTFE as the propellant. The discharge energies were varied between 6-24 J.

The current-mode Langmuir triple probe consisted of three tungsten wires in an alumina housing [29]. The probe tips were 0.2 mm in diameter and 0.5 mm long. The Langmuir triple probe was place 10 to 20 cm from the thruster exit at radial locations 0-40˚ off the centerline with respect to both perpendicular and parallel planes of the electrodes.

The current-model Langmuir triple probe measured T_e between 0.6 to 5.4 eV [29]. The n_e was found to vary from 10^{19} to 10^{21} m^{-3}. The T_e and n_e show the trend of deceasing as the angle from the centerline increased and with decreasing discharge energy.

2.1.2.5 Parker. Parker analyzed a PPT using an energy analyzer coupled with a drift tube [30]. The scope of the investigation focused on the exhaust velocity of ions at different energies. The plume analysis was performed on a 5.2 J micro-PPT supplied by Dawgstar.

The gridded energy analyzer uses four grids upstream of a collector plate [30]. The first grid decreases the plasma density. The second grid is negatively biased to repel electrons. The third grid repels ions below certain energy by positively biasing to variable voltage. The forth grid is negatively biased to repel electrons from ion collisions with the third grid. The collector plate then collects the ions of sufficient energy to pass through all the grids.

The fastest ions to reach the collector plate were found to have a u_i of 73.6 km/sec [30]. The fastest ions to reach the positive grid were found to have a u_i from 55 to 105 km/sec.

2.1.2.6 Gatsonis, et al. Gatsonis, et al. performed a plasma plume analysis on a PPT using a quadruple Langmuir probe [31]. The scope of their investigation focused on the T_e, n_e, and the ion-speed ratio at different spatial locations and discharge energies. The plasma plume analysis was performed on a parallel plate laboratory model Teflon PPT.

The quadruple Langmuir probe consists of an ordinary Langmuir triple probe with an additional crossed-probe, an electrode place perpendicular to the plasma [31]. All the electrodes were made out of 0.127 mm diameter tungsten wires with 6 mm exposed from their alumina housing. The PPT was tested at discharge energies of 5, 20, and 40 J. The probe took measurements at several different radial positions and angle with respect to the Teflon propellant centerline.

The maximum T_e of 11.5 eV was record slightly before the maximum of the discharge current [31]. A maximum ion-speed ratio of 2.53 was recorded resulting in an estimated maximum u_i of 15 km/sec. The T_e shows little variation in either angular direction but decreases with increasing radial distance. The n_e is greatly affected by angular direction especially as the radial distance increases.

2.1.3. High Performance Electric Monopropellant. MS&T has previously studied an electric solid propellant system that function similar to a coaxial PPT [18]. The APLab at MS&T performed a series of experiments to interrogate the plasma plume.

High Performance Electric Propellant (HiPEP) supplied by DSSP was incorporated into a micro-thruster [18]. The chemical composition of HiPEP is shown in Table 2.1. HiPEP is a HAN based propellant that is manufactured in benign processes resulting in a relatively safe to handle and work with solid propellant. This solid propellant is insensitive to ignition through spark, impact, or open flame.

The HiPEP coaxial micro-thruster is designed for small spacecraft [18]. The HiPEP propellant is cured between the outer electrode and a central inner electrode. The dimension of the micro-thruster is a 1 in long by 1/8 in diameter cylinder. This electric propulsion system is operated in short pulse of about 0.5 msec. A relatively low voltage discharge of 300 V ablates a thin layer of the HiPEP which is then expelled from the micro-thruster. Unlike the typical Teflon propellant of PPTs, HiPEP has a much better electrical conductivity leading to questions about how analogous this micro-thruster is to a PPT.

Table 2.1. Chemical composition of High Performance Electric Monopropellant.

Chemical Name	Chemical Formula	Percentage (by Mass)	Molecular Mass [g/mol]
Ammonium Nitrate	NH_4NO_3	5%	80
Hydroxyl Ammonium Nitrate	$H_4N_2O_4$	75%	96
Polyvinyl Alcohol	C_2H_4O	20%	44

The plasma plume generated by the HiPEP micro-thruster was investigated using a series of experiments [18]. A NFP mounted on the translation table inside of the vacuum testing facility allowed for a rough estimate of the J_i at several centerline and radial positions. An array of five single Langmuir probes was used to take measurements

of several predetermined locations. A Langmuir triple probe was used to verify the results obtained by the other plasma plume diagnostic probes. Finally a residual gas analyzer was used to examine the gas species present in the plume.

At 5 cm from the exit of the thruster the NFP measured an peak J_i of approximately 230 mA/cm^2. As the NFP was moved to 10 and 15 cm from the thruster exit the max J_i dropped to 190 mA/cm^2 and decreased even further as the distance increased. The mass bit was determined by measuring the weight of the micro-thruster before and after each experimental run and was determined to be approximately 250 μg. The estimate for ionization fraction was between 0.01% and 0.2%. When compared to traditional PPTs the HiPEP micro-thruster had a lower J_i, T_e, n_e, and ionization fraction and slightly larger mass bit.

2.1.4. Experimental Liquid Pulsed Plasma Thrusters. To date there is no flight heritage of any LPPT concept but several have been proposed and studied in the lab [32]. These electric propulsion systems have been speculated as a way to improve the thruster efficiency of PPT since the 1960s. Water and lithium based propellants have theoretically been shown to have higher exhaust velocity and thruster efficiency compared to PTFE. Experiments have shown that water based LPPTs have a lower T_e, n_e, impulse bits, and peak discharge current but higher thruster efficiency and specific impulse. LPPTs remain an active area on research.

Several liquids have been considered as propellants use in LPPTs [32]. These liquid propellants include mercury, lithium, cesium, methanol, ethanol, buthanol, gallium, DME, and water. Water has remained the favorite due to its ease of use, availability, and performance. The main challenge for LPPTs has been accurate control of the liquid propellant feed system.

The optimal design of a LPPT is speculated to incorporate a few key parameters to achieve a propulsion system that has a higher specific impulse, thruster efficiency, and propellant utilization [32]. The electrodes should be a rectangular configuration rather than coaxial. A preheated water propellant seed with sodium chloride provides the highest impulse bit per power input. A self-controlled passive propellant feed system that incorporates a porous ceramic medium provides the highest thruster efficiency and specific impulse.

An example of a LPPT was created and tested at the University of Tokyo [33]. This LPPT concept used water, methanol, ethanol, and butanol as its propellant. A small solenoid valve was used to control the propellant supplied into the discharge chamber. A pair of parallel electrodes discharged a current through the propellant which is expelled producing thrust. The LPPT created by University of Tokyo produced an impulse bit of 80.0 μNs, a specific impulse of 4300 sec, and a thruster efficiency of 13% at a mass bit 2.8 μg and discharge of 14 J which is comparable to a typical PPT. This LPPT was only studied using a thrust stand which does not give indications of the properties of the plasma plume generated.

2.2. TESTED LPPT

A prototype LPPT that is different than previous developed systems was tested. The main difference with the previous LPPTs is the design of the discharge chamber. Typical LPPTs use long parallel electrodes to accelerate the plasma generate whereas the tested LPPT uses only small parallel electrodes that are only as wide as the wires entering the discharge chamber. The LPPT's electrical discharge is supplied by a Multiple Energy Discharge Controller (MEDiC). The solenoid control valve is controlled by a Valved Liquid Actuation Device (VLAD) which allow for precise user determined actuation times. Green Electric Monopropellant (GEM 10T) is used in the LPPT.

2.2.1. Design of the LPPT. The LPPT, shown in Figure 2.2., consists of a gravity fed propellant system, a propellant flow control solenoid valve, and a discharge chamber that consists of parallel electrodes [34]. The propellant tank is positioned on the top of the thruster assembly and is baffled allowing for the equalization of the pressure inside of the propellant tank and the vacuum facility. The propellant tank is filled approximately 2/3 full to generate the proper head pressure to supply propellant to the discharge chamber when the control valve is actuated. Two stainless steel cylindrical electrodes pass through the top and bottom of the cylindrical discharge chamber. The electrical discharge is supplied by a separate power supply.

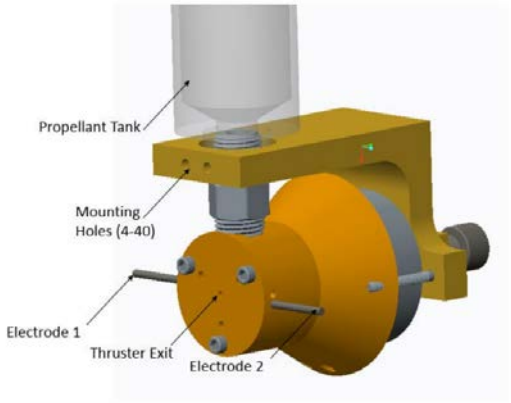

Figure 2.2. CAD model of the LPPT [34].

2.2.2. MEDiC. The LPPT's electrical discharge used to generate plasma is supplied by the MEDiC [35]. MEDiC was designed to test the performance of the micro-thrusters under varying discharge energies. The different discharge energies are achieved by varying the output voltage and capacitance level. There are five capacitance levels ranging from 100 to 500 μf (± 5%) in 100 μf intervals. The voltage of MEDiC can be varied from 50 to 390 V. The MEDiC must be operated in a vacuum of less than 50 μTorr and requires a separate power supply operating between 5 to 10 V. The typical energies used for micro-thruster testing are shown in Table 2.2.

Table 2.2. Typical MEDiC energies for use with micro-thrusters [35].

	Level 1	Level 2	Level 3	Level 4	Level 4
200 V	2	4	6	8	10
250 V	3.12	6.25	9.38	12.5	15.93
300 V	4.5	9	13.5	18	22.5
350 V	6.31	12.25	18.38	24.5	30.63
390 V	7.61	15.2	22.82	30.42	38.03

2.2.3. VLAD. VLAD is a small device that allows for precise, user defined, actuation times of solenoid valves [36]. VLAD was specifically developed to operate with this LPPT. VLAD is kept in atmosphere and allows for real time control over how the LPPT operates in a vacuum facility. VLAD can be either push button operated or connected to a computer. The actuation times are controlled by flipping on-board dip switch to a specific value. Each switch represents a specific value, shown in Table 2.3., and the total actuation time is the sum of all dip switch set on. VLAD allows for actuation times between 5 and 1,275 msec.

Table 2.3. VLAD actuation duration time settings [36].

Switch position	1	2	3	4	5	6	7	8
Duration Value (msec)	5	10	20	40	80	160	320	640

2.2.4. GEM 10T. The LPPT was operated with GEM 10T as its liquid propellant [34]. GEM 10T is a HAN based liquid propellant, that is insensitive to spark, impact, or open flame ignition making a relative safe propellant to transport and handle [36]. It is highly corrosive to some metals and can cause skin irritation so gloves are required when handling this propellant. GEM 10T chemical composition is shown in Table 2.4. It is primarily HAN with the bulk of the remainder a combination of ammonium nitrate, 1,2,4-trazole, and sugar alcohol. GEM 10T will absorb water out of the atmosphere which will evaporate out of the propellant tank when placed in a vacuum facility. The similarities in the chemical composition of the GEM 10T to HiPEP allows for a qualitative comparison of results with Matthew Glascock's HiPEP micro-thruster analysis.

Table 2.4. Chemical composition of GEM 10T [36].

Chemical Name	Chemical Formula	Percentage (by mass)	Molecular Mass [g/mol]
Ammonium Nitrate	NH_4NO_3	0.5-10%	80
Hydroxyl Ammonium Nitrate	$H_4N_2O_4$	65-75%	96
1,2,4-triazole	$C_2H_3N_3$	5-15%	69
2,2-dipyridyl	$C_{10}H_8N_2$	NA	156
Sugar Alcohol	NA	7-12%	NA
Water	H_2O	0.5-3.0%	18

2.3. EXPERIMENTAL METHODOLOGY

The plasma plume experiments were conducted during the summer of 2016 in the large vacuum facility in the Aerospace Plasma Laboratory (APLab) at MS&T at operating pressure between 40 to 50 μTorr. A series of experiments were conducted on the LPPT using a LPT, a NFP, and a mass analysis scheme. The LPPT mounts to the inside of the main vacuum facility's main hatch.

2.3.1. LPPT Experiment Procedure. All experiments performed on the LPPT followed a similar procedure. The procedure consists of filling the LPPT with propellant and setting up the experiment. The next step is pumping down the vacuum facility to the proper vacuum environment to conduct experiments. Then the experiment is conducted and data is collected. Next the vacuum facility must be safely returned to atmospheric conditions. Finally, the excess propellant is removed from the LPPT and any expelled GEM 10T is cleaned off the probes and vacuum facility.

The experiments begin by removing the GEM 10T form the fireproof locker where propellants are stored in the APLab. The tape seal around the cap of GEM 10T storage bottled is removed and saved. Approximately 18 g of GEM 10T is poured into a beaker, mass is recorded, the cap is replaced on the propellant storage bottle, the tape seal

reapplied, and the propellant storage bottle is placed back into the fireproof locker. The baffle is removed from the LPPT propellant tank and the propellant is poured in. The baffle replaced on the propellant tank and the beaker is weighed again to determine the initial mass (m_i) of propellant. The LPPT is mounted to the main hatch of the vacuum facility and the leads are connected to the electrodes and the VLAD controls are connected.

With the LPPT mounted in the vacuum facility the process of obtain the proper vacuum environment begins. The hatch is latched shut and the retaining clips for the hatch seal removed. A new vacuum run is started on the vacuum facility control program and proper pump down procedure is followed. It takes between three to four hours for the vacuum facility to pump down to the operating pressure of below 50 μTorr. During this time the vacuum facility controls need to be monitored to make sure the cooling systems is functioning properly. This is especially true once the diffusion and backing pumps due to high temperature they operate at. During the course of experiments the cooling system temperature is check periodically.

Once the proper vacuum environment is achieved the experiment can commence. Typically an experimental run will consist of hundreds of pulses of the LPPT. Each pulse consist of instructing the MEDiC to charge which takes from a few seconds to over a minute depending on energy setting. Once the MEDiC is charged the VLAD is used to actuate the control valve supplying propellant into the discharge chamber. The MEDiC is then instructed to discharge triggering the oscilloscope to record data. The data is then extracted from the oscilloscope using LabVIEW where it is then labeled and exported to the APLabs archive. This process is then repeated until a sufficient number of pulses have been recorded. The data is then imported, filtered, and analyzed by MATLAB algorithms.

Once the experiment has ended the diffusion pumps are shut down and the vacuum facility cool down process begins. The vacuum facility must return to a safe temperature before it can be vented from the atmosphere. This process takes approximately two hours. Once a safe temperature has been achieved the vacuum facility is vented, the retain clips re-inserted, and the hatch is opened.

The LPPT is disconnected is disconnected from the MEDiC and VLAD and unmounted from the inside of the hatch. A clean beaker is the weighted and the mass recorded. The baffle is removed and the propellant is allowed to drain for a couple minutes into the beaker. The beaker is then re-weighed to determine the final mass (m_f) of propellant. Finally the LPPT, the beaker, the vacuum facility, and any probes used are then cleaned with water and alcohol to remove any excess GEM 10T.

2.3.2. Langmuir Triple Probe. The first experiment performed on the LPPT was a variable operating energies investigation using a LTP positioned approximately 5cm from the exit of the thruster to evaluate its performance, shown in Figure 2.3. During these experiments the VLAD was set to 200 msec. A variety of energy levels from 7.61 to 23.82J was explored.

The LTP is mounted to the translation table and the LPPT is mounted to the door of the vacuum facility. The LTP was operating in voltage mode where one of the electrodes is negatively biased, another electrode floats, and the final electrode is positively biased to determine the T_e and n_e of the plasma plume generated by the LPPT.

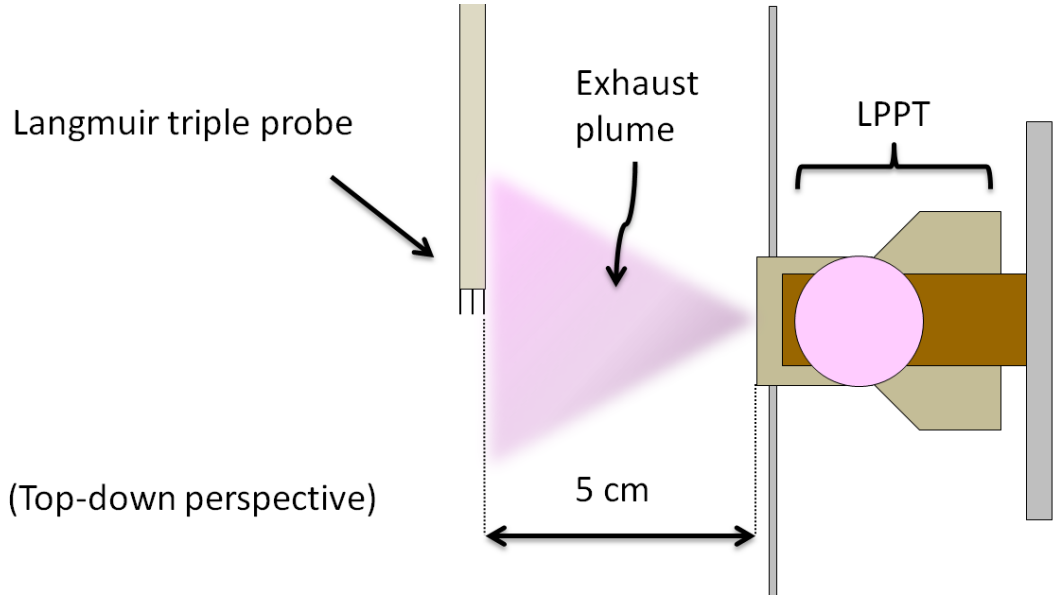

Figure 2.3. Schematic of the LPT experiment conducted on the LPPT.

2.3.3. Nude Faraday Probe. The bulk of the plasma plume analysis was performed using the APLab's NFP, shown in Figure 2.4. The NFP was position approximately 10cm from the exit of the LPPT's discharge chamber. The collector plate is roughly 2.54 cm in diameter resulting in an A_c of approximately 5 cm^2. Both the collector plate and the shielding ring are negatively biased to 28 V (± ½ V).

An initial survey of the ten pulses at a large number of the typical operating energies was performed to determine the energy setting that produce the highest level of repeatability. The initial survey allows for a rough estimate of the plasma plume characteristics. It does not give a true representation of the plasma plume at the investigated energies and was only used as a guide.

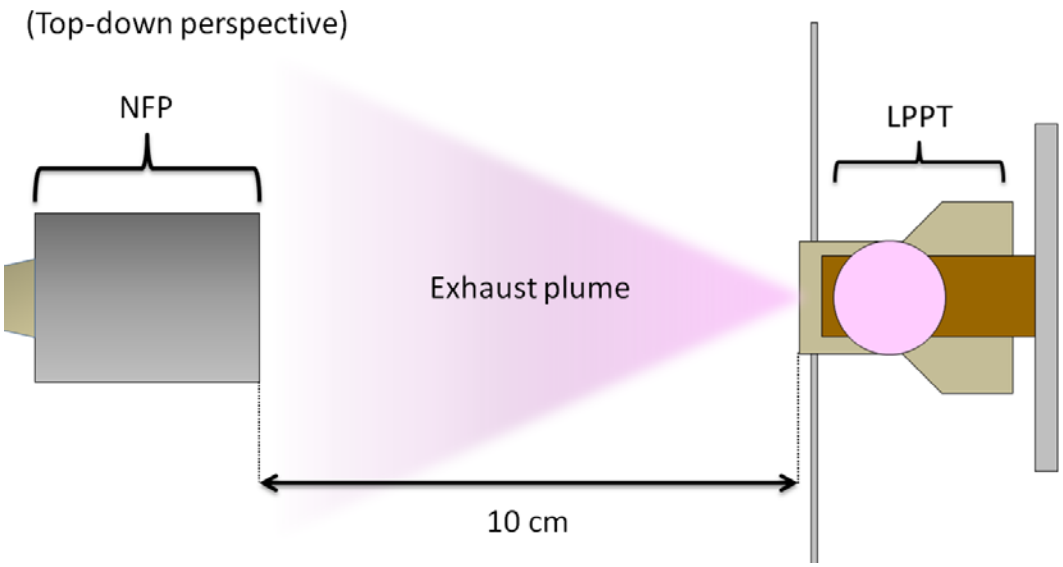

Figure 2.4. Schematic of the NFP conducted on the LPPT.

Following the initial survey a number of experiments analyzed the plasma plume at several operating energies at the 390 voltage setting and varying valve timings on the VLAD. The experiments looked for consistency of the $J_{i,max}$ at these varying settings. The major focus of the consistency analysis was on the mean $J_{i,max}$ of a large number of pulses along with the standard deviation and the standard deviation relative to the mean. Secondary focus of the consistency analysis was on the time of the $J_{i,max}$, the maximum discharge current to the LPPT, the time of the maximum current to the LPPT, start time of the $J_{i,max}$, and the difference between the maximums which is used to estimate the time of flight (t_f). With an estimate for t_f determined a prediction for u_i by:

$$u_i = \frac{x}{t_f} \tag{2.4}$$

where x is the distance the plasma plume traveled.

2.3.4. Propellant Mass Investigation. Following the NFP experiment an attempt was made to determine the amount of liquid GEM 10T being expelled, m_{expel}, from the LPPT during a pulse along with the quantity of GEM 10T being leaked, m_{leak}. The liquid mass investigation, shown in Figure 2.5., consisted of a beaker position to catch the majority of the GEM 10T expelled during a pulse and a dish to catch the GEM 10T leaked from the LPPT during its time in the vacuum chamber.

The initial mass of GEM 10T, m_i, is measured in a beaker before being added to the LPPT. Following each experiment the GEM 10T was once again measured in a beaker to determine the final mass, m_f. The m_{leak} was directly measured in several experiments and in others it is assumed. To determine the amount of GEM 10T that is being expelled as liquid, m_{liquid}, the liquid catch is used. To determine the amount of the GEM 10T expelled as gas, m_{gas}, the following equation is used:

$$\begin{aligned} m_i = m_f + m_{used} &= m_f + m_{leak} + m_{expel} \\ &= m_f + m_{leak} + m_{liquid} + m_{gas} + m_{plasma} \end{aligned} \tag{2.5}$$

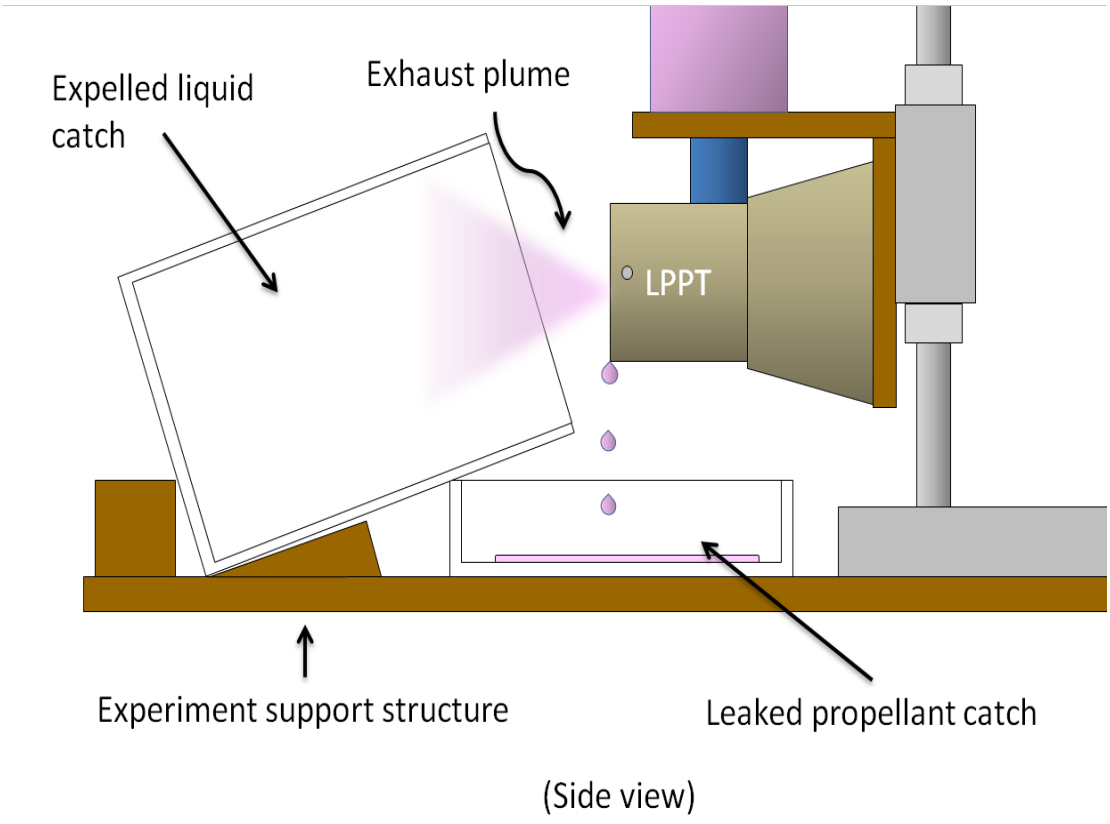

Figure 2.5. Schematic of the liquid mass investigation.

where the mass of GEM expelled as plasma, m_{plasma}, is assume negligible. The average mass bit is then by:

$$m_{bit} = \frac{m_{gas}}{n} \tag{2.6}$$

where n is the number of pulses.

2.4. EXPERIMENTAL RESULTS

The initial investigation into the plasma plume using the LTP was abandon after it became obvious that excess GEM 10T in the plume was shorting the probe producing

abnormal results. When the LTP was used the voltage difference across two of the electrodes would remain constant at a certain level and the current measurement from the other electrode would show either nothing or several small pikes barely disguisable from signal noise.

The NFP was used for the majority of the plasma plume analysis because of its inability to be shorted by the excess GEM 10T in the exhaust plume. The results of the NFP survey and later in-depth analysis show a large level of inconsistency in the plasma generated by the LPPT. The mass consumption analysis also show an inconsistency in mass bit between experiments.

The results of the NFP survey of different operating energies, shown in Table 2.5 and 2.6, shows that over the spectrum of available energies the LPPT plasma generation is largely inconsistent. The small sample size and rejection of pulses not generating plasma results in an incomplete picture of the actual $J_{i,max}$ produced at the different energies. Another problem not shown in Table 2.5 and 2.6, is the difficulty operating the LPPT at the low energy settings found at low operating voltages where the MEDiC had a tendency not to discharge. A problem that is apparent in Table 2.5 and 2.6 is that at energies above 20 J the LPPT had a tendency to backfire into the propellant tank ejecting the baffle and expel GEM 10T onto the walls of the vacuum facility. Shown in Figure 2.6 is that at an operating energy that had a high level of consistency relative to other energies the $J_i(t)$ still a high level of random fluctuations. Due to the ease of operation and relative consistency the energy levels at 390 V was used for subsequent experiments.

When higher numbers of pulses were used to refine the accuracy of mean values of different parameters the consistency of the LPPT plasma generation remained poor. Shown in Figure 2.7, the $J_{i,max}$ for discharge energy of 15.2 J and valve actuation duration of 640 msec were highly inconsistent. The $J_{i,max}$ ranged from 0 to 700 mA/cm2 and the time of these $J_{i,max}$ from 50 to 350 μsec. These levels of inconsistency were not unique to this energy setting but were common with all the energies examined. Changing energy level simply changed the scale of the parameters measure but not the consistency.

Table 2.5. The NFP survey of typical operating energies mean $\boldsymbol{J_{i,max}}$. Areas in red highlight the energies where the perceived risk of backfire is high.

	200V	250V	300V	350V	390V
Level 1	31.41	56.26	77.52	119.96	118.22
Level 2	54.87	73.36	88.64	137.22	280.59
Level 3	76.88	153.29	369.34	303.94	356.71
Level 4	238.30	268.49	412.91	-	-
Level 5	209.85	262.24	311.37	-	-

Table 2.6. The NFP survey of typical operating energies relative standard deviation of the mean $\boldsymbol{J_{i,max}}$. Areas in red highlight the energies where the perceived risk of backfire is high.

	200V	250V	300V	350V	390V
Level 1	52.2%	56.9%	55.4%	51.1%	37.3%
Level 2	28.9%	30.6%	34.3%	47.6%	53.4%
Level 3	69.6%	59.9%	40.0%	56.5%	45.9%
Level 4	20.8%	53.2%	19.2%	-	-
Level 5	32.6%	56.6%	48.2%	-	-

Throughout the experiments the one consistent factor was the rather large inconsistency of the plasma plume parameter measure and calculated. Shown in Table 2.7, the mean values of the $J_{i,max}$ did show higher values when the LPPT was supplied higher energies. These range from a high of 332.6 mA/cm2 for a discharge energy 22.82 J to a low of 83.7 mA/cm2 for a discharge energy of 7.61 J. The mean $J_{i,max}$ of the different energies and VLAD settings have a relative standard deviation with respect to

the mean between 63.6% and 138.2% indicating a high level of inconsistency in these measurements. Some of the pulses of the LPPT would also produce very little plasma with the highest level being 26% of the pulses at a discharge energy of 7.61 J and a VLAD setting of 480 msec producing a $J_{i,max}$ of less than 10 mA/cm2.

Another inconsistency in the plasma plume generated by the LPPT exist in the time from when current is discharged from the MEDiC into the LPPT to when $J_{i,max}$ occurs, Table 2.8. The lowest mean time to $J_{i,max}$ at 25.2 μsec is found at a discharge energy of 7.61 J and a VLAD setting of 200 msec and the highest mean time at 83.4 μsec at a discharge energy of 22.82 J and a VLAD setting of 1275 msec. The overall trend in the data suggest that as energies are increase so is the time to $\boldsymbol{J_{i,max}}$. The mean time to $J_{i,max}$ also shows a large level of inconsistency with respect to the mean ranging from 69.5% to 175.3%.

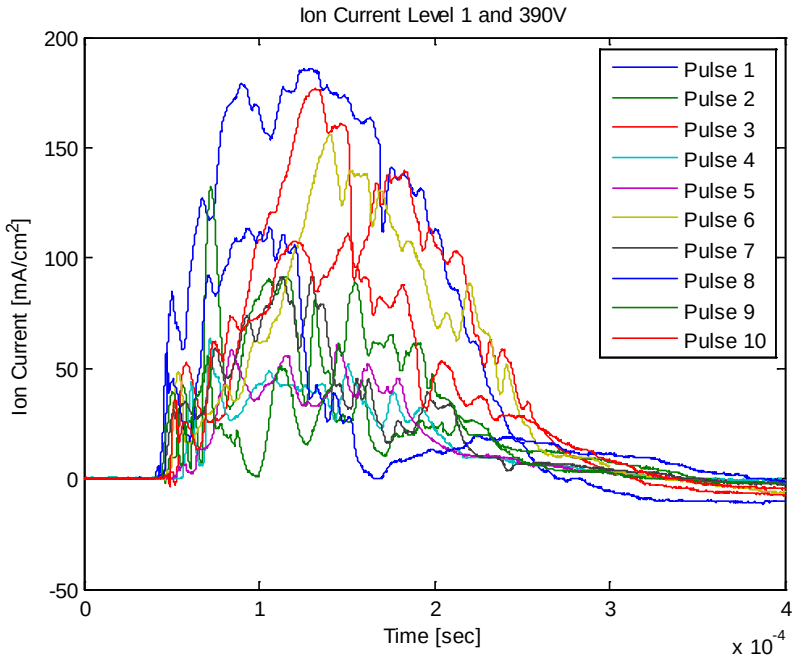

Figure 2.6. Overlay of ten pulse record during the NFP survey at an operating energy of 7.61 J that highlight the random fluctuation of $\boldsymbol{J_i(t)}$ between discharges.

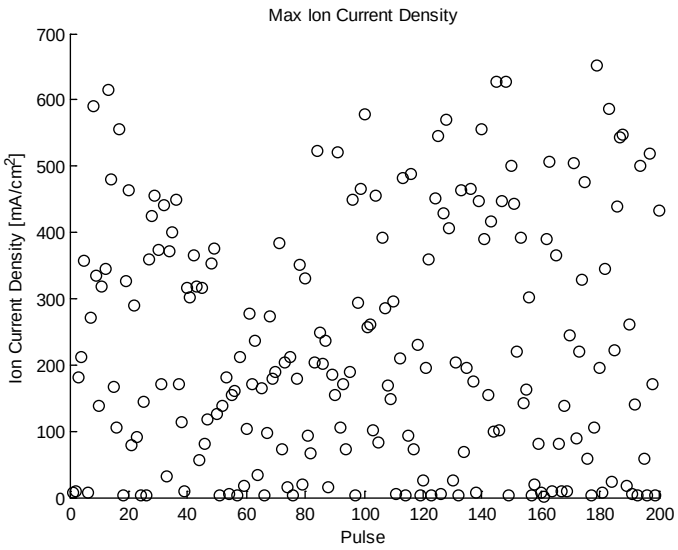

Figure 2.7. Scatter of $\boldsymbol{J_{i,max}}$ for a discharge energy of 15.2 J and valve actuation duration 640 msec.

Table 2.7. $\boldsymbol{J_{i,max}}$ investigation of the series of NFP experiments.

Discharge Energy [J]	Valve Timing [msec]	Number of Pulses	Mean [mA/cm^2]	Standard Deviation [mA/cm^2]	Relative Standard Deviation	Percent of Pulses Below 10 mA/cm^2
7.61	200	200	178.6	113.6	63.6%	-
7.61	360	50	148.4	139.3	93.8%	12.0%
7.61	480	50	106.0	132.9	125.4%	26.0%
7.61	640	50	100.4	128.4	127.9%	22.0%
15.2	640	200	228.7	182.8	79.9%	16.5%
7.61	960	50	125.2	173.0	138.2%	12.0%
7.61	1275	100	83.7	85.7	102.3%	16.0%
15.2	1275	100	256.1	238.8	93.2%	22.0%
22.82	1275	100	332.6	281.2	84.6%	24.0%

Table 2.8. Time of $J_{i,max}$ investigation of the series of NFP experiments.

Discharge Energy [J]	Valve Timing [msec]	Number of Pulses	Mean [μsec]	Standard Deviation [μsec]	Relative Standard Deviation
7.61	200	200	25.2	17.5	69.5%
7.61	360	50	34.2	45.5	133.1%
7.61	480	50	38.3	45.5	118.8%
7.61	640	50	33.2	46.4	140.0%
15.2	640	200	65.0	60.2	92.7%
7.61	960	50	38.2	58.7	153.5%
7.61	1250	100	43.7	76.6	175.3%
15.2	1250	100	58.9	67.2	114.0%
22.82	1250	100	83.4	69.2	82.9%

One use of a NFP is the ability to estimate the u_i by using the known distance of the probe form the thruster and the time difference between the peak current discharge to the LPPT and the $J_{i,max}$ which is also tabulated in Table 2.9. The mean time differences range from 15.9 μsec to 66.0 μsec resulting estimated u_i of 6,300 m/sec to 1,500 m/sec. Then mean time differences follow similar trends as the time to $J_{i,max}$ with the higher energies have higher time differences thus slower u_i. These estimate however show very large inconsistency with relative standard deviations with respect to the mean ranging from 108.9% to 269.1%.

Examining the mass consumption of the LPPT, shown in Table 2.10, highlights the difficulty of determining the mass bit used at different VLAD settings. The LPPT, despite numerous attempts to remedy, leaks some portion of the initial amount of the GEM 10T that filled the propellant tank. The amount that leaks ranged from 0.7g to 1.3g depending on experiment. The percent of m_{used} that leaked out of the LPPT was measured to be from 42 to 45%. The leaking led to an assumed amount leaked of

approximately 1g of GEM 10T used during an experiments where it wasn't directly measured.

Overall the average m_i was measured to be approximately 15 g of propellant. The average m_{used} was found to be approximately 2 g. When looking at m_{liquid} from the LPPT during the mass investigation the amount varied from 0.1 to 0.06 g. The percent of m_{expel} that was m_{liquid} was found to range from a low of 5% to a high of an estimated 45%.

The m_{leak} along with the mass of propellant lost to evaporation, which is assumed negligible, and residual left on the interior of the LPPT make it extremely difficult to accurately determine a mass bit. The m_{bit} that was estimated for several experimental runs ranged from 1.2 to 17.9 mg with mass bits for different experimental runs at the same VLAD setting vary by an order of magnitude. The average m_{bit} was calculated by dividing the sum of m_{expel} by the sum of corresponding n. The average m_{bit} was found to be 9.2 mg.

Table 2.9. The time difference between the peak discharge current and $\boldsymbol{J_{i,max}}$.

Discharge Energy [J]	Valve Timing [msec]	Number of Pulses	Mean [μsec]	Standard Deviation [μsec]	Relative Standard Deviation	Ion Velocity [m/sec]
7.61	200	200	15.9	26.2	164.6%	6293
7.61	320	50	20.2	54.3	269.1%	4955
7.61	480	50	27.4	53.6	195.6%	3651
7.61	640	50	21.6	53.5	248.3%	4639
15.2	640	200	51.4	63.1	122.9%	1947
7.61	960	50	30.2	58.5	193.8%	3316
7.61	1250	100	35.6	76.0	213.4%	2806
15.2	1250	100	40.0	85.4	213.2%	2498
22.82	1250	100	66.0	71.7	108.6%	1514

Table 2.10. GEM 10T mass consumption analysis for a number of different experiments. Areas shaded blue represent the liquid mass investigation experiment.

Valve Timing [msec]	Discharge Energy [J]	m_i [g]	m_f [g]	m_{used} [g]	Number of Pulses	m_{leak} [g]	m_{expel} [g]	Mass Bit [g]	m_{liquid} [g]	m_{gas} [g]
200	Various	17.163	16.010	1.153	-	~1.000	0.438	-	-	-
200	Various	18.750	16.785	1.965	-	~1.000	1.250	-	-	-
-	-	17.041	16.326	0.715	0	0.715	-	-	-	-
200	Various	17.665	-	-	88	-	-	-	-	-
200	Various	17.087	-	-	31	-	-	-	-	-
200	7.61	13.452	12.215	1.237	200	~1.000	0.237	0.0012	-	-
Various	7.61	14.662	13.401	1.261	200	~1.000	0.261	0.0013	-	-
640	15.2	14.739	11.923	2.816	200	~1.000	1.816	0.0091	-	-
1250	Various	16.992	12.063	4.929	220	~1.000	3.929	0.0179	-	-
-	-	17.105	16.205	0.900	0	0.900	-	-	-	-
1250	22.82	17.815	14.855	2.960	80	~1.000	1.960	0.0245	-	-
1250	22.82	14.923	13.709	1.214	100	~1.000	0.214	0.0021	0.061	0.153
1250	15.2	18.295	17.049	1.246	100	~1.000	0.246	0.0025	0.115	0.131
1250	7.61	16.333	13.298	3.035	100	1.275	1.760	0.0176	0.110	1.650
200	7.61	16.648	13.803	2.845	100	1.279	1.566	0.0157	0.071	1.495

2.5. DISCUSSION OF RESULTS

The LPPT demonstrated a lack of consistency generating a plasma plume. The reasons for this large level of inconsistency could be the result of an overabundance of propellant being present in the discharge chamber, a poorly design discharge chamber, and/or GEM 10T being a unsuitable PPT propellant. The experimental results are compared to the HiPEP micro-thruster plume analysis to extract some meaningful insight into the plasma plume generated. Due to the lack of consistency it is difficult to further characterize the plasma plume of the LPPT.

The propellant feed system on the LPPT failed to accurately control the flow of GEM 10T into the discharge chamber. The problem appears to come from a design flaw with the solenoid valve employed on the thruster. When the valve is closed a seal is supposed to be created by the plunger on the solenoid valve and the internal walls of the discharge chamber's housing. This seal is only a plastic on plastic pressure seal that does not utilize any gasket or O-ring. Despite many attempts to adjust the spring on the control valve no setting was found that both allowed for actuation of the valve and a leak proof seal. This design flaw led to an uncontrollable release of propellant that made repeatability between different experimental tests difficult.

The high leak rate of the solenoid valve led to an overabundance of GEM 10T which could make vaporization and ionization during a discharge difficult. The typical PPT mass bit is around 10 to 100 times smaller than the one estimated for the LPPT [20,22,28-33]. The LPPT does operate at similar energy levels to these PPTs. It's speculated that the much higher mass bit to discharge energy would result in poor ionization and performance of the LPPT.

The discharge chamber is different than that of typical PPTs. The use of parallel electrodes is a well understood design for PPTs but in the LPPT these parallel electrodes are only the diameter of metal rods leading into the discharge chambers. Typical PPTs use long electrodes to electromagnetically accelerate the plasma to high velocities [4]. The very short length of the electrodes in the LPPT could be leading to the u_i being an order of magnitude less than typical PPTs [31]. To improve the electromagnetic acceleration of the plasma generated by the LPPT the length of the electrodes should be increased.

A concern with the current design of the LPPT is the placement of the electrodes positioned inwards form the exit of discharge chamber. In the current configuration during a pulse the discharge chamber is typically completely filled with GEM 10T. When the electrical discharge is triggered the bulk of the current should take the path of least resistance which would by directly between the electrodes since the propellant is electrically conductive. The plasma plume generated by the discharge is then electromagnetically accelerated into a large number of neutral particles present in the discharge chamber due to the overabundance of propellant. This process is speculated to be a major contributor to fluctuations in $J_i(t)$ measured by the NFP. Opening the discharge chamber in such a way as to allow the excess GEM 10T to overflow out of the chamber would probably improve the LPPT's plasma generation.

The previously tested the micro-thruster tested by Matthew Glascock produced an ionization fraction of 0.2% or less using the HiPEP fuel which has a similar chemical composition to GEM 10T and discharge method [28]. The HiPEP micro-thruster mass bit was approximately ten times less than the one estimated the LPPT. The $J_{i,max}$ of the two propulsions systems at the same radial location are of the same order of magnitude. Taking these parameters into consideration, the LPPT can be assumed to have an ionization fraction of less than 0.2%. The qualitative result justifies the earlier assumption of the m_{plasma} being negligible.

The LPPT could be improved by replacing the solenoid controlled propellant feed system with a passive capillary system or a more consistent solenoid valve allowing for an accurate control of the propellant. A decrease in the mas bit would likely have a great effect on the plasma plume characteristics. Adding electrode rails similar to a typical PPT to the design of the LPPT would allow for an optimization of the electromagnetic acceleration of the plasma plume. The performance of GEM 10T as a propellant for LPPTs could not be compared with previously tested LPPT propellants from the data collected.

3. MR SAT PROPULSION SYSTEM PERFORMANCE REVIEW

M-SAT propulsion system designs, theoretical calculations, experimental setups, and results are reviewed in this section. The performance analysis previously done shows a large difference with the thrust experimentally measured. When using the original nozzle on a valve thruster (NVT) the error between the theoretically calculated and experimentally measured thrust was over 150%. To improve the thrust predictions of MR SAT's propulsion system the previous performance analysis assumptions are reviewed. The main assumption that is examine is the effects of the solenoid valve are negligible on the flow.

Following this section the development of a procedure for analyzing cold gas thrusters of similar design is discussed. This includes mathematical formulations and examination of multiple case studies. The techniques implemented significantly improve thrust prediction of the NVT. These techniques are then used to predict the performance for the current straight pipe thruster (SPT) and compared to the experimental data. The techniques developed in this section can be used to predict the performance of future M-SAT cold gas propulsion systems. It is important that any future performance analysis is verified through experimentation due to large number of equations that can be used to quantify valve flow.

3.1. MR SAT PROPULSION SYSTEM

Overall MR SAT propulsion system design has remained fairly unchanged over the years consisting of a central propellant tank feeding several thrusters located on the periphery of the satellite [38,39,40]. The current and historical design have consistently used R-134a refrigerant as its propellant. The thrusters are isolated from the propellant tank by a series of solenoid valves and the line pressure is controlled by a regulator. The NVT is the oldest MR SAT thruster design and consisted of attaching a nozzle on the outflow of a valve. The SPT operates by simply using the outflow tube from the solenoid valve as a de-facto nozzle.

3.1.1. Propulsion System Design. MR SAT uses a refrigerant-based cold gas propulsion system. The design consists of a central propellant storage tank, a propellant feed system, and twelve cold gas thrusters [40]. The propellant flows from the storage tank through a series of Lee Company solenoid valves and a Swagelok pressure regulator to a distributor then is routed to individual thruster assemblies. The pressure regulator is rated to produce 24.7 psia at nominal conditions but will vary from 25.7 to 21.7 psia depending on the flow rate through it. The thruster assemblies have varied over the years due to manufacturability issues and changes in components.

3.1.2. Original Thruster Design. The original MR SAT thruster was developed during the Nanosat 4 competition and its subsequent development and testing is documented thoroughly in several theses by M-SAT members [38,39,40]. The design of the NVT, shown in Figure 3.1, involved attaching a nozzle to Lee Company INKX0507800A solenoid valve. The inlet port is attached to a Swagelok fitting. This design was used throughout the Nanosat 4 and 6 competitions.

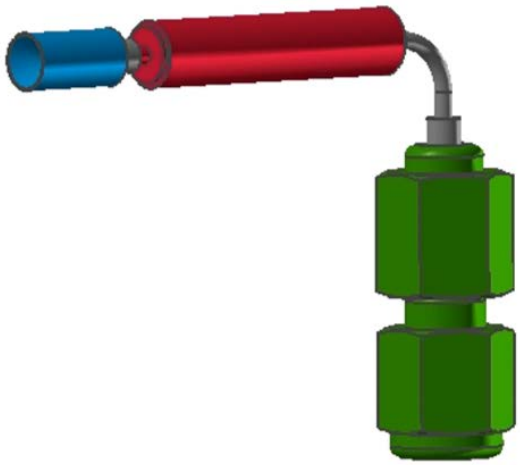

Figure 3.1. The NVT design. The blue section is the nozzle, the red section is the solenoid valve, and the green section is the Swagelok fitting.

3.1.3. Current Thruster Design. The current thruster design consists of simply a valve attached to a mounting bracket. A nozzle was originally considered and was to be manufactured inside of a bolt which would be screwed into the mounting bracket [41]. The manufacturing process proved too difficult to accurately produce the nozzle thus leaving the thruster as just the Lee Company IEPA1221241H solenoid valve, shown in Figure 3.2. When the pipe on the valve is cut and de-burred a small diverging section is created on the end which is treated as the nozzle in the refined performance predictions.

3.2. PREVIOUS PERFORMANCE PREDICTIONS AND EXPERIMENTS

Over the years MR SAT has been in development, numerous attempts have been made to predict and experimentally measure the performance of the different thruster assemblies. The predicted results have typically overestimated the performance of the thruster assembly to a large degree. The historical predicted performance is based on ideal nozzle analysis.

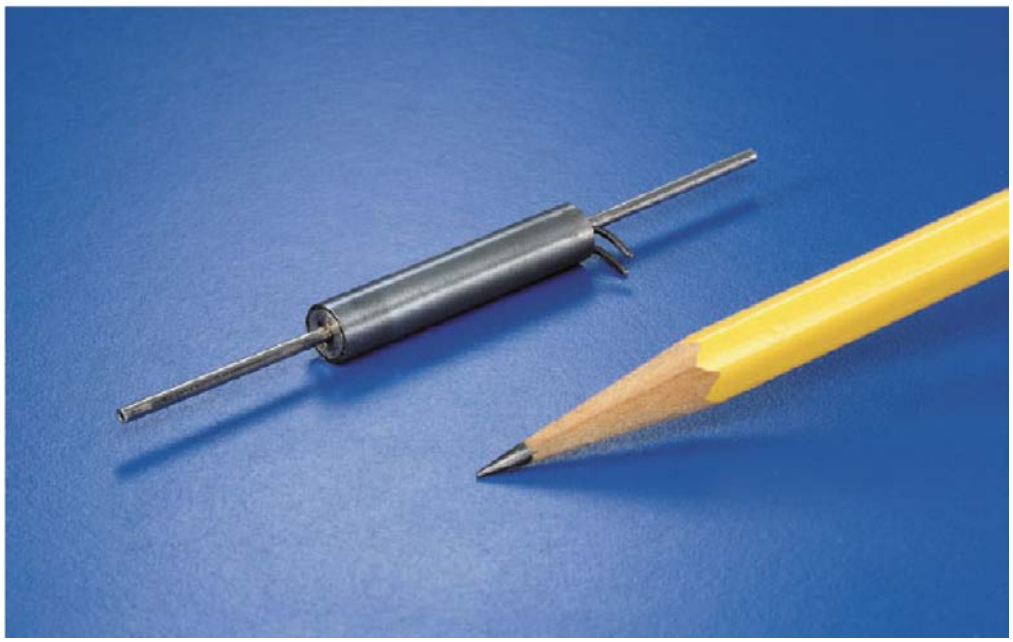

Figure 3.2. Lee Company IEPA1221241H solenoid valve.

3.2.1. Historical Thrust Prediction. The original thrust calculations for the NVT are documented in Carl Seibert's thesis [38]. For the nominal case the flow properties are listed in Table 3.2. The methodology for calculating the performance starts by calculating the speed of sound in the pipe leading to the nozzle (a_0) using

$$a_0 = \sqrt{\gamma R T_0} \tag{3.1}$$

where γ is the ratio of specific heat, R is the gas constant of R-134a, and T_0 is the fluid temperature upstream of the nozzle. The characteristic velocity (c^*) was determined using

$$c^* = \frac{a_0}{\gamma \left(\frac{2}{\gamma+1}\right)^{\gamma+1/2(\gamma-1)}} \tag{3.2}$$

The pressure ratio between the exit and the throat (PR) was then calculated by solving a variation of the area-Mach relationship,

$$\frac{A_e}{A^*} = AR = \sqrt{\frac{\left(\frac{\gamma-1}{2}\right)\left(\frac{2}{\gamma+1}\right)^{(\gamma+1)/(\gamma-1)}}{PR^{2/\gamma}\left[1 - PR^{(\gamma-1)/\gamma}\right]}} \tag{3.3}$$

where AR is the area ratio between the nozzle throat and exit. The mass flow rate through the nozzle ($\dot{m}$) is given by

$$\dot{m} = \frac{A^* P_c}{c^*} \tag{3.4}$$

where P_c is the pressure in the chamber (the pipe leading to the nozzle) found from the PR. The specific impulse (I_{sp}) is determined through

$$I_{sp} = \frac{c^{*}\gamma}{g_0}\sqrt{\left(\frac{\gamma-1}{2}\right)\left(\frac{2}{\gamma+1}\right)^{(\gamma+1)/(\gamma-1)}\left[1-PR^{(\gamma-1)/\gamma}\right]} \tag{3.5}$$

where g_0 is the acceleration due to gravity. The momentum correction factor (λ) for a conical nozzle is found using

$$\lambda = \frac{1}{2}(1+cos\alpha) \tag{3.6}$$

where α is the nozzle half-angle. The thrust (F) produce is then

$$F = \lambda A^{*} P_c \gamma \sqrt{\left(\frac{2}{\gamma-1}\right)\left(\frac{2}{\gamma+1}\right)^{(\gamma+1)/(\gamma-1)}[1-PR^{(\gamma-1)/\gamma}]} + P_e A_e \tag{3.7}$$

To make the performance prediction more accurate correction factors were selected based on estimates provided by textbooks on rocket nozzle performance predictions. The correction factors for F (ζ_F), I_{sp} (ζ_v), and $\dot{m}$ (ζ_d) of 0.972, 1.08, and 0.9 respectively were chosen resulting in estimation of the actual parameters by

$$F_a = \zeta_F F \tag{3.8}$$

$$I_{sp_a} = \zeta_v I_{sp} \tag{3.9}$$

$$\dot{m}_a = \zeta_d \dot{m} \tag{3.10}$$

where the subscript a indicated the actual performance. To determine a conservative estimate of the performance an assumed pressure drop of 10 psi below the regulated pressure and a reduced propellant temperature of was used. The results of these performance prediction routines are shown in Table 3.1 based on the given parameters in Table 3.2.

Table 3.1. Nominal and conservative historical NVT performance.

Parameter	Nominal Estimate	Conservative Estimate
I_{sp_a}	44.09 s	43.71 s
F_a	62.79 mN	37.37 mN
$\dot{m}_a$	0.1481 g/s	0.0889 g/s

Table 3.2. The parameters used in the nominal performance prediction.

Parameter	Nominal Case
P_c	$24.7\ psia = 1.703 * 10^5\ \frac{N}{m^2}$
T_c	$20\ ℃ = 293.2\ K$
g_0	$9.81\ \frac{m}{sec^2}$
γ	1.127
R	$81.49\ \frac{J}{kg * K}$
α	30°
d^*	$0.5\ mm = 0.0005\ m$
A^*	$1.964 * 10^{-7}\ m^2$
d_e	$5\ mm = 0.005\ m$
A_e	$1.964 * 10^{-5}\ m^2$

3.2.2. NVT Performance Parametric Study. The NVT performance was thoroughly tested by Ryan Pahl at several propellant temperature and line pressures [40]. The experiment was conducted in a bell jar vacuum facility in the AP Lab. A schematic of the experimental setup is shown in Figure 3.3. The results of the parametric study were compared to the predicted performance.

3.2.2.1 Experimental methodology. The original experimental setup of the thrust testing of the NVT consisted of measuring the force produced by the thruster using a digital scale inside of a vacuum chamber [40]. To measure and regulate temperature the R-134a tank was placed in a water bath with the temperature recorded by a thermocouple. A hot plate and ice cubes were used to adjust temperature. The line pressure was controlled by an adjustable pressure regulator. Two pressure transducers measured the pressure. One pressure transducer was placed upstream of the regulator to measure the pressure in the tank and another just before the NVT to determine the pressure entering the thruster.

The experiments was conducted from 0-40 ˚C in 10 ˚C increments and 10-100 psia in 10 psia increments providing a parametric study of the performance of the NVT

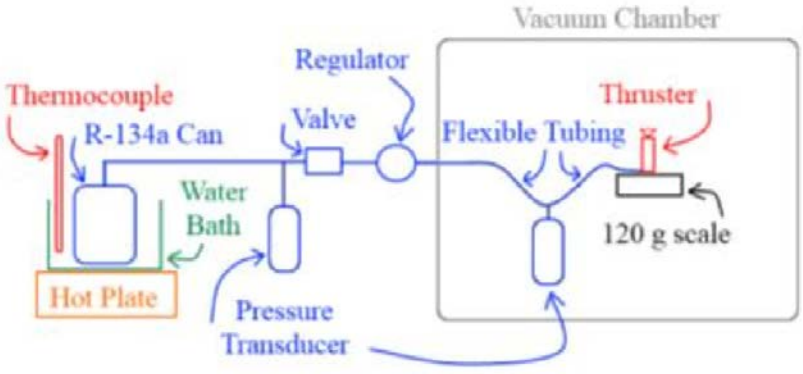

Figure 3.3. Schematic of the NVT parametric study [40].

[40]. The temperature of the propellant was kept constant while the pressure was varied. The thruster was fired for several seconds until the thrust reading reached equilibrium. Each of the pressure and temperature combinations was tested at least five times to ensure an accurate thrust reading.

3.2.2.2 Experimental results. The results of the parametric study, shown in Figure 3.4, show a linear increase in thrust with increasing line pressure and no measureable effect from temperature on thrust readings [40]. The estimated nominal performance of the NVT is shown in Table 3.3. At temperatures of 30 ˚C or higher the thruster experiences an unknown fault leading to a decrease in performance. This phenomenon was witnessed in two identical thruster assemblies with no explanation of the cause.

Table 3.3. The measured nominal operating point of the NVT and error of estimated performance.

Parameter	Measured	Nominal Estimated Error	Conservative Estimated Error
I_{sp} (sec)	20.92*	111%	109%
F (mN)	24.13	160%	55%

* No explanation is given for the method of calculation of this value

3.2.2.3 Discussion of results. The measured performance, Table 3.3, is significantly less than the estimated performance. The measured specific impulse value is highly questionable. The experimental setup did not have the ability to measure flow rate and there was no explanation of how this value was obtained. Shown in Figure 3.4, the second test at 30 ˚C appears to show anomalous data and it is unclear what the cause was. The data was extracted from the original scatter plots and used for comparison with the improved performance predictions.

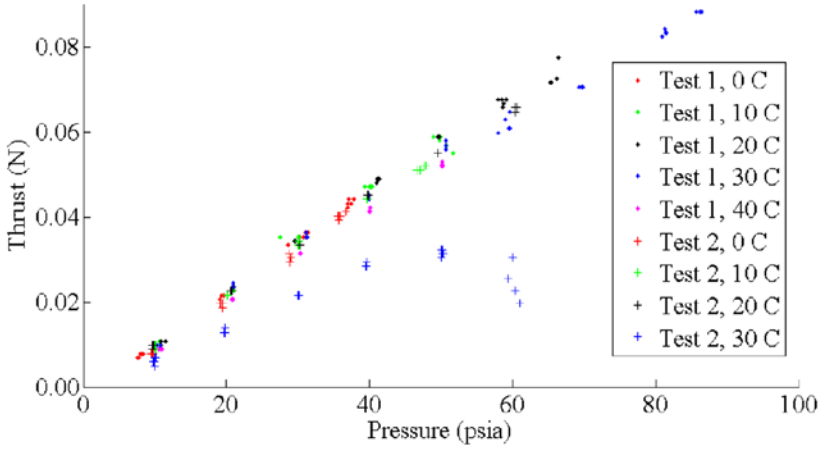

Figure 3.4. Results of the NVT parametric study [40].

3.2.3. SPT Thrust Testing. The SPT was tested using a pendulum thrust stand in the large vacuum facility in the AP Lab. In this section the mathematical basis for a pendulum thrust stand is explained along with a discussion of the experimental methodology and results. The pendulum thrust stand was used to quantify the performance of the SPT.

3.2.3.1 Pendulum thrust stand mathematical basis. A pendulum thrust stand is a simple but highly accurate tool for measuring the thrust produced by micro-thrusters [42,43]. The three main kinds of pendulum thrust stands are inverted, hanging, and torsional [42]. All three types of pendulum thrust stand can be describe by the equation of motion

$$I\ddot{\theta} + c\dot{\theta} + k\theta = F(t)L \tag{3.11}$$

where θ is the angular position, I is the moment of inertia, c is the damping constant, k is the effective spring constant, and $F(t)$ is the applied force acting at a distance L. This equation can be rewritten as

$$\ddot{\theta} + 2\zeta\omega_n\dot{\theta} + \omega_n^2\theta = \frac{F(t)L}{I} \tag{3.12}$$

where ζ is the damping coefficient

$$\zeta = \frac{c}{2}\sqrt{\frac{1}{IK}} \tag{3.13}$$

and ω_n is the natural frequency of the undamped system

$$\omega_n = \sqrt{\frac{k}{I}} \tag{3.14}$$

which for a simple hanging pendulum is

$$\omega_n = \sqrt{\frac{L}{g_0}} \tag{3.15}$$

In a hanging pendulum thrust stand the effect of gravity is a restoring force on the system. The torque associated with the gravitational force is

$$\tau_g = mg_0L_{cm}sin\theta \tag{3.16}$$

where m is the mass of the pendulum and L_{cm} is the length from the pivot point to the center of mass. For small θ equation 3.18 can be approximated as

$$\tau_g \cong mg_0L_{cm}\theta \tag{3.17}$$

With the approximation of equation 3.17 the gravitational torque can be incorporated into the spring torque by

$$k = k_s + mgL_{cm} \tag{3.18}$$

where k_s is the actual spring torque.

There are two ways to utilize a pendulum thrust stand to determine the thrust. If the thrust produced by a micro-thruster is a steady-state event the thrust can be view as a step input, where

$$F(t) = \begin{cases} 0 \; for \; t < 0 \\ F \; for \; t \geq 0 \end{cases} \tag{3.19}$$

The steady state deflection of the pendulum thrust stand (θ_{ss}) is

$$\theta_{ss} = \frac{FL_t}{I\omega_n^2} = \frac{FL_t}{k} \tag{3.20}$$

where L_t is the distance from the pivot point to the thruster. For an undamped hanging pendulum thrust stand the θ_{ss} is

$$\theta_{ss} = sin^{-1}\left(\frac{x_{ss}}{L_{cm}}\right) \tag{3.21}$$

where x_{ss} is the steady displacement of the thrust stand. If the thrust produced by a micro-thruster happen over a very small time frame it can be treated as an impulse input,

$$F(t) = I_{bit}\delta(t) \tag{3.22}$$

where I_{bit} is the impulse bit produce by the micro-thruster. The initial angular velocity produced is

$$\dot{\theta}(0) = \frac{I_{bit}L_t}{I} \tag{3.23}$$

For an undamped system the maximum amplitude (θ_m) is

$$\theta_m = \frac{I_{bit} L_t}{I \omega_n} \tag{3.24}$$

For an undamped pendulum thrust stand the period of oscillation (t_p) is

$$t_p = 2\pi \sqrt{\frac{L_{cm}}{g_0}} \tag{3.25}$$

The thrust produced by a micro-thruster on an undamped hanging pendulum thrust stand is given by

$$F = \frac{m g_0 L_{cm}}{L_t} sin^{-1}\left(\frac{x_{ss}}{L_{cm}}\right) \tag{3.26}$$

3.2.3.2 Experimental methodology. The SPT was tested on an undamped hanging pendulum thrust stand developed by M-SAT [44]. The thruster board contains an R-134a tank, a pressure regulator, a pressure transducer, a thermocouple on the propellant line, an Arduino, and the SPT. The thruster board is suspended from the stand by fishing line and its displacement is measured with a laser range finder. This method has been shown to measure accurate values of the small amount of thrust produced by the SPT [43].

The thruster board's mass was measured before and after each test using a digital scale [44]. Following the initial mass measurement the length of the fishing line from the pivot point is measured with a tape measure. The vacuum facility was pumped down to the operating pressure and the amplitude of the oscillation of the thrust board is allowed to approach zero. The solenoid valve is then opened and the thruster fires for 15 seconds. The pressure, temperature, and displacement are recorded over the experimental run. The experiment was repeated ten times to insure an accurate result.

3.2.3.3 Experimental results. The raw data from the SPT pendulum thrust stand were available allowing an in-depth analysis of the results to be conducted. The displacement measured with respect to time of the ten experiments is shown in Appendix C. The physical parameters of the test are shown in Table 3.4 along with their mean value and standard deviation (σ). The parameters calculated by the raw physical parameters and analysis of the displacement are shown in Table 3.5.

The raw displacement was analyzed over the test duration and ten seconds before and after the test fire. The x_{ss} was determined by averaging the maximum and minimum amplitude of displacement and then averaging these values. The t_p was determined by averaging the peak-to-peak time of several oscillations. The length (L_{cm}) was then determined by using equation 3.27. F is then found using equation 3.28.

The value of $\dot{m}$ can be found using a couple of different methodologies. The first method is to use the average change in mass (Δm) and duration of a test fire (t_f) that results in an $\dot{m}$ of 0.06 g/s. The second method is to analyze Δm over the entire test regime and the total duration t_f that results in an $\dot{m}$ of 0.03 g/s. This difference in $\dot{m}$ results in an average I_{sp} ranging from 25.1 to 50.3 s.

Table 3.4. Physical parameters recorded during the SPT thrust test.

Test	T (k)	P (psia)	L_t (mm)	m_i (g)	m_f (g)	Δm (g)	t_f (s)
1	298.51	25.9	885.8	1659.80	1659.60	0.20	15
2	297.35	24.8	892.0	1661.10	1660.30	0.80	15
3	296.46	25.2	888.0	1660.30	1659.70	0.60	15
4	297.88	25.9	892.0	1660.85	1659.70	1.15	15
5	291.63	24.8	889.0	1659.65	1658.90	0.75	15
6	297.17	25.5	891.0	1658.70	1657.85	0.85	15
7	298.24	-	892.2	1658.65	1657.60	1.05	15
8	297.26	-	895.0	1658.05	1656.95	1.10	15
9	298.33	-	889.0	1657.25	1656.10	1.15	15
10	300.85	-	895.4	1656.30	1655.30	1.00	15
Mean	297.368	25.35	890.9	1659.1	1658.2	0.9	15.0
σ	2.22	0.46	2.86	1.48	1.62	0.28	0

Table 3.5. Parameters calculated for the SPT thrust test.

Test	x_{ss} (mm)	t_p (s)	L_{cm} (mm)	θ_{ss} (deg)	F (mN)
1	0.793	1.90	896.7	0.0507	14.6
2	0.774	1.89	887.3	0.0500	14.1
3	0.782	1.89	884.2	0.0507	14.3
4	0.850	1.91	904.3	0.0538	15.5
5	0.894	1.90	896.7	0.0571	16.4
6	0.834	1.89	887.3	0.0538	15.2
7	0.833	1.90	893.6	0.0534	15.2
8	0.804	1.89	889.7	0.0518	14.6
9	0.799	1.88	881.1	0.0520	14.6
10	0.768	1.90	896.7	0.0491	13.9
Mean	0.813	1.89	891.8	0.0522	14.8
σ	0.037	0.01	6.7	0.0023	0.693

3.2.3.4 Discussion of results. The raw displacement data shown in Appendix C highlights a problem present in the experimental setup. The accuracy of the mass measurement makes it difficult to precisely quantify $\dot{m}$.

The raw displacement data shown in Appendix C appears to indicate a timing error in the LABVIEW program which resulted in data being distorted. This distortion results in the data record jumping back in forth from the pre-firing to post-firing. This distortion causes some level of uncertainty in x_{ss} and t_p but through averaging a reasonably accurate value is determined.

The accuracy of the mass measurements shown in Table 3.4 is questionable. The value of Δm has a high relative standard deviation of 31% that is likely the result of attempting to quantify a very small Δm with respect to the overall mass of the system using a digital scale. The tendency of m_f of the previous test being less than m_i of the following test highlights this problem. This lack of precision makes it difficult to accurately quantify $\dot{m}$.

The small angle assumption in equation 3.19 appears valid due to the magnitude of θ_{ss}. The simple harmonic analysis indicates that the L_{cm} of the hanging pendulum is slightly greater than L_t. The raw data from the hanging pendulum thrust stand experiment indicates that P and T is approximately 25.4 psia and 297.4 K respectably. The F is approximately 14.8 mN with only a 4.7% relative standard deviation of the mean.

3.3. IMPROVED THRUSTER PERFORMANCE PREDICTIONS

The majority of the error associated with the performance analysis previously done by M-SAT can be attributed to the assumption that the Lee Company valve directly upstream of the nozzle has a negligible effect on the flow properties. This assumption allowed for the flow to be treated as a simple ideal nozzle analysis with the propellant feed line from the propellant tank after the regulator being treated as an infinitely large reservoir expelling through an attached nozzle. This over simplification skews the performance parameters calculated against the real case measured experimentally.

To improve future thrust predictions of an in-depth analysis on the effects the valves have on the flow are needed. The effects of a valve on the flow are assessed along with an approach to calculate these effects. Coupling the valve flow equations with the rocket nozzle equation allow for a more accurate method to estimate the performance of the MR SAT propulsion system. When using these equations special care must be taken with units because the valve flow equations are typically in English units whereas the rocket equations are typically in SI units. To improve the theoretical thrust calculations the assumption that the flow was choking in the Lee Company's valve is investigated.

The mathematical basis of the improved thruster performance predictions operates on the assumption that the mass flow rate through the propulsion system is dependent on the solenoid valve. To analyze the nominal operating conditions of the experimentally tested thrusters the flow is assumed choked in the solenoid valve and in the nozzle throat. This assumption is referred to as a multiple point choked flow (MPCF) throughout the flowing sections. The nozzle performance is based on the principles of ideal nozzle analysis.

3.3.1. Ideal Rocket Nozzle Analysis. Ideal rocket nozzle analysis is typically the first step to quantifying the expected performance of a conventional (i.e. cold gas, mono-, and bi-propellant) spacecraft propulsion system [4]. This type of analysis generally gives an error between 1 and 6% due to assumptions that performance losses are negligible. This analysis assumes isentropic expansion in the nozzle which maximizes the conversion of thermal to kinetic energy [45]. The flow is analyzed as quasi- one-dimensional ignoring any three-dimensional effects. For ideal rocket nozzle analysis the flowing assumptions must be made:

- The working substance is homogenous
- All the species of the working fluid are gaseous
- The working substance obeys the perfect gas law
- The flow is adiabatic (no heat transfer with the walls)
- All boundary layer effects and friction are negligible
- The propellant flow is steady and constant
- All exhaust gases leave the nozzle with an axially directed velocity
- Any section normal to the nozzle axis has uniform properties (i.e. velocity, pressure, temperature, etc.)
- Chemical equilibrium is established inside the rocket chamber and does not change

In ideal rocket nozzle analysis the $\dot{m}$ through a choked nozzle is defined as

$$\dot{m} = \frac{A^* P_t}{\sqrt{T_t}} \sqrt{\frac{R}{\gamma}} \left(\frac{\gamma + 1}{2}\right)^{(\gamma+1)/2(\gamma-1)} \tag{3.27}$$

Equation 3.27 can be rearranged to solve for the pressure in the chamber (P_t) by

$$P_t = \frac{\dot{m}\sqrt{T_t}}{A^*} \sqrt{\frac{R}{\gamma}} \left(\frac{\gamma + 1}{2}\right)^{(\gamma+1)/2(\gamma-1)} \tag{3.28}$$

and for A^* by

$$A^* = \frac{\dot{m}\sqrt{T_t}}{P_c}\sqrt{\frac{R}{\gamma}}\left(\frac{\gamma+1}{2}\right)^{(\gamma+1)/2(\gamma-1)} \tag{3.29}$$

The area-Mach relation is given by

$$\frac{A}{A^*} = AR = \frac{1}{M}\left\{\frac{2}{\gamma+1}\left[1+\frac{\gamma-1}{2}M^2\right]\right\}^{\frac{1}{2}(\gamma+1)/(\gamma-1)} \tag{3.30}$$

Equation 3.30 is used to determine M at the exit of the nozzle. An isentropic relationship is used to determine the pressure at the exit of the nozzle (P_e) as

$$P_e = \frac{P_t}{\left[1+\frac{\gamma-1}{2}M^2\right]^{\gamma/(\gamma-1)}} \tag{3.31}$$

Another isentropic relationship is used to determine the temperature at the exit (T_e) as

$$T_e = \frac{T_t}{\left[1+\frac{\gamma-1}{2}M^2\right]} \tag{3.32}$$

The exit velocity of the exhaust gas (u_e) is given by

$$u_e = M\sqrt{\gamma R T_e} \tag{3.33}$$

Thrust (F) produced by the nozzle is then found by

$$F = \lambda \dot{m} v_e + P_e A_e \tag{3.34}$$

The I_{sp} is calculated using

$$Isp = \frac{F}{\dot{m} g_0} \tag{3.35}$$

3.3.2. Valve Flow Equations. Mass flow rate through a valve is a difficult value to quantify. Most textbooks that describe pipe flow only mention that valves will have an effect on the flow but do not detail how to quantify it [46]. Instead, textbooks typically recommend consulting with the manufacturer of the valve for the empirically found equations. Great care must be taken with the units because pipe flow equations are predominately expressed using English units.

These valve flow equations are broken down into two categories. The first is normal flow, where the pressure differential across the valve is such that the flow will not choke in the valve. The second is choked flow, where the pressure differential across the valve is such that the flow will go sonic at the orifice. At choked flow conditions the maximum flow rate through the valve with respect to the upstream pressure is achieved. Interestingly every manufacturer gives a different set of equations with several being detailed in this section.

The Generalized Fluid System Simulation Program, GFSSP, is a program developed by NASA to analyze flow in complex systems. The GFSSP manual goes into great detail on the mathematical formulation in the program [47]. For compressible flow through a restriction the GFSSP uses:

$$P_{cr} = \left(\frac{2}{\gamma + 1}\right)^{\gamma/(\gamma-1)} \tag{3.36}$$

Choked Flow ($\frac{P_j}{P_i} \leq P_{cr}$)

$$\dot{m}_{ij} = C_{v,ij} A \sqrt{P_i \rho_i g_c \frac{2\gamma}{\gamma - 1} (P_{cr})^{2/\gamma} [1 - (P_{cr})^{(\gamma-1)/\gamma}]} \tag{3.37}$$

Normal Flow ($\frac{P_j}{P_i} > P_{cr}$)

$$\dot{m}_{ij} = C_{v,ij} A \sqrt{P_i \rho_i g_c \frac{2\gamma}{\gamma - 1} \left(\frac{P_j}{P_i}\right)^{2/\gamma} \left[1 - \left(\frac{P_j}{P_i}\right)^{(\gamma-1)/\gamma}\right]} \tag{3.38}$$

where $\dot{m}_{ij}$ is in lb/sec, A is in in^2, P is in lb$_f$/in^2, ρ is in lb/ft^3, and g_c is 32.174 lb-ft/lb$_f$-sec^2. The Lee Company's valve flow equations are [48]:

Choked Flow ($\frac{P_1}{P_2} \geq 1.9$)

$$Q = \frac{K f_t P_1}{L} \tag{3.39}$$

Normal Flow ($\frac{P_1}{P_2} < 1.9$)

$$Q = \frac{2K f_t \sqrt{\Delta P P_2}}{L} \tag{3.40}$$

where f_t is a temperature correction factor given by

$$f_t = \sqrt{\frac{530}{T + 460}} \tag{3.41}$$

where Q is in kg/min, P is in psia, ΔP is the pressure differential across the valve, T is in ˚F, K is a unit constant 0.629, and L is given by the manufacturer. The K valve is provided by Lee Company from a list of fluids (R-134a is not available so Freon-12 is used instead). Swagelok's valve flow equations are [49]:

Choked Flow ($\frac{P_2}{P_1} \leq 0.5$)

$$Q = 0.471 N C_v P_1 \sqrt{\frac{1}{G_g T_1}} \tag{3.44}$$

Normal Flow ($\frac{P_2}{P_1} > 0.5$)

$$Q = NC_v P_1 \left(1 - \frac{2\Delta P}{3P_1}\right) \sqrt{\frac{\Delta P}{P_1 G_g T_1}} \tag{3.45}$$

where Q is in SCFM, N is a constant equal to 22.67, P is in psia, G_g is the specific gravity, and T is in ˚R. The Parker Instrumentation's valve flow equations are [50]:

Choked Flow ($\frac{P_1}{P_2} \geq 1.89$)

$$Q = 13.63 C_v P_1 \sqrt{\frac{1}{T_1 G_g}} \tag{3.46}$$

Normal Flow ($\frac{P_1}{P_2} < 1.89$)

$$Q = 16.05 C_v \sqrt{\frac{P_1^2 - P_2^2}{T_1 G_g}} \tag{3.47}$$

where Q is in SCFM, P is in psia, and T is in ˚R.

3.3.3. Lee Company's Valves. M-SAT has used two different solenoid valves for MR SAT's propulsion system over the years. The NVT uses INKX0507800A and the SPT uses IEPA1221241H solenoid valves. The Lee company rates their valves using the Lohms (L) system which can be used to define several properties as the following [51]:

$$L = \frac{0.67}{C_D d^2} \tag{3.48}$$

$$L = \frac{20}{C_v} \tag{3.49}$$

$$L = \frac{0.76}{d^2} \tag{3.50}$$

where C_D is the coefficient of discharge, C_v is the flow coefficient, and d is the orifice diameter in inches. The Lee Valve Company estimate that the actual values can vary by +/- 15%. Assuming that the values provided by these equations 3.48-50 are accurate Table 3.6 shows the valve flow parameters of the two different valves that MSAT has used.

Table 3.6. Lee Company's valve parameters.

Part Number	INKX0507800A	IEPA1221241H
L	4750	4100
d (in)	0.01269	0.01365
d (mm)	0.32127	0.34589
C_D	0.88159	0.88159
C_v	0.00421	0.00488

3.3.4. Coupling Valve and Nozzle Equations. To predict the performance of a cold gas thruster the valve and nozzle equations need to be coupled together. If the pressure ratio over the valve results in choked flow the valve flow equations are used to determine the $\dot{m}$ through the thruster. If the pressure ratio over the valve results in normal flow the $\dot{m}$ is determined by coupling a valve flow equation for normal flow and equation 3.29.

If the GFSSP or Lee Company valve flow equations are used only the units of $\dot{m}$ must be converted. If the Swagelok or Parker Instrumentation valve flow equations are used the $\dot{m}$ is determined by

$$\dot{m} = Q\rho_s \tag{3.51}$$

where Q needs to converted to SCMS and ρ_s is the standard density of the fluid in kg/m^3. The ρ_s is given by the ideal gas law

$$\rho_s = \frac{P_s}{RT_s} \tag{3.52}$$

where P_s is the standard pressure equal to 101,325 N/m^2 and T_s is the standard temperature equal to 293.15 K.

3.4. RESULTS OF MPCF ANALYSIS

The results of the MPCF analysis at the NVT nominal point of 24.7 psia and 20 ˚C for the different valve flow equations are shown in Table 3.7. The results of the MPCF analysis at the SPT nominal operating point of 25.4 psia and 24.2 ˚C for the different valve flow equations are shown in Table 3.8. A comparison between the MPCF using the different valve flow equation and the NVT parametric study data is shown in Figures 3.5-8. The accuracy of the MPCF analysis using the different valve flow equation with NVT parametric data's least-mean-square is shown in Table 3.9.

Table 3.7. Performance predictions of the NVT at nominal condition.

Valve Flow Equation	F (mN)	Error	$\dot{m}$ (g/sec)	I_{sp} (sec)
Parker Instrumentation	28.5	4.5%	0.0604	48.0
Swagelok	22.3	18.1%	0.0473	48.0
Lee Company	22.7	16.7%	0.0482	48.0
NASA's GFSSP	8.8	67.5%	0.0188	48.0

Table 3.8. Performance predictions of the SPT at nominal condition.

Valve Flow Equation	F (mN)	Error	$\dot{m}$ (g/sec)	I_{sp} (sec)
Parker Instrumentation	21.6	45.7%	0.0713	30.8
Swagelok	16.9	14.2%	0.0559	30.8
Lee Company	17.2	16.2%	0.0568	30.8
NASA's GFSSP	6.7	54.7%	0.0222	30.8

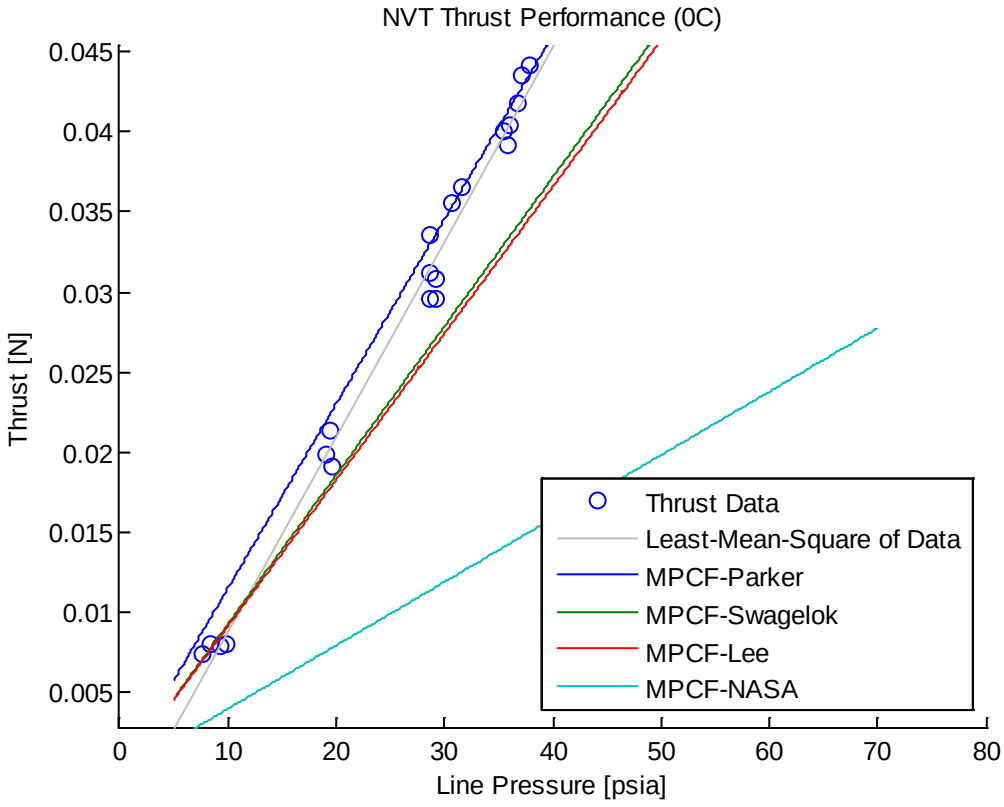

Figure 3.5. Comparison of the MPCF using different valve equations against the NPT parametric data at 0 ˚C.

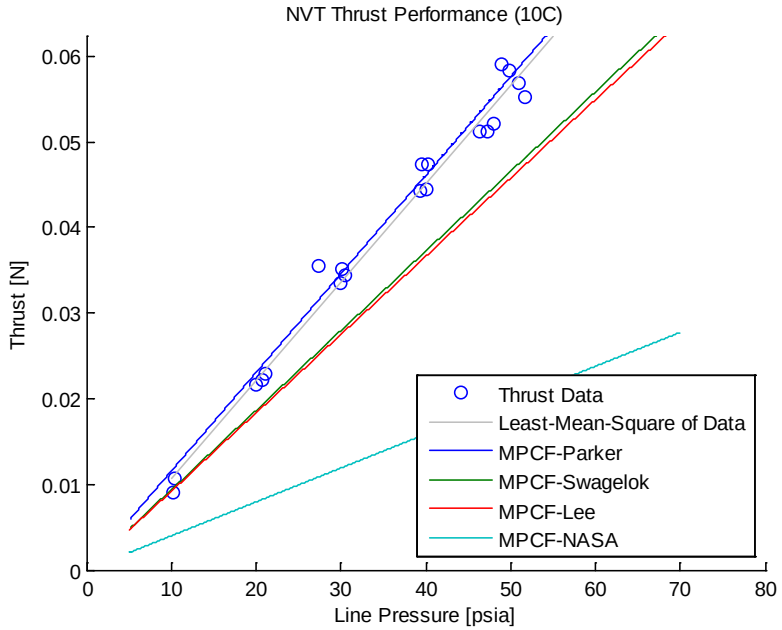

Figure 3.6. Comparison of the MPCF using different valve equations against the NPT parametric data at 10 ˚C.

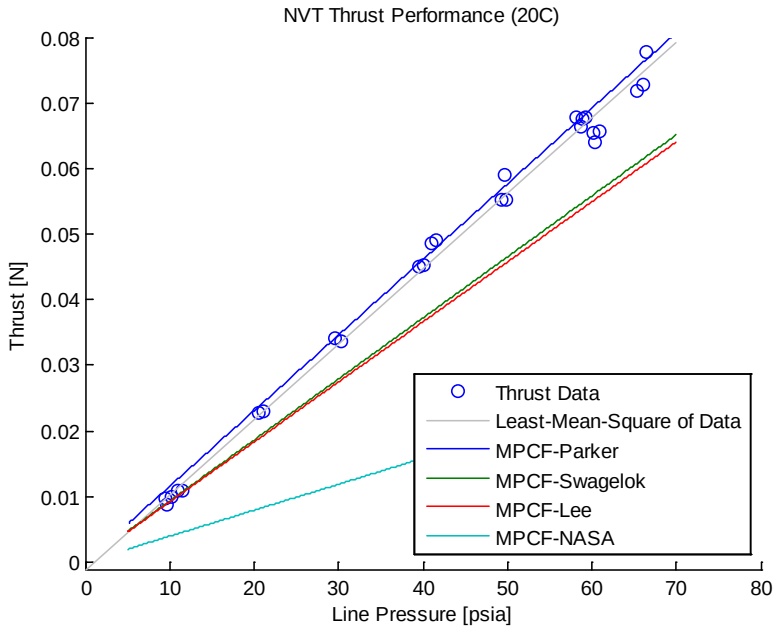

Figure 3.7. Comparison of the MPCF using different valve equations against the NPT parametric data at 20 ˚C.

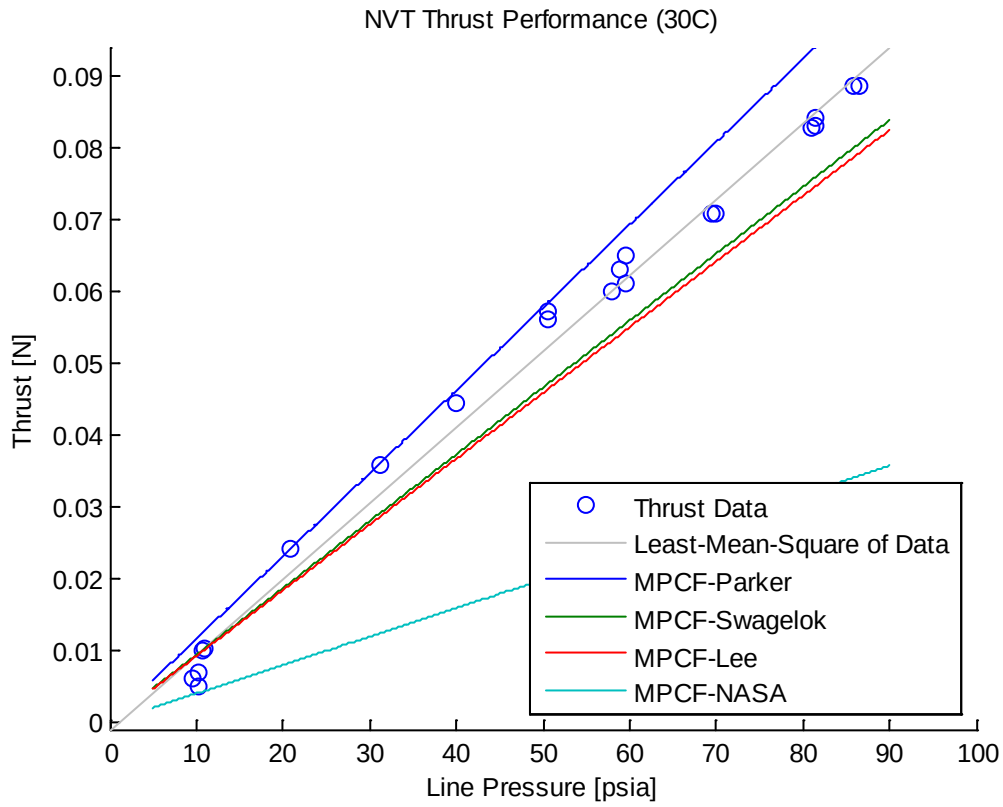

Figure 3.8. Comparison of the MPCF using different valve equations against the NPT parametric data at 30 ˚C.

Table 3.9. Error of the MPCF analysis using different valve flow equations to the least-mean-square of the parametric study data.

T	MPCF Error			
(˚C)	Parker	Swagelok	Lee	NASA
0	-1.10%	-21.46%	-20.15%	-65.99%
10	1.35%	-19.54%	-18.20%	-65.16
20	2.18%	-18.88%	-17.52%	-64.87%
30	10.97%	-11.90%	-10.43%	-61.85%

3.5. DISCUSSION OF MPCF ANALYSIS

Overall the MPCF analysis provides an accuracy of 14% or less when compared to the available experimental data when using the valve flow equation that provides the most accurate result. The decrease in mass flow rate and pressure drop when choking in the valve is considered appears to explain the historical overestimate of performance. The SPT predictions are not as accurate as the NVT and the lack of more experimental data prevents the MPCF to be fine-tuned for this case.

The MPCF analysis had a much higher accuracy compared to the historical MR SAT performance predictions. The Parker Instrumentation valve flow equations provide the highest level of accuracy for the NPT at 4.5% for the nominal operating conditions. When compared with the NVT parametric study thrust data the MPCF using the Parker Instrumentation valve equations ranged in accuracy from -1.1 to 11% with the least-mean-square of the data. The Swagelok valve flow equations provide the highest level of accuracy for thrust of the SPT at its nominal operating condition of 14.2%.

The mass flow rate predicted for the NVT by the different valve equations used by the MPCF are approximately a third of what was historically predicted which may explain why the original performance predictions overestimated the thrust to such a large degree. The predict mass flow rate for the SPT at the nominal operating conditions, shown in Table 3.8, of all the valve flow equation is of the same order of magnitude as the range of experimentally measured value. The mass flow rate predicted by the Swagelok and Lee Company valve flow equations fall between the 0.3-0.6 g/sec range but it is difficult to determine which one offers the highest accuracy.

The SPT predicted thrust is not as accurate as the NVT with the highest accuracy achieved as only 14.2% compared to 4.5% for the nominal cases. The assumption that the exit of the outlet pipe can be treated as a nozzle throat is questionable. The performance parameters of the valve itself could also be slightly (+/- 15%) different than the ones calculated by equations 3.48-50. There is currently no data on how the SPT performs over a range of pressure and temperatures to determine which valve flow equations obtain the most accurate result. An increase in the number of experimental data at different operating points would allow for a fine-tuned MPCF analysis with increased analysis.

4. CONCLUSION

4.1. SUMMARY OF THE LPPT ANALYSIS

LPPTs are promising electric propulsion system concepts that still have several obstacles to overcome before they can become fully operational on future spacecraft. The most obvious obstacle facing LPPT is the accurate control of the very small amounts of liquid propellant used by the system during each pulse. This problem plagued the LPPT resulting in a system that produced plasma with a standard deviation of the mean ion current density ranging from 63.8% to 138.2%. It is difficult to determine whether or not GEM-10T is a good LPPT propellant due to the challenge to control the flow of propellant to discharge chamber. Any future LPPT design should be very careful in its selection of solenoid valve to avoid the high leak rate.

4.2. SUMMARY OF MPCF ANALYSIS

Coupling valve flow equations and ideal nozzle analysis provides for a level of accuracy ranging from 14.2% to 4.5% when predicting the performance of a cold gas thruster compared to the use of the ideal nozzle equations on their own. The MPCF analysis allows for the performance prediction of MR SAT's thrusters over a wide range of pressure and temperature accurately to within 11% for the NVT. It is difficult to determine how accurately the MPCF will predict the performance of the current thruster design over a wide range of operating conditions due to the narrow scope of the thrust testing performed. If the previous thruster, thrust testing data, and analysis is used as a guide, the MPCF should predict the performance of the current design over a range of pressure and temperatures to within 20%. For future analysis of propulsion systems the effects of valves on the flow should be included.

APPENDIX A.

NVT NONIMAL FLOW PERFORMANCE ALGORITHM

```
%%%%%%%%%%%%%%%%%%%%%%%%%%%%%%%%%%%%%%%%%%%%%%%%%%%%%%%%%%%%%%%%%%%%%%%%%%%%
%%%%%%%%%%%%%%%%%    NVT Nominal Flow Performance     %%%%%%%%%%%%%%%%%%%%
%%%%%%%%%%%%%%%%%%%%%%%%%%%%%%%%%%%%%%%%%%%%%%%%%%%%%%%%%%%%%%%%%%%%%%%%%%%%
clc; close all; clear all;
%%%%%%%%%%%%%%%%%%%%%%%%%%%%%%%%%%%%%%%%%%%%%%%%%%%%%%%%%%%%%%%%%%%%%%%%%%%%
%%%%%%%%%%%%%%%%%%%%%%    Conversion Factors    %%%%%%%%%%%%%%%%%%%%%%%%%%
%%%%%%%%%%%%%%%%%%%%%%%%%%%%%%%%%%%%%%%%%%%%%%%%%%%%%%%%%%%%%%%%%%%%%%%%%%%%

%Converts inches to
meters in_to_m =
0.0254;
%Converts meters to
inches m_to_in =
39.3701;
%Converts degrees to
radians deg_to_rad =
0.0174533;
%Converts psi
to Pa psi_to_pa
= 6894.76;
%Converts Pa to psi
pa_to_psi =
0.000145038;
%Converts SCFM to SCMS
SCFM_to_SCMS =
4.7194667e-4;
%Converts kg/m^3 to
lb/ft^3
kg_m3_to_lb_ft_3 =
0.062428;

%%%%%%%%%%%%%%%%%%%%%%%%%%%%%%%%%%%%%%%%%%%%%%%%%%%%%%%%%%%%%%%%%%%%%%%%%%%%
%%%%%%%%%%%%%%%%%%%%%    R-134a Properties     %%%%%%%%%%%%%%%%%%%%%%%%%%
%%%%%%%%%%%%%%%%%%%%%%%%%%%%%%%%%%%%%%%%%%%%%%%%%%%%%%%%%%%%%%%%%%%%%%%%%%%%

%Molecular Weight
MW = 102.0308928; %[kg/kmol]
%Ratio of Specific
Heats gamma =
1.127;
%Universal Gas Constant
R_univ =  8314.51; %[J/(kmol*K)]
%R-134a gas constant
R = R_univ/MW; %[J/(kg*K)]
%R-134a specific
gravity SG = 3.25;
%Standard Pressure
P_s = 101325; %[N/m^2]
%Standard
Temperature T_s
= 293.15; %[K]
%Standard Density of R-
134a rho_s = P_s/(T_s*R);
%[kg/m^3]

%%%%%%%%%%%%%%%%%%%%%%%%%%%%%%%%%%%%%%%%%%%%%%%%%%%%%%%%%%%%%%%%%%%%%%%%%%%%
%%%%%%%%%%%%%%%%%%%%%    Lee Company Valve     %%%%%%%%%%%%%%%%%%%%%%%%%%
%%%%%%%%%%%%%%%%%%%%%%%%%%%%%%%%%%%%%%%%%%%%%%%%%%%%%%%%%%%%%%%%%%%%%%%%%%%%

%Lohm
rating
L =
```

```
4750;
%Diameter of the orifice
d_orfice = sqrt(0.76/L)*in_to_m; %[m]
%Area of the orifice
A_orfice = (pi/4)*d_orfice^2; %[m^2]
%Flow
coefficient
Cv = 20/L;
%Discharge coefficient
Cd = 0.67/(L*(d_orfice*m_to_in)^2);

%%%%%%%%%%%%%%%%%%%%%%%%%%%%%%%%%%%%%%%%%%%%%%%%%%%%%%%%%%%%%%%%%%%%%%%%%%%%
%%%%%%%%%%%%%%%%%%%%%%    Flow Upstream of Valve    %%%%%%%%%%%%%%%%%%%%%%
%%%%%%%%%%%%%%%%%%%%%%%%%%%%%%%%%%%%%%%%%%%%%%%%%%%%%%%%%%%%%%%%%%%%%%%%%%%%

%Total pressure
Pt0 = (24.7)*psi_to_pa; %[N/m^2]
%Total
temperature
Tt0 = 293.15;
%[K]
%Total density
rhot0 = Pt0/(R*Tt0); %[kg/m^3]

%%%%%%%%%%%%%%%%%%%%%%%%%%%%%%%%%%%%%%%%%%%%%%%%%%%%%%%%%%%%%%%%%%%%%%%%%%%%
%%%%%%%%%%%%%%%%%%%%%%    NVT Nozzle Geometry    %%%%%%%%%%%%%%%%%%%%%%%%
%%%%%%%%%%%%%%%%%%%%%%%%%%%%%%%%%%%%%%%%%%%%%%%%%%%%%%%%%%%%%%%%%%%%%%%%%%%%

%Throat diameter
d_star = 0.0005;
%[m]
%Exit
diameter de
= 0.005;
%[m]
%Throat area
A_star = (pi/4)*d_star^2; %[m^2]
%Exit area
Ae = (pi/4)*de^2; %[m^2]
%Area ratio
AR = Ae/A_star;
%Nozzle half-angle
Theta = 30*deg_to_rad; %[rad]

%%%%%%%%%%%%%%%%%%%%%%%%%%%%%%%%%%%%%%%%%%%%%%%%%%%%%%%%%%%%%%%%%%%%%%%%%%%%
%%%%%%%%%%%%%%%%%%%%%%     Mass Flow Rate     %%%%%%%%%%%%%%%%%%%%%%%%%%
%%%%%%%%%%%%%%%%%%%%%%%%%%%%%%%%%%%%%%%%%%%%%%%%%%%%%%%%%%%%%%%%%%%%%%%%%%%%

%Swagelok
%Temperature upstream
T1 = (Tt0 - 273.15)*1.8 + 491.67; %[R]
%Pressure upstream
P1 = Pt0*pa_to_psi; %[psia]
%Unit
constant
N =
22.67;
%Volumetric flow rate
Q1 = 0.471*N*Cv*P1*sqrt(1/(SG*T1)); %[SCFM]
%Mass flow rate
m_dot(1) = Cd*SCFM_to_SCMS*rho_s*Q1; %[kg/sec]

%Lee Company
```

```
%Unit
constant
K =
0.629;
%Temperature correction
factor f = sqrt(530/T1);
%Volumetric flow rate
Q2 = K*f*P1/L; %[kg/min]
%Mass flow rate
m_dot(2) = Cd*Q2/60; %[kg/sec]

%Parker Instrumentation
%Volumetric flow rate
Q3 = 13.63*Cv*P1*sqrt(1/(T1*SG)); %[SCFM]
%Mass flow rate
m_dot(3) = Cd*SCFM_to_SCMS*rho_s*Q3; %[kg/sec]

%NASA GFSSP
%Area Pipe
OD = (1/16);
%[in] wt =
0.014; %[in]
ID = OD - 2*wt; %[in]
A1 = (pi/4)*ID^2; %[in^2]
%Acceleration due to gravity
gc = 32.174; %[ft/sec^2]
%Density
rho1 = rhot0*kg_m3_to_lb_ft_3; %[lb/ft^3]
%Critical pressure
Pcr = (2/(gamma+1))^(gamma/(gamma-1));
%Mass flow rate
m_dot(4) =Cd*0.453592*Cv*A1*sqrt(P1*rho1*gc*(2*gamma/(gamma-1))*...
    Pcr^(2/gamma)*(1-Pcr^((gamma-1)/gamma))); %[kg/sec]

%%%%%%%%%%%%%%%%%%%%%%%%%%%%%%%%%%%%%%%%%%%%%%%%%%%%%%%%%%%%%%%%%%%%%%%%%%%%%%%
%%%%%%%%%%%%%%%%%%     Ideal Nozzle Equations      %%%%%%%%%%%%%%%%%%%%%%%%%%
%%%%%%%%%%%%%%%%%%%%%%%%%%%%%%%%%%%%%%%%%%%%%%%%%%%%%%%%%%%%%%%%%%%%%%%%%%%%%%%

%Chamber Pressure
Pc =
   m_dot/((A_star/sqrt(Tt0))*sqrt(gamma/R)*(((gamma+1)/2)^
   ... (-(gamma+1)/(2*(gamma-1))))); %[N/m^2]
%Area-Mach
Relationship syms
y;
eqn3 = (AR == (1/y)*((2/(gamma + 1))*(1 + ((gamma -
    1)/2)*y^2))^... ((gamma + 1)/(2*(gamma - 1)))); %Mach area
    relation
assume( y > 1 );
%Exit Mach number
Me = real(double(solve(eqn3, y)));
%Exit Temperature
Te = Tt0/(1 + ((gamma - 1)/2)*Me^2); %[K]
%Exit pressure
Pe = Pc/(1 + ((gamma - 1)/2)*Me^2)^(gamma/(gamma - 1)); %[N/m^2]
%Exit velocity
ue = Me*sqrt(gamma*R*Te); %[m/sec]
%Correction factor
lamda = (1/2)*(1+cos(Theta));
%Thrust
F = lamda*m_dot*ue + Pe*Ae; %[N]
%Specific
Impulse for
```

```
i=1:4
    Isp(i) = F(i)/(m_dot(i)*9.81); %[sec]
end
```

APPENDIX B.

SPT NOMINAL FLOW PERFORMANCE ALGORITHM

```
%%%%%%%%%%%%%%%%%%%%%%%%%%%%%%%%%%%%%%%%%%%%%%%%%%%%%%%%%%%%%%%%%%%%%%%%%%%%
%%%%%%%%%%%%%%%%%%   SPT Nominal Flow Performance      %%%%%%%%%%%%%%%%%%%%%%
%%%%%%%%%%%%%%%%%%%%%%%%%%%%%%%%%%%%%%%%%%%%%%%%%%%%%%%%%%%%%%%%%%%%%%%%%%%%
clc; close all; clear all;
%%%%%%%%%%%%%%%%%%%%%%%%%%%%%%%%%%%%%%%%%%%%%%%%%%%%%%%%%%%%%%%%%%%%%%%%%%%%
%%%%%%%%%%%%%%%%%%%%%%%    Conversion Factors    %%%%%%%%%%%%%%%%%%%%%%%%%%
%%%%%%%%%%%%%%%%%%%%%%%%%%%%%%%%%%%%%%%%%%%%%%%%%%%%%%%%%%%%%%%%%%%%%%%%%%%%

%Converts inches to meters
in_to_m = 0.0254;
%Converts meters to inches
m_to_in = 39.3701;
%Converts degrees to radians
deg_to_rad = 0.0174533;
%Converts psi to Pa
psi_to_pa = 6894.76;
%Converts Pa to psi
pa_to_psi = 0.000145038;
%Converts SCFM to SCMS
SCFM_to_SCMS = 4.7194667e-4;
%Converts kg/m^3 to lb/ft^3
kg_m3_to_lb_ft_3 = 0.062428;

%%%%%%%%%%%%%%%%%%%%%%%%%%%%%%%%%%%%%%%%%%%%%%%%%%%%%%%%%%%%%%%%%%%%%%%%%%%%
%%%%%%%%%%%%%%%%%%%%%%    R-134a Properties     %%%%%%%%%%%%%%%%%%%%%%%%%%
%%%%%%%%%%%%%%%%%%%%%%%%%%%%%%%%%%%%%%%%%%%%%%%%%%%%%%%%%%%%%%%%%%%%%%%%%%%%

%Molecular Weight
MW = 102.0308928; %[kg/kmol]
%Ratio of Specific Heats
gamma = 1.127;
%Universal Gas Constant
R_univ = 8314.51; %[J/(kmol*K)]
%R-134a gas constant
R = R_univ/MW; %[J/(kg*K)]
%R-134a specific gravity
SG = 3.25;
%Standard Pressure
P_s = 101325; %[N/m^2]
%Standard Temperature
T_s = 293.15; %[K]
%Standard Density of R-134a
rho_s = P_s/(T_s*R); %[kg/m^3]

%%%%%%%%%%%%%%%%%%%%%%%%%%%%%%%%%%%%%%%%%%%%%%%%%%%%%%%%%%%%%%%%%%%%%%%%%%%%
%%%%%%%%%%%%%%%%%%%%%%    Lee Company Valve     %%%%%%%%%%%%%%%%%%%%%%%%%%
%%%%%%%%%%%%%%%%%%%%%%%%%%%%%%%%%%%%%%%%%%%%%%%%%%%%%%%%%%%%%%%%%%%%%%%%%%%%

%Lohm rating
L = 4100;
%Diameter of the orifice
d_orfice = sqrt(0.76/L)*in_to_m; %[m]
%Area of the orifice
A_orfice = (pi/4)*d_orfice^2; %[m^2]
%Flow coefficient
Cv = 20/L;
%Discharge coefficient
Cd = 0.67/(L*(d_orfice*m_to_in)^2);

%%%%%%%%%%%%%%%%%%%%%%%%%%%%%%%%%%%%%%%%%%%%%%%%%%%%%%%%%%%%%%%%%%%%%%%%%%%%
%%%%%%%%%%%%%%%%%%%%%%     Flow Upstream of Valve   %%%%%%%%%%%%%%%%%%%%%%%
%%%%%%%%%%%%%%%%%%%%%%%%%%%%%%%%%%%%%%%%%%%%%%%%%%%%%%%%%%%%%%%%%%%%%%%%%%%%
```

```
%Total pressure
Pt0 = (25.35)*psi_to_pa; %[N/m^2]
%Total temperature
Tt0 = 297.368; %[K]
%Total density
rhot0 = Pt0/(R*Tt0); %[kg/m^3]

%%%%%%%%%%%%%%%%%%%%%%%%%%%%%%%%%%%%%%%%%%%%%%%%%%%%%%%%%%%%%%%%%%%%%%%%%%%%%%%
%%%%%%%%%%%%%%%%%%%%%%%%%    SPT Nozzle Geometry    %%%%%%%%%%%%%%%%%%%%%%%%%
%%%%%%%%%%%%%%%%%%%%%%%%%%%%%%%%%%%%%%%%%%%%%%%%%%%%%%%%%%%%%%%%%%%%%%%%%%%%%%%

% SPT Nozzle Design
OD = (1/16)*in_to_m; %[m]
wt = 0.014*in_to_m; %[m]
d_star = OD - 2*wt; %[m]
de = d_star; %Exit diameter[m]
A_star = (pi/4)*d_star^2;
%Throat area[m^2]
Ae = (pi/4)*de^2;
%Exit area[m^2]
AR = Ae/A_star; %Area ratio
Theta = 0*deg_to_rad; %Nozzle half-angle[rad

%%%%%%%%%%%%%%%%%%%%%%%%%%%%%%%%%%%%%%%%%%%%%%%%%%%%%%%%%%%%%%%%%%%%%%%%%%%%%%%
%%%%%%%%%%%%%%%%%%%%%%%%     Mass Flow Rate     %%%%%%%%%%%%%%%%%%%%%%%%%%%%
%%%%%%%%%%%%%%%%%%%%%%%%%%%%%%%%%%%%%%%%%%%%%%%%%%%%%%%%%%%%%%%%%%%%%%%%%%%%%%%

%Swagelok
%Temperature upstream
T1 = (Tt0 - 273.15)*1.8 + 491.67; %[R]
%Pressure upstream
P1 = Pt0*pa_to_psi; %[psia]
%Unit constant
N = 22.67;
%Volumetric flow rate
Q1 = 0.471*N*Cv*P1*sqrt(1/(SG*T1)); %[SCFM]
%Mass flow rate
m_dot(1) = Cd*SCFM_to_SCMS*rho_s*Q1; %[kg/sec]

%Lee Company
%Unit constant
K = 0.629;
%Temperature correction factor
f = sqrt(530/T1);
%Volumetric flow rate
Q2 = K*f*P1/L; %[kg/min]
%Mass flow rate
m_dot(2) = Cd*Q2/60; %[kg/sec]

%Parker Instrumentation
%Volumetric flow rate
Q3 = 13.63*Cv*P1*sqrt(1/(T1*SG)); %[SCFM]
%Mass flow rate
m_dot(3) = Cd*SCFM_to_SCMS*rho_s*Q3; %[kg/sec]

%NASA GFSSP
%Area Pipe
OD = (1/16); %[in]
wt = 0.014; %[in]
ID = OD - 2*wt; %[in]
A1 = (pi/4)*ID^2; %[in^2]
```

```
%Acceleration due to gravity
gc = 32.174; %[ft/sec^2]
%Density
rho1 = rhot0*kg_m3_to_lb_ft_3; %[lb/ft^3]

%Critical pressure
Pcr = (2/(gamma+1))^(gamma/(gamma-1));
%Mass flow rate
m_dot(4) = Cd*0.453592*Cv*A1*sqrt(P1*rho1*gc*(2*gamma/(gamma-1))*...
Pcr^(2/gamma)*(1-Pcr^((gamma-1)/gamma))); %[kg/sec]

%%%%%%%%%%%%%%%%%%%%%%%%%%%%%%%%%%%%%%%%%%%%%%%%%%%%%%%%%%%%%%%%%%%%%%%%%%%%%%%
%%%%%%%%%%%%%%%%%%%%      Ideal Nozzle Equations     %%%%%%%%%%%%%%%%%%%%%%%%
%%%%%%%%%%%%%%%%%%%%%%%%%%%%%%%%%%%%%%%%%%%%%%%%%%%%%%%%%%%%%%%%%%%%%%%%%%%%%%%

%Chamber Pressure
Pc = m_dot/((A_star/sqrt(Tt0))*sqrt(gamma/R)*(((gamma+1)/2)^...
    (-(gamma+1)/(2*(gamma-1))))); %[N/m^2]
%Area-Mach Relationship
syms y;
eqn3 = (AR == (1/y)*((2/(gamma + 1))*(1 + ((gamma - 1)/2)*y^2))^...
    ((gamma + 1)/(2*(gamma - 1)))); %Mach area relation
assume( y > 1 );
%Exit Mach number
Me = real(double(solve(eqn3, y)));
%Exit Temperature
Te = Tt0/(1 + ((gamma - 1)/2)*Me^2); %[K]
%Exit pressure
Pe = Pc/(1 + ((gamma - 1)/2)*Me^2)^(gamma/(gamma - 1)); %[N/m^2]
%Exit velocity
ue = Me*sqrt(gamma*R*Te); %[m/sec]
%Correction factor
lamda = (1/2)*(1+cos(Theta));
%Thrust
F = lamda*m_dot*ue + Pe*Ae; %[N]
%Specific Impulse
for i=1:4
    Isp(i) = F(i)/(m_dot(i)*9.81); %[sec]
end
```

APPENDIX C.

NVT PARAMETRIC FLOW THRUST ANALYSIS ALGORITHM

```
%%%%%%%%%%%%%%%%%%%%%%%%%%%%%%%%%%%%%%%%%%%%%%%%%%%%%%%%%%%%%%%%%%%%%%%%%%%%
%%%%%%%%%%%%%%%%%   NPT Parametric Thrust Analysis    %%%%%%%%%%%%%%%%%%%%%
%%%%%%%%%%%%%%%%%%%%%%%%%%%%%%%%%%%%%%%%%%%%%%%%%%%%%%%%%%%%%%%%%%%%%%%%%%%%
clc; close all; clear all;
%%%%%%%%%%%%%%%%%%%%%%%%%%%%%%%%%%%%%%%%%%%%%%%%%%%%%%%%%%%%%%%%%%%%%%%%%%%%
%%%%%%%%%%%%%%%%%%%%%%    Conversion Factors    %%%%%%%%%%%%%%%%%%%%%%%%%%%
%%%%%%%%%%%%%%%%%%%%%%%%%%%%%%%%%%%%%%%%%%%%%%%%%%%%%%%%%%%%%%%%%%%%%%%%%%%%

%Converts inches to meters
in_to_m = 0.0254;
%Converts meters to inches
m_to_in = 39.3701;
%Converts degrees to radians
deg_to_rad = 0.0174533;
%Converts psi to Pa
psi_to_pa = 6894.76;
%Converts Pa to psi
pa_to_psi = 0.000145038;
%Converts SCFM to SCMS
SCFM_to_SCMS = 4.7194667e-4;
%Converts kg/m^3 to lb/ft^3
kg_m3_to_lb_ft_3 = 0.062428;

%%%%%%%%%%%%%%%%%%%%%%%%%%%%%%%%%%%%%%%%%%%%%%%%%%%%%%%%%%%%%%%%%%%%%%%%%%%%
%%%%%%%%%%%%%%%%%%%%%     R-134a Properties    %%%%%%%%%%%%%%%%%%%%%%%%%%%
%%%%%%%%%%%%%%%%%%%%%%%%%%%%%%%%%%%%%%%%%%%%%%%%%%%%%%%%%%%%%%%%%%%%%%%%%%%%

%Molecular Weight
MW = 102.0308928; %[kg/kmol]
%Ratio of Specific Heats
gamma = 1.127;
%Universal Gas Constant
R_univ =    8314.51; %[J/(kmol*K)]
%R-134a gas constant
R = R_univ/MW; %[J/(kg*K)]
%R-134a specific gravity
SG = 3.25;
%Standard Pressure
P_s = 101325; %[N/m^2]
%Standard Temperature
T_s = 293.15; %[K]
%Standard Density of R-134a
rho_s = P_s/(T_s*R); %[kg/m^3]

%%%%%%%%%%%%%%%%%%%%%%%%%%%%%%%%%%%%%%%%%%%%%%%%%%%%%%%%%%%%%%%%%%%%%%%%%%%%
%%%%%%%%%%%%%%%%%%%%%%    Lee Company Valve    %%%%%%%%%%%%%%%%%%%%%%%%%%%
%%%%%%%%%%%%%%%%%%%%%%%%%%%%%%%%%%%%%%%%%%%%%%%%%%%%%%%%%%%%%%%%%%%%%%%%%%%%

%Lohm rating
L = 4750;
%Diameter of the orifice
d_orfice = sqrt(0.76/L)*in_to_m; %[m]
%Area of the orifice
A_orfice = (pi/4)*d_orfice^2; %[m^2]
%Flow coefficient
Cv = 20/L;
%Discharge coefficient
Cd = 0.67/(L*(d_orfice*m_to_in)^2);

%%%%%%%%%%%%%%%%%%%%%%%%%%%%%%%%%%%%%%%%%%%%%%%%%%%%%%%%%%%%%%%%%%%%%%%%%%%%
%%%%%%%%%%%%%%%%%%%%%%    Flow Upstream of Valve    %%%%%%%%%%%%%%%%%%%%%%%%
%%%%%%%%%%%%%%%%%%%%%%%%%%%%%%%%%%%%%%%%%%%%%%%%%%%%%%%%%%%%%%%%%%%%%%%%%%%%
```

```
%Total pressure
Pt0 = linspace(5,70,1000)*psi_to_pa; %[N/m^2]
%Total temperature
Tt0 = 293.15; %[K]
%Total density
rhot0 = Pt0/(R*Tt0); %[kg/m^3]

%%%%%%%%%%%%%%%%%%%%%%%%%%%%%%%%%%%%%%%%%%%%%%%%%%%%%%%%%%%%%%%%%%%%%%%%%%%%%%%
%%%%%%%%%%%%%%%%%%%%%%%%%%     NVT Nozzle Geometry   %%%%%%%%%%%%%%%%%%%%%%%%%%
%%%%%%%%%%%%%%%%%%%%%%%%%%%%%%%%%%%%%%%%%%%%%%%%%%%%%%%%%%%%%%%%%%%%%%%%%%%%%%%

%Throat diameter
d_star = 0.0005; %[m]
%Exit diameter
de = 0.005; %[m]
%Throat area
A_star = (pi/4)*d_star^2; %[m^2]
%Exit area
Ae = (pi/4)*de^2; %[m^2]
%Area ratio
AR = Ae/A_star;
%Nozzle half-angle
Theta = 30*deg_to_rad; %[rad]

%%%%%%%%%%%%%%%%%%%%%%%%%%%%%%%%%%%%%%%%%%%%%%%%%%%%%%%%%%%%%%%%%%%%%%%%%%%%%%%
%%%%%%%%%%%%%%%%%%%%%%%%%%       Valve Flow       %%%%%%%%%%%%%%%%%%%%%%%%%%%
%%%%%%%%%%%%%%%%%%%%%%%%%%%%%%%%%%%%%%%%%%%%%%%%%%%%%%%%%%%%%%%%%%%%%%%%%%%%%%%

%Parker
%Temperature upstream
T1 = (Tt0 - 273.15)*1.8 + 491.67; %[R]
%Pressure upstream
P1 = Pt0*pa_to_psi; %[psia]
%Volumetric flow rate
Q1 = 13.63*Cv*P1*sqrt(1/(T1*SG)); %[SCFM]
%Mass flow rate
m_dot1 = Cd*SCFM_to_SCMS*rho_s*Q1; %[kg/sec]

%Swagelok
%Unit constant
N = 22.67;
%Volumetric flow rate
Q3 = 0.471*N*Cv*P1*sqrt(1/(SG*T1)); %[SCFM]
%Mass flow rate
m_dot3 = Cd*SCFM_to_SCMS*rho_s*Q3; %[kg/sec]

%Lee Company
%Unit constant
K = 0.629;
%Temperature correction factor
f = sqrt(530/T1);
%Volumetric flow rate
Q2 = K*f*P1/L; %[kg/min]
%Mass flow rate
m_dot2 = Cd*Q2/60; %[kg/sec]


%NASA GFSSP
%Area Pipe
OD = (1/16); %[in]
wt = 0.014; %[in]
```

```
ID = OD - 2*wt; %[in]
A1 = (pi/4)*ID^2; %[in^2]
%Acceleration due to gravity
gc = 32.174; %[ft/sec^2]
%Density
rho1 = rhot0*kg_m3_to_lb_ft_3; %[lb/ft^3]
%Critical pressure
Pcr = (2/(gamma+1))^(gamma/(gamma-1));
%Mass flow rate
for i=1:length(P1)
    m_dot4(i) = Cd*0.453592*Cv*A1*sqrt(P1(i)*rho1(i)*gc*(2*gamma/...
        (gamma-1))*Pcr^(2/gamma)*(1-Pcr^((gamma-1)/gamma))); %[kg/sec]
end

%%%%%%%%%%%%%%%%%%%%%%%%%%%%%%%%%%%%%%%%%%%%%%%%%%%%%%%%%%%%%%%%%%%%%%%%%%%%
%%%%%%%%%%%%%%%%%%     Ideal Nozzle Equations      %%%%%%%%%%%%%%%%%%%%%%%%
%%%%%%%%%%%%%%%%%%%%%%%%%%%%%%%%%%%%%%%%%%%%%%%%%%%%%%%%%%%%%%%%%%%%%%%%%%%%

%Chamber Pressure
Pc1 = m_dot1/((A_star/sqrt(Tt0))*sqrt(gamma/R)*(((gamma+1)/2)^...
    (-(gamma+1)/(2*(gamma-1))))); %[N/m^2]
Pc2 = m_dot2/((A_star/sqrt(Tt0))*sqrt(gamma/R)*(((gamma+1)/2)^...
    (-(gamma+1)/(2*(gamma-1))))); %[N/m^2]
Pc3 = m_dot3/((A_star/sqrt(Tt0))*sqrt(gamma/R)*(((gamma+1)/2)^...
    (-(gamma+1)/(2*(gamma-1))))); %[N/m^2]
Pc4 = m_dot4/((A_star/sqrt(Tt0))*sqrt(gamma/R)*(((gamma+1)/2)^...
    (-(gamma+1)/(2*(gamma-1))))); %[N/m^2]
%Area-Mach Relationship
syms y;
eqn3 = (AR == (1/y)*((2/(gamma + 1))*(1 + ((gamma - 1)/2)*y^2))^...
    ((gamma + 1)/(2*(gamma - 1)))); %Mach area relation
assume( y > 1 );
%Exit Mach number
Me = real(double(solve(eqn3, y)));
%Exit Temperature
Te = Tt0/(1 + ((gamma - 1)/2)*Me^2); %[K]
%Exit pressure
Pe = Pc1/(1 + ((gamma - 1)/2)*Me^2)^(gamma/(gamma - 1)); %[N/m^2]
%Exit velocity
ue = Me*sqrt(gamma*R*Te); %[m/sec]
%Correction factor
lamda = (1/2)*(1+cos(Theta));
%Thrust
F1 = lamda*m_dot1*ue + Pe*Ae; %[N]
F2 = lamda*m_dot2*ue + Pe*Ae; %[N]
F3 = lamda*m_dot3*ue + Pe*Ae; %[N]
F4 = lamda*m_dot4*ue + Pe*Ae; %[N]
%Specific Impulse
Isp = F1/(m_dot1*9.81); %[sec]



%%%%%%%%%%%%%%%%%%%%%%%%%%%%%%%%%%%%%%%%%%%%%%%%%%%%%%%%%%%%%%%%%%%%%%%%%%%%
%%%%%%%%%%%%%%%%%%%%%%   Thrust Data Analysis     %%%%%%%%%%%%%%%%%%%%%%%%%
%%%%%%%%%%%%%%%%%%%%%%%%%%%%%%%%%%%%%%%%%%%%%%%%%%%%%%%%%%%%%%%%%%%%%%%%%%%%

%   Data = xlsread('NVT_0');
%Data = xlsread('NVT_10');
Data = xlsread('NVT_20');
% Data = xlsread('NVT_30');
```

```
%%%%%%%%%%%%%%%%%%%%%%%%%%%%%%%%%%%%%%%%%%%%%%%%%%%%%%%%%%%%%%%%%%%%%%%%%%%%
%%%%%%%%%%%%%%%%%%%%%%%%          Plots          %%%%%%%%%%%%%%%%%%%%%%%%%%
%%%%%%%%%%%%%%%%%%%%%%%%%%%%%%%%%%%%%%%%%%%%%%%%%%%%%%%%%%%%%%%%%%%%%%%%%%%%

figure
scatter(Data(:,1),Data(:,2));
%Least Mean Square Line of the Data
h=lsline;
p2 = polyfit(get(h,'xdata'),get(h,'ydata'),1);
hold on
plot(Pt0*pa_to_psi,F1,Pt0*pa_to_psi,F2,Pt0*pa_to_psi,F3,Pt0*pa_to_psi,F4)
hold on
legend('Thrust Data','Least-Mean-Square','Parker','Swagelok','Lee','NASA')
xlabel('Line Pressure [psia]')
ylabel('Thrust [N]')
title('NVT Thrust Performance (20C)')

%%%%%%%%%%%%%%%%%%%%%%%%%%%%%%%%%%%%%%%%%%%%%%%%%%%%%%%%%%%%%%%%%%%%%%%%%%%%
%%%%%%%%%%%%%%%%%%%%%%%%     Error Analysis      %%%%%%%%%%%%%%%%%%%%%%%%%%
%%%%%%%%%%%%%%%%%%%%%%%%%%%%%%%%%%%%%%%%%%%%%%%%%%%%%%%%%%%%%%%%%%%%%%%%%%%%

%Thrust measured
F_meas = p2(1)*Pt0*pa_to_psi + p2(2); %[N]
%Error
error1 = (F1 - F_meas)/F_meas;
error2 = (F2 - F_meas)/F_meas;
error3 = (F3 - F_meas)/F_meas;
error4 = (F4 - F_meas)/F_meas;
```

APPENDIX D.

PENDULUM THRUST STAND DISPLACEMENT DATA

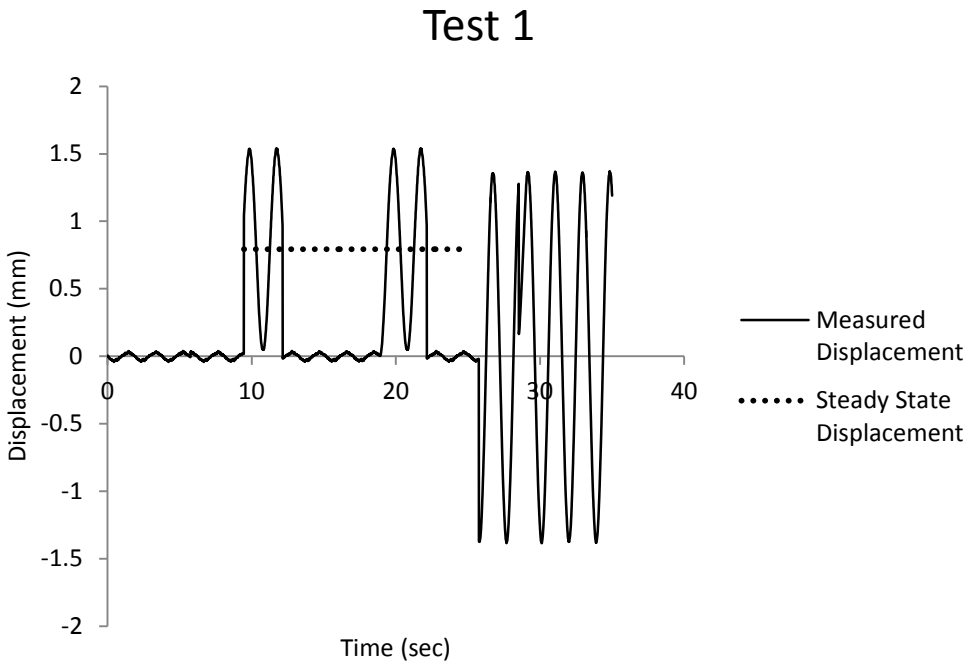

Figure D.1. The measured and calculated steady state displacement of the pendulum thrust stand for test 1.

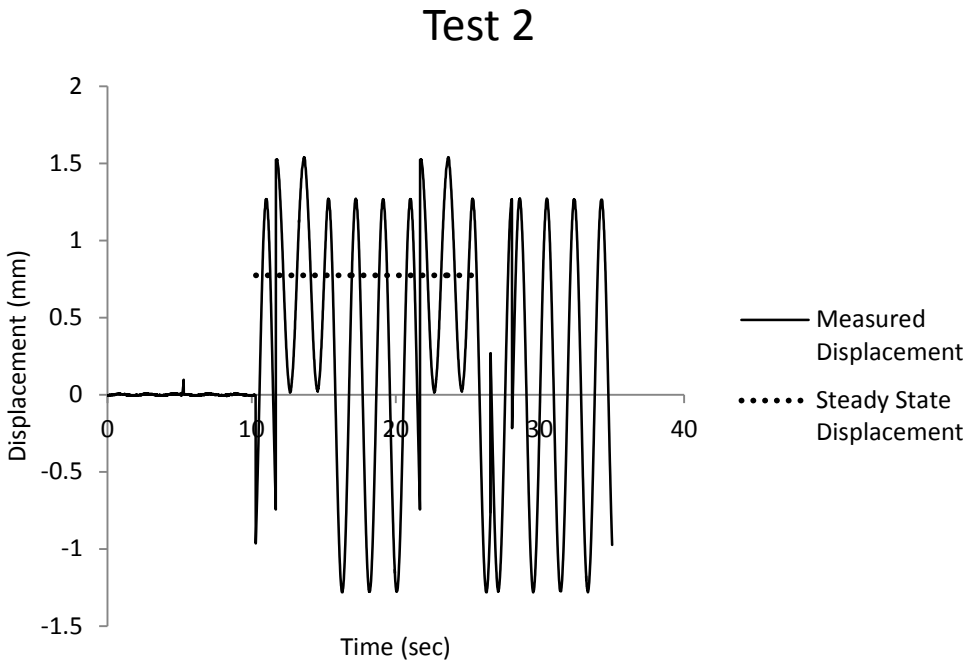

Figure D.2. The measured and calculated steady state displacement of the pendulum thrust stand for test 2.

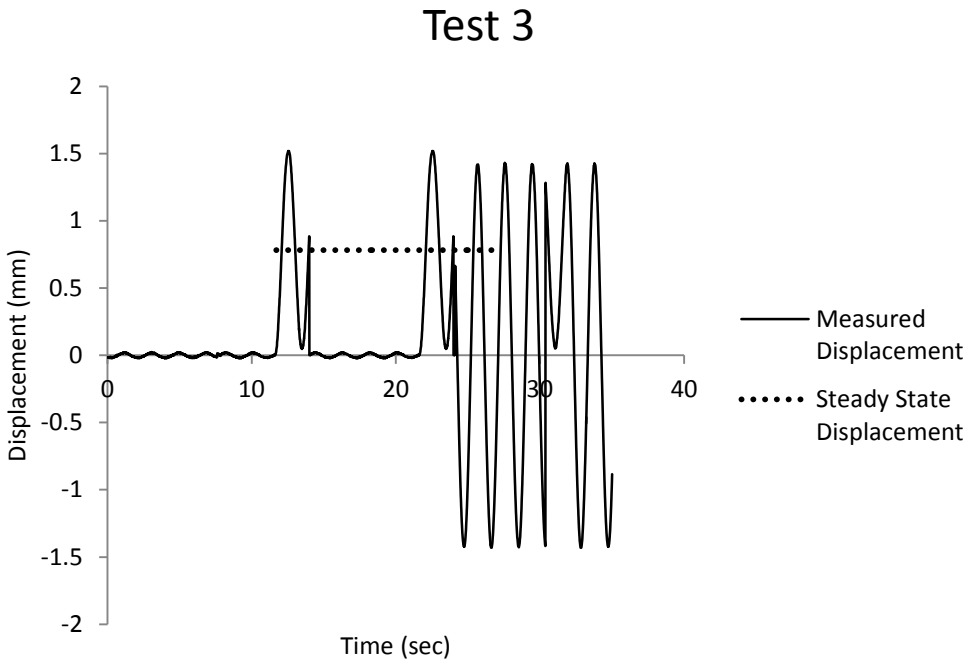

Figure D.3. The measured and calculated steady state displacement of the pendulum thrust stand for test 3.

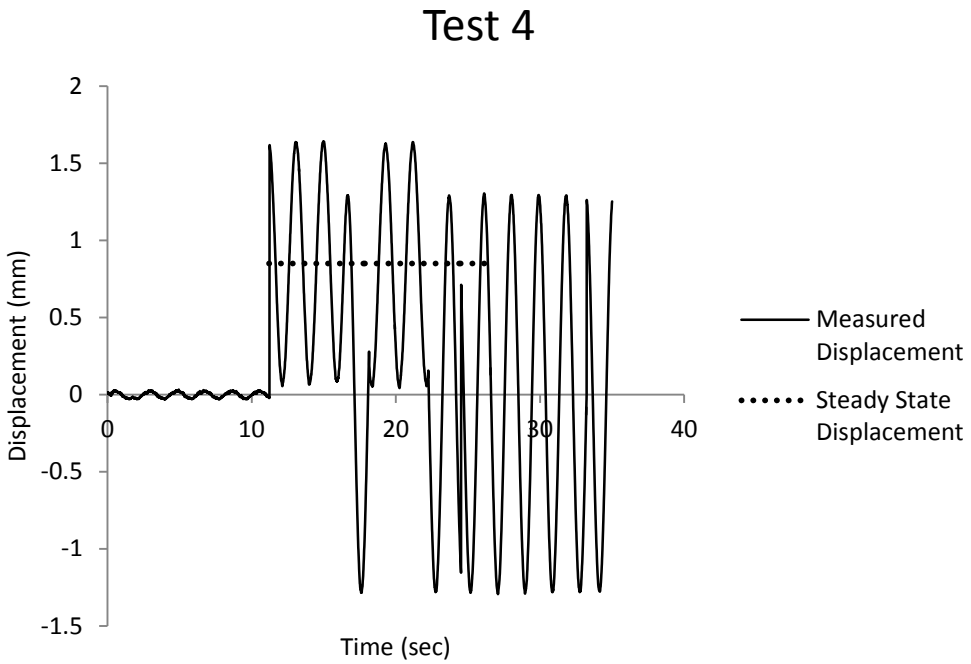

Figure D.4. The measured and calculated steady state displacement of the pendulum thrust stand for test 4.

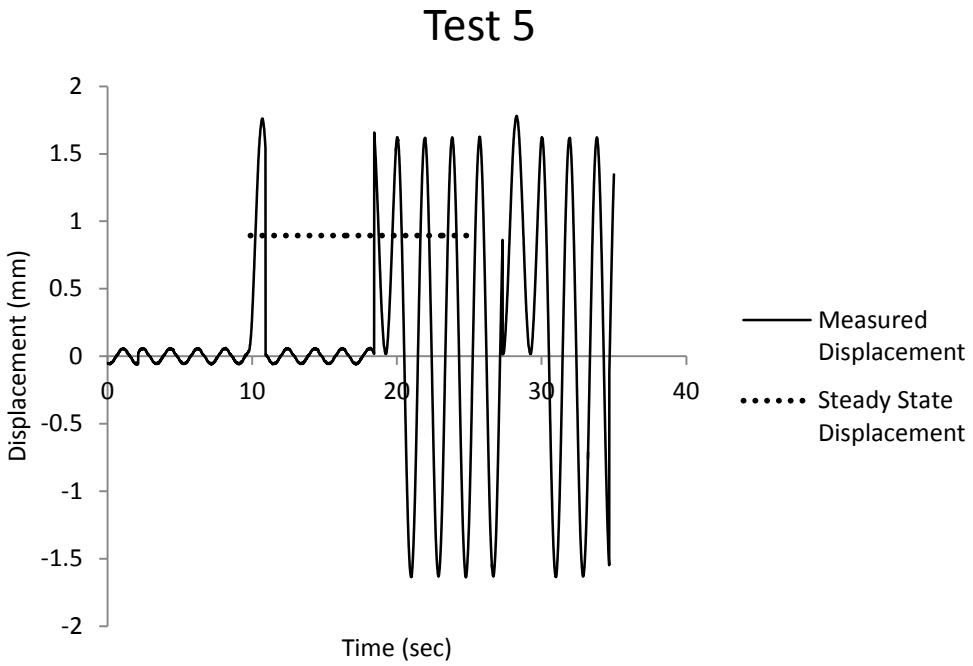

Figure D.5. The measured and calculated steady state displacement of the pendulum thrust stand for test 5.

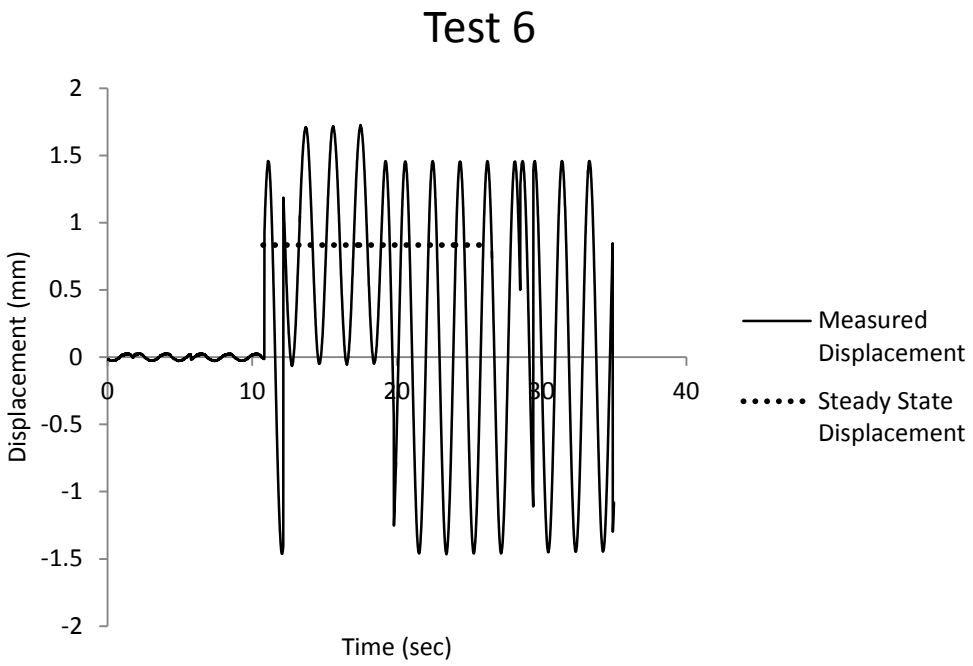

Figure D.6. The measured and calculated steady state displacement of the pendulum thrust stand for test 6.

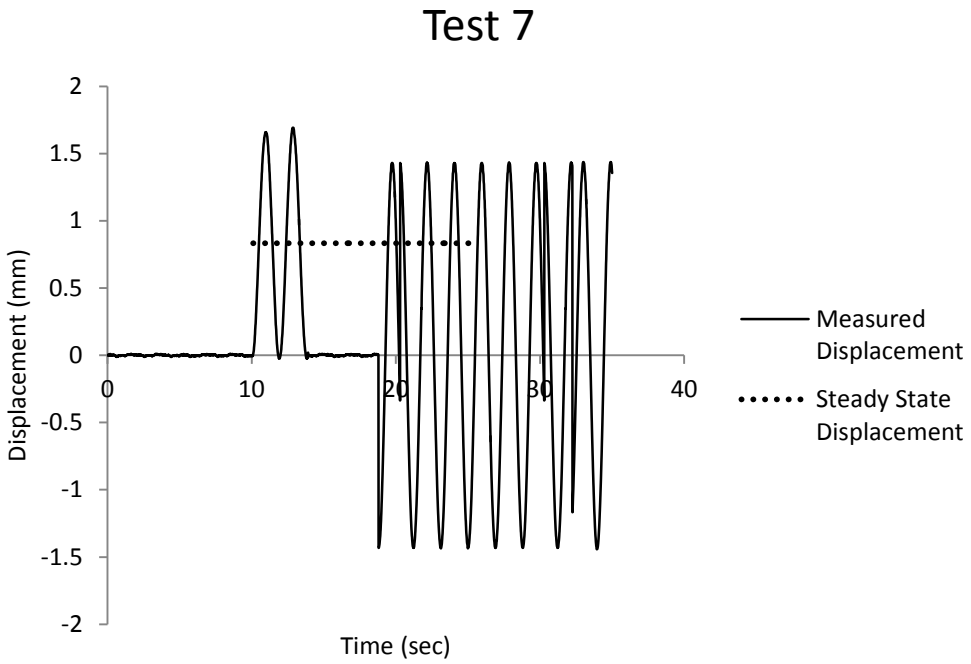

FigureD5.7. The measured and calculated steady state displacement of the pendulum thrust stand for test 7.

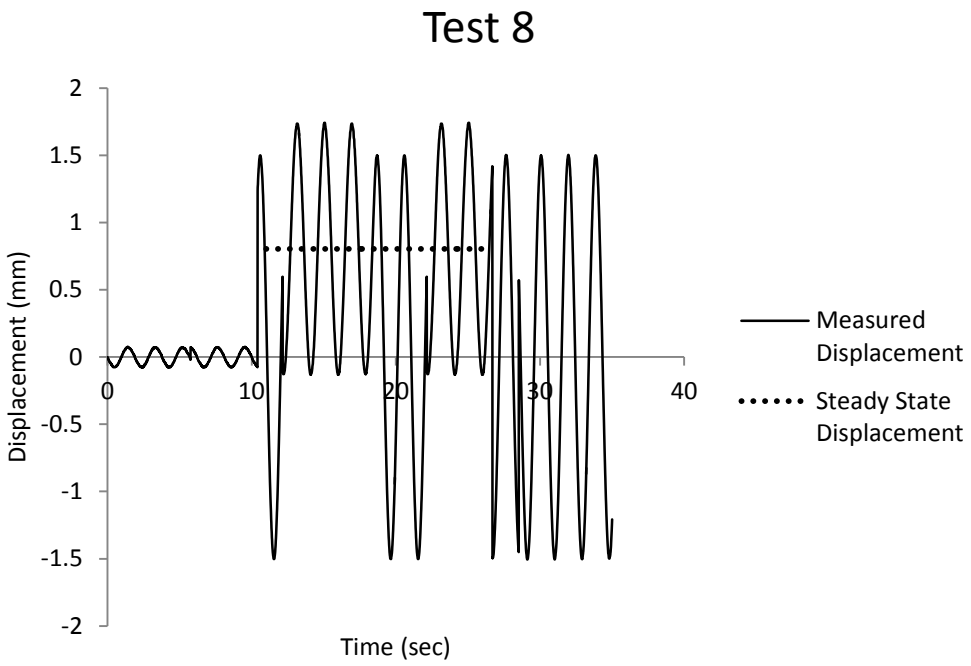

Figure D.8. The measured and calculated steady state displacement of the pendulum thrust stand for test 8.

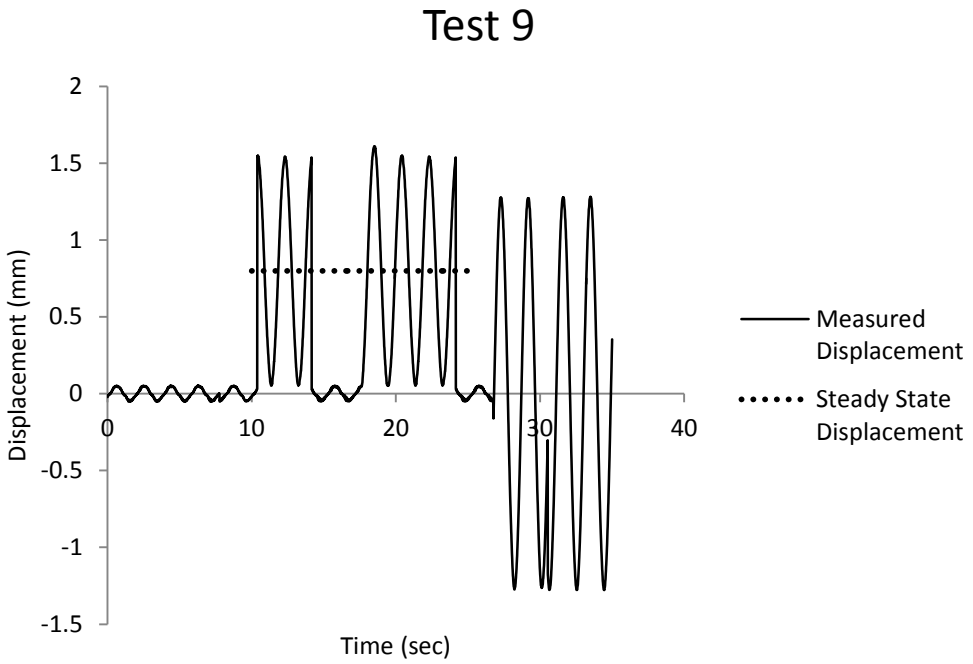

Figure D.9. The measured and calculated steady state displacement of the pendulum thrust stand for test 9.

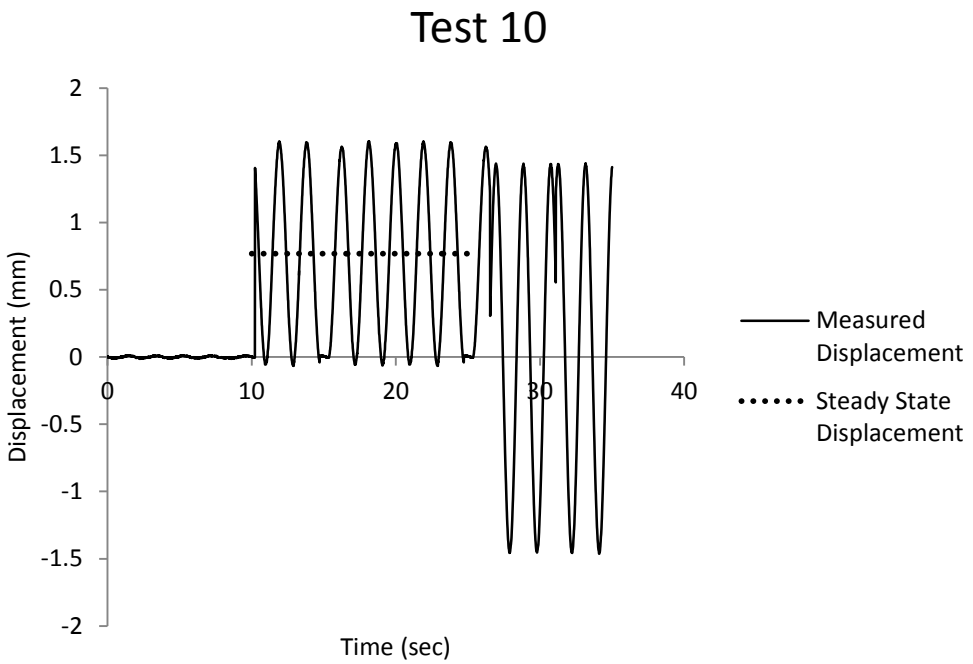

Figure D.10. The measured and calculated steady state displacement of the pendulum thrust stand for test 10.

BIBLIOGRAPHY

[1] Darling, D. (n.d.). "Sputnik." Retrieved March 27, 2017, from http://www.daviddarling.info/encyclopedia/S/Sputnik.html.

[2] Loff, S. "Explorer 1 Overview." *National Aeronautics and Space Administration.* July 30, 2015. March 27, 2017. https://www.nasa.gov/mission_pages/explorer/explorer-overview.html.

[3] "Pioneer 1." *NASA Space Science Data Coordinated Archive*. March 27, 2017. https://nssdc.gsfc.nasa.gov/nmc/spacecraftDisplay.do?id=1958-007A.

[4] Sutton G. P. and Biblarz O. *Rocket Propulsion Elements.* Wiley, Hoboken, NJ, 8th edition, 2010.

[5] "F-1." *Encyclopedia Astronautica*. March 27, 2017. http://www.astronautix.com/f/f-1.html.

[6] "SRB." *Encyclopedia Astronautica.* March 27, 2017. http://www.astronautix.com/s/srb.html.

[7] "SpaceShip One." *Encyclopedia Astronautica*. March 27, 2017. http://www.astronautix.com/s/spaceshipone.html.

[8] "SpaceDev Hybrid." *Encyclopedia Astronautica.* March 27, 2017. http://www.astronautix.com/s/spacedevhybrid.html.

[9] P. Fortescue, J. Stark, and G. Swinerd, editors, *Spacecraft Systems Engineering.* John Wiley & Sons Ltd, West Sussex, England, 3rd edition, 2003.

[10] T. K. Imken, T. H. Stevenson, and E. G. Lightsey, (2015) "Design and Testing of a Cold Gas Thruster for an Interplanetary CubeSat Mission." *Journal of Small Satellites*, Vol. 4, No. 2, pp. 371-386.

[11] A. Rachid, K. Toshiyuki, A. Nobuyuki, and H. Keiichi. (2017). "Hydroxylammonium nitrate (HAN)-based green propellant as alternative energy resource for potential hydrazine substitution: From lab scale to pilot plant scale-up." *Combustion and Flames*, Vol. 176, pp. 334-348.

[12] "MR-103." *Encyclopedia Astronautica,* March 29, 2017. http://www.astronautix.com/m/mr-103.html.

[13] "OME." *Encyclopedia Asronautica,* March 29, 2017. http://www.astronautix.com/o/ome.html.

[14] D. M. Goebel and I. Katz. *Fundamentals of Electric Propulsion: Ion and Hall Thrusters.* John Wiley & Sons, Inc. Hoboken, N.J. 2008.

[15] C. M. Marrese. "A Review of Field Emission Cathode Technologies for Electric Propulsion Systems and Instruments." IEEE, *Aerospace Conference*, March 25th, 2000.

[16] F. Mier-Hicks and P. C. Lozano. "Electrospray Thrusters as Precise Attitude Control Actuators for Small Satellites." *Journal of Guidance, Control, and Dynamics*, Vol. 40, No. 3, March 2017.

[17] H. Dali, Z. Wansheng, and K. Xiaoming. "Operation Analysis of Pulsed Plasma Thruster." *Acta Astronautica*. Vol. 62, pp 404-409, 2008.

[18] M. S. Glascock, J. L. Rovey, S. Williams, and J. Thrasher. "Plasma Plume Characterization of Electric Solid Propellant Pulsed Microthrusters." *AIAA 51st Joint Propulsion Conference*, Orlando, FL, July 27-29, 2015.

[19] M. L. R. Walker, R. R. Hofer, and A. D. Gallimore. "The Effects of Nude Faraday Probe Design and Vacuum Facility Backpressure on the Measured Ion Current Density Profile of Hall Thruster Plumes." *AIAA 38th Joint Propulsion Conference*, Indianapolis, IN, July 7-10, 2002.

[20] R. Eckman, L. Byrne, N. A. Gatsonis, and E. J. Pencil. "Triple Langmuir Probe Measurements in the Plume of a Plasma Thruster," *Journal of Propulsion and Power*, Vol. 17, No. 4, pp 762-771, July-August 2001.

[21] R. Eckman. "Pulsed Plasma Thruster Plume Diagnostics," *36th AIAA Aerospace Science Meeting and Exhibit*, Reno, NV, 1998.

[22] N. Kumagai, M. Igarashi, K. Sato, K. Tamura, and H. Takegahara. "Plume Diagnostics in Pulsed Plasma Thruster," *AIAA 38th Joint Propulsion Conference*, Indianapolis, IN, July 7-10, 2002.

[23] L. T. Byrne, J. Zwahlen, N. A. Gatsonis, and E. J. Pencil. "Pulsed Plasma Thruster Plume Measurements Using A Triple Probe Method," *AIAA 38th Joint Propulsion Conference*, Indianapolis, IN, July 7-10, 2002.

[24] M. Lau, S. Manna, G. Herdrich, T. Schonherr, and K. Komuraski. "Investigation of the Plasma Current Density of a Pulsed Plasma Thruster," *Journal of Propulsion and Power*, Vol. 30, No. 6, pp. 1459-1470, November-December 2014.

[25] S. I. Chen, and T. Sekiguchi. “Instantaneous Direct-Display System of Plasma Parameters by Means of Triple Probe,” *Journal of Applied Physics*, Vol. 36, No. 8, pp. 2363-2375, August 1965.

[26] J.L Rovey, M. L. R. Walker, A. D. Gallimore, and P. Y. Peterson. “Evaluation of a Magnetically-Filtered Faraday Probe for Measuring the Ion Current Density Profile of a Hall Thruster,” *AIAA 40th Joint Propulsion Conference*, Fort Lauderdale, FL, July 11-14, 2004.

[27] D. Aktas. “Simulations of a Langmuir Probe,” *AIAA 50th Aerospace Sciences Meeting*, Nashville, TN, January 9-12, 2012.

[28] T. Schönherr, F. Ness, Y. Arakawa, K. Komurasaki, and G. Herdrich. “Characteristics of Plasma Properties in an Ablative Pulsed Plasma Thruster.” *Physics of Plasmas*, Vol. 20, Issue 3, 2013.

[29] Y. Li, R. Zhang, and J. Zong. “Study of the Plume Characteristics of Pulsed Plasma Thruster.” *Applied Mechanics and Materials*, Vol. 347-350, pp 55-58, 2013.

[30] K. Parker. “Pulse Plasma Thruster Plume Analysis.” *Acta Astronautica*, Vol. 53, Is. 4-10, pp. 789-795, August-November 2003.

[31] N. A. Gatsonis, J. Zwahlen, A. Wheelock, E. Pencil, and H. Kamhawi. “Characterization of a Pulsed Plasma Thruster Plume using a Quadruple Langmuir Probe Method.” *AIAA 38th Joint Propulsion Conference and Exhibit*, Indianapolis, IN, July 7-10, 2002.

[32] A. Rezaeiha, and T. Schönherr. “Review of Worldwide Activities in Liquid-Fed Pulsed Plasma Thruster.” *Journal of Propulsion and Power*, Vol. 30, No. 2 March-April, 2014.

[33] A. Kakami, H. Koizumi, K. Komursaki, and Y. Arakawa. “Performance Study on Liquid Propellant Pulsed Plasma Thruster.” *AIAA 39th Joint Propulsion Conference and Exhibit*, Huntsville, AL, July 20-23, 2003.

[34] “GEM-Fueled LPPT.” Digital Solid State Propulsion, Inc., Reno, NV. (proprietary).

[35] “DSSP Multiple Energy Discharge Controller.” Digital Solid State Propulsion, Inc., Reno, Nevada. (proprietary).

[36] “DSSP Valved Liquids Actuation Device (VLAD) Version 1.0.” Digital Solid State Propulsion, Inc., Reno, NV. (proprietary).

[37] "Safety Data Sheet – GEM 10T", Digital Solid State Propulsion, Inc., Reno, Nevada, 8/31/2015.

[38] C. R. Seubert. "Refrigerant-Based Propulsion System for Small Spacecraft", M.S. Thesis, Mechanical and Aerospace Engineering Department, Missouri University of Science and Technology, Rolla, MO, 2007.

[39] J. R. Siebert. "Design, Hazard Analysis, and System Level Testing of a University Propulsion System for Spacecraft Application", M.S. Thesis, Mechanical and Aerospace Engineering Department, Missouri University of Science and Technology, Rolla, MO, 2009.

[40] R. A. Pahl. "Integration and Test of A Refrigerant-Based Cold-Gas Propulsion System for Small Satellites", M.S. Thesis, Mechanical and Aerospace Engineering Department, Missouri University of Science and Technology, Rolla, MO, 2010.

[41] D. Newberry, P. Galchenko, and H. Pernicka. "PRP108 Nozzle and Valve Design." Internal Document, Missouri S&T Satellite Research Team, Missouri University of Science and Technology, January 12, 2017.

[42] J. E. Polk, A. Pancotti, T. Haag, S. King, M. Walker, J. Blakely, and J. Ziemer. "Recommended Practices in Thrust Measurements." *33rd International Electric Propulsion Conference*, Washington DC, October 6-10, 2013.

[43] C. Lugini and M. Romano. "A Ballistic-Pendulum Test Stand to Characterize Small Cold-Gas Thruster Nozzle." *Acta Astronautica*, Vol. 64, Iss. 5-6, March-April 2009, PP. 615-625.

[44] C. Eckert, D. Newberry, P. Galchenko, H. Pernicka. "PRP605 Thrust Testing." Internal Document, Missouri S&T Satellite Research Team, Missouri University of Science and Technology, January 12, 2017.

[45] D. C. Wilcox, *Basic Fluid Mechanics*. 5th ed., DCW Industries, La Canada, California, 2012.

[46] D. C. Rennels and H. M. Hudson. *Pipe Flow: A Practical and Comprehensive Guide*. Wiley, Hoboken, NJ, 2012.

[47] A. K. Majumbar, A. C. LeClair, R. Moore, and P. A. Schallhorn. "Generalized Fluid System Simulation Program, Version 6.0." NASA/TM-2013-217492, 2013.

[48] Technical Hydraulic Handbook. 11th ed., The Lee Company, Westbrook, CT, 2009.

[49] Valve Sizing Technical Bulletin, Swagelok Company, 2002.

[50] Valve Technical Guide. Parker Instrumentation, Jacksonville, AL.

[51] “Extended Performance Solenoid Valve.” Product Datasheet, The Lee Company, Westbrook, CT, 2010.

VITA

Jeremiah Daniel Hanna was born on May 21st, 1990, to Michael and Lori Hanna in Saint Louis, Missouri. Despite the best efforts of his parents Jeremiah dropped out of Camdenton High School during his junior year. Strongly encouraged by his family he returned to Camdenton High School and obtained his GED. It was not until he was 19 years old would he begin his collegiate career.

Jeremiah enrolled at the Osage Beach campus of State Fair Community College in the fall of 2009. He spent three semesters there taking general education classes originally in a business degree program. Jeremiah began attending Ozark Technical Community College in Springfield, Missouri, in the spring 2011 semester. He graduated from Ozark Technical Community College with an Associate in Engineering at the end of 2012. He was accepted to attend the Missouri University of Science and Technology for the spring 2013 semester. Originally enrolled as a dual major in aerospace and mechanical engineering. He graduated as a magna cum laude in aerospace engineering in December 2015. During his last undergraduate semester he began working on a masters in aerospace engineering. He received his master's of science in aerospace engineering from Missouri University of Science and Technology in July of 2017.